Instituto Universitário de Lisboa

DEPARTMENT OF INFORMATION SCIENCE AND TECHNOLOGY

Impact of In-Band Crosstalk on the Performance of Optical Coherent Detection Communication Systems

Dissertation presented in partial fulfillment of the requirements for the Masters Degree on Telecommunications and Information Science

by

Bruno Rafael Pereira Pinheiro

Supervisors:

Dr. João Rebola, Assistant Professor,

ISCTE-IUL

Dr. Luís Cancela, Assistant Professor,

ISCTE-IUL

April, 2015

Acknowledgements

I am fortunate to have been supervised in this dissertation by Prof. João Rebola and Prof. Luís Cancela. Throughout this work, their availability and patience in all my doubts and questions, provided me support and guidance to conclude this dissertation. I am also thankful to Instituto de Telecomunicações (IT) for providing access to their installations.

I would like to thank my family for their unconditional support, love and encouragement. A warm feeling towards Susana, who always helps me to get my confidence back when things became difficult.

Finally, I would like to thank all my friends and colleagues for all their support during the past years.

Thank you all!

Resumo

A detecção óptica coerente leva à coexistência de sinais com diferentes formatos de modulação e diferentes ritmos binários nas redes ópticas. Devido a essa coexistência vários cenários de diafonia homódina (in-band crosstalk) são possíveis. Neste trabalho, o impacto do in-band crosstalk devido a sinais interferentes com o formato de modulação em amplitude em quadratura (M-QAM) no desempenho do PDM-QPSK e PDM-16-QAM receptores coerentes a um ritmo binário agregado de 100 Gbps é estudado utilizando simulação Monte-Carlo. A precisão do método de magnitude do vector de erro (EVM) também é investigado na presença de in-band crosstalk, e revelou ser suficientemente preciso na estimação o nível de interferência que leva a uma penalidade de 1 dB na relação sinal-ruído óptico (OSNR) no receptor. No entanto, a precisão do método EVM foi diminuída, relativamente à estimativa da penalidade na OSNR devido a níveis de in-band crosstalk mais elevados.

A influência do factor de duração de ciclo, do desalinhamento temporal e da diferença de fase entre o sinal interferência e o sinal seleccionado no desempenho do receptor é também avaliada. Mostra-se que o sinal QPSK com um factor de duração de ciclo de 33% é, em geral, o sinal seleccionado mais tolerante ao in-band crosstalk e o interferente menos prejudicial para o desempenho do receptor coerente. Mostramos também que o desalinhamento temporal tem uma influência significativa no impacto do in-band crosstalk no desempenho do receptor coerente, quando o factor de duração de ciclo dos interferente ou do sinal seleccionado são baixos, e a diferença de fase tem impacto quase desprezável na variação da penalidade de OSNR.

Palavras-chave: Crosstalk homódino, magnitude do vector de erro, modulação de amplitude em quadratura, simulação de Monte-Carlo, sistemas ópticos com detecção coerente.

Abstract

Optical coherent technology leads to the coexistence of signals with different modulation formats and different bit rates in optical networks. Due to this coexistence several in-band crosstalk scenarios are possible. In this work, the impact of in-band crosstalk due to M-ary quadrature amplitude modulation (M-QAM) interferers on the performance of PDM-QPSK and PDM-16-QAM coherent receivers at an aggregated bit rate of 100 Gbps is studied using Monte Carlo simulation. The accuracy of the error vector magnitude method is also investigated in presence of in-band crosstalk and it revealed to be sufficiently accurate for the estimation of the crosstalk level that leads to a 1 dB Optical Signal-to-Noise ratio (OSNR) penalty at the receiver. However, the EVM method accuracy was diminished, concerning the estimation of the OSNR penalty due to higher crosstalk levels.

The influence of the duty-cycle, time misalignment and phase difference between interferers and selected signal on the receiver performance is also assessed. We show that the QPSK signal with a duty-cycle of 33% is, generally, the most tolerant selected signal to in-band crosstalk and the less detrimental interferer to the coherent receiver performance. We also show that the time misalignment has a significant influence on the in-band crosstalk impact, when the duty-cycles of the interferers or selected signal are low, and the phase difference has almost negligible impact on the OSNR penalty variation.

Keywords: Error vector magnitude, in-band crosstalk, Monte-Carlo simulation, optical coherent detection communication systems, quadrature amplitude modulation.

Contents

List of Figures

List of Tables

List of Acronyms

ASE	Amplified Spontaneous Emission
AWGN	Additive White Gaussian Noise
BER	Bit Error Rate
DEC	Direct Error Counting
DPSK	Differential Phase-Shift Keying
DQPSK	Differential Quadrature Phase-Shift Keying
DSP	Digital Signal Processing
ED	Eye Diagram
EDFA	Erbium-Doped Fiber Amplifier
EF	Electrical Filter
EVM	Error Vector Magnitude
FFT	Fast Fourier Transform
GF	Galois Field
IP	Internet Protocol
ISI	Intersymbolic Interference
LO	Local Oscillator
***M*-PSK**	M-ary Phase-Shift Keying
***M*-QAM**	M-ary Quadrature Amplitude Modulation
MC	Monte-Carlo
OA	Optical Amplifier
OF	Optical Filter
OOK	On-Off Keying
OPLL	Optical Phase-Locked Loop
OSA	Optical Spectrum Analyzer
OSNR	Optical Signal-to-Noise Ratio
PBS	Polarization Beam Splitter
PDF	Probability Density Function

PDM	Polarization Division Multiplexing
PMF	Probability Mass Function
PRBS	Pseudo-Random Bit Sequence
PSD	Power Spectral Density
QF	Quadrature Front-End
ROADM	Reconfigurable Optical Add-Drop Multiplexer
SE	Spectral Efficiency
SNR	Signal-to-Noise Ratio
WDM	Wavelength-Division Multiplexing

List of Symbols

Δf	Frequency resolution
δ_{XT}	Penalty due to crosstalk
λ_0	Selected signal wavelength
λ_{XT}	Crosstalk signal wavelength
$\mathscr{F}\{\}$	Fourier Transform
ν_0	Optical carrier frequency
ν_{LO}	Local oscillator optical frequency
$\phi(t)$	Signal phase
ϕ_ε	Phase difference
B	Bit rate
B_e	-3 dB bandwidth of the electrical filter
B_o	-3 dB bandwidth of the optical filter
$B_{e,opt}$	Optimized -3 dB bandwidth of the electrical filter
$B_{o,opt}$	Optimized -3 dB bandwidth of the optical filter
B_{OSA}	Optical Spectrum Analyzer bandwidth
B_{sim}	Simulation bandwidth
$E[.]$	Expected value
E_0	Electrical field after optical filtering
$E_T(t)$	Transmitted electrical field
$E_x(t)$	Interfering signal electrical field
$E_{0,x}(t)$	Electrical field in polarization x
$E_{0,y}(t)$	Electrical field in polarization y
$E_{LO,x}(t)$	Local oscillator electrical field in polarization x
$E_{LO,y}(t)$	Local oscillator electrical field in polarization y
h	Planck constant
N_0	ASE noise power spectrum density after optical filtering
N_a	Number of samples per symbol

N_I	ASE noise power spectrum density of the in-phase component
N_Q	ASE noise power spectrum density of the quadrature component
N_s	Number of symbols
N_x	Total number of interfering signals
N_{ASE}	ASE noise power spectrum density
N_{MC}	Number of MC sample functions
P_0	Average power of the selected signal
P_{LO}	Local oscillator power
R_s	Symbol Rate
T	Overall duration of the simulated signal
T_a	Sampling time
t_i	Time misalignment of the i-th interferer
T_s	Symbol time
X_c	Crosstalk level
$X_{c,max}$	Crosstalk level for 1 dB OSNR penalty

Chapter 1

Introduction

In the last years, the data traffic in the telecommunications networks had an exponential growth [1]. Figure 1.1 shows the evolution of the global Internet Protocol (IP) traffic since its beginning and the predicted growth until 2016. As it can be observed, the IP traffic in 2015 has increased about 10 orders of magnitude since 1980, and, in the next years, it is predicted that it continues to grow [1]. This increase of traffic demands the evolution of the telecommunications networks infrastructure in order to respond to the increasing communication need from users and also to technological advances. Optical technology has and will continue to enable telecommunication networks to support these traffic requirements [2].

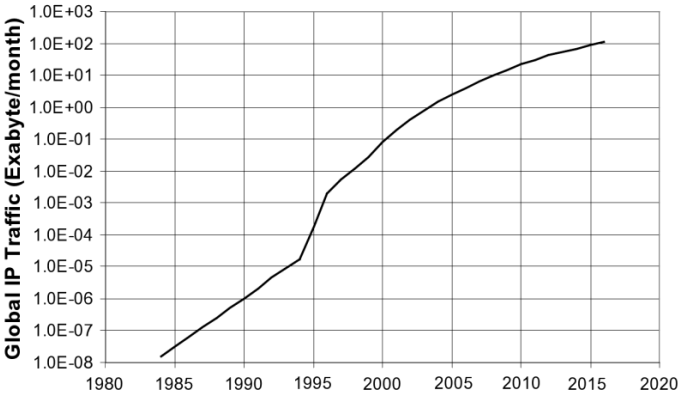

Figure 1.1: Increase of the global IP traffic demands from 1985 to 2016 [1].

1.1 Road to 100 Gbps Optical Networks

The telecommunications networks are highly complex structures. So, in order to simplify the design, development and operation of those networks, it is common to use a layering approach [3]. Figure 1.2 exemplifies the

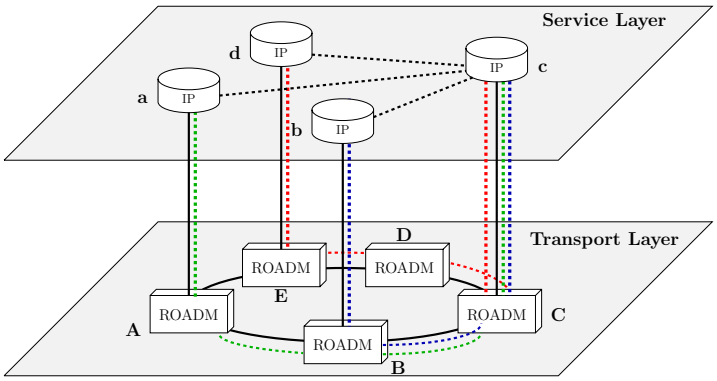

Figure 1.2: Layering approach for a telecommunication network [3].

layering concept for a telecommunication network. The upper layer is the service network layer and, nowadays, it is mainly formed by IP routers, which function is to gather and aggregate all information from the users. On the other hand, the transport network layer provides transmission paths for the service network layer, which are represented by colored dashed lines. In order to deliver high data capacity with lower signal loss, the transmission medium that supports the transport network layer is the optical fiber. The network elements of the transport network layer represented in Figure 1.2 are Reconfigurable Optical Add-Drop Multiplexers (ROADMs).

The first optical networks served telephone services that required narrow bandwidth, a few kHz, but, as the communication services evolved, with the introduction of the Internet, the required bandwidth started to be more demanding. The IP has became the dominant traffic type in the service network layer, and the optical transport network has started to carry traffic from IP routers, MPLS (Multi-Protocol Label Switching) and Ethernet switches [1]. However, in the last decades, as shown in Figure 1.1, the IP traffic had a growth at a rate with a factor of ten [2], while the capacity of the optical transport networks has increased with a factor of four [1]. Figure 1.3 depicts the evolution of the optical transport network standard and the Ethernet port speed standard. Figure 1.3 shows that, in 2010, the deployment of OTU-4 standard allowed the optical channel capacity to reach the Ethernet port speed of 100 Gbps [1], [4].

The OTU-4 standard came from a long research work and several techniques to reach 100 Gbps were investigated and tested. The elected approach was to adopt advanced detection schemes in order to increase the spectral efficiency (SE) per wavelength. Successful implementations were made by using optical differential detection, direct detection and coherent detection [4]. The latter detection technique was the telecom industry chosen for the OTU-4 standard [1]. The coherent detection allows the reception of high-order modulation signals, which consequently, increases the SE of the optical signal transmission. In addition, this detection scheme combined with Polarization-Division Multiplexing (PDM) technique, doubles the SE of a given modulation format without requiring additional Optical Signal-to-Ratio (OSNR), by transmitting two modulated signals in the same optical carrier frequency, but with orthogonal polarizations [4]. By making use of wavelength divi-

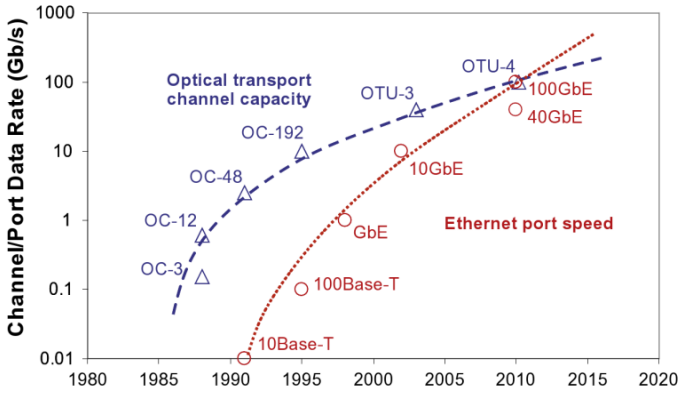

Figure 1.3: Standards of the transport channel capacities and Ethernet port speeds [1].

sion multiplexing (WDM), optical systems with commercial capacities near 10 Tbps are commonly available nowadays [5].

1.2 Modulation Formats

The use of advanced modulation formats is also important to the increase of the optical networks capacity. Since 1985, until the deployment of the OTU-3 standard, On-Off Keying (OOK) was the elected modulation format for the optical transmission. On the receiver side, the detection of the incoming signal power was performed by a technique known as direct detection. The direct detection makes use of a photodiode to convert the optical signal power into an electrical current [6]. The use of optical amplification and WDM extended the use of direct detection and OOK in optical networks to the data rate of 10 Gbps until the end of 2000 [7].

With the deployment of the OTU-3 standard, the optical network reached the channel rate of 40 Gbps, and more modulation formats were used: the OOK 40 Gbps, and the differential modulation formats, such as Differential Phase-Shift Keying (DPSK) or the Differential Quadrature Phase-Shift Keying (DQPSK) [5], [8]. The detection of differential modulation formats is possible by including delay line interferometers and several photodiodes on the receiver, leading to the recovery of the phase information by estimating the phase difference between two consecutive symbols [6].

In 2010, the OTU-4 standard proposed a capacity of 100 Gbps per WDM channel in optical networks with the use of coherent receivers. Hence, the detection of Quadrature Phase-Shift Keying (QPSK) or M-ary Quadrature Amplitude Modulation (M-QAM) optical signals became possible, increasing the SE of the optical transmission. Despite the PDM-QPSK being the modulation format for the 100 Gbps optical networks, the coherent detection enables receiving other higher-order modulation formats. The detection of PDM-32-QAM [9] and PDM-64-QAM [10] signals at a bit rate of 100 Gbps has been also experimented [11].

Regarding the standard for the capacity of future optical transport networks, the most discussed options

are: 400 Gbps or 1 Tbps [1], [2], using higher-order QAM. Moreover, due to the higher OSNR required, and consequent shorter reach of the optical transmission, the 400 Gbps optical networks will require multi-carrier transmission, using superchannels [1], where the optical carriers of the superchannel can be packed more tightly, without the use of guard bandwidth. However, these capacities are still in investigation and their future commercial deployment is not eminent [1]. There are several possibilities for the superchannel design at a data rate of 400 Gbps: using two carriers PDM-16-QAM superchannels, each one with a bit rate of 200 Gbps, or four carriers PDM-QPSK superchannels, each one with a bit rate of 100 Gbps [1]. The PDM-16-QAM superchannel occupies a total bandwidth of 82.9 GHz, and the PDM-QPSK superchannel has a bandwidth of 137.5 GHz. Thus, the total bandwidth of a superchannel, including the superchannels separation gap, is no longer multiple of the actual WDM networks, which have a fixed 50 GHz channel grid. Therefore, the data rate of 400 Gbps signals demands the adoption of a flexible grid, however it will increase the network management and digital signal processing complexity [1].

1.3 In-Band Crosstalk

In today 100 Gbps optical networks, a considerable amount of modulation formats and bit rates for the transmitted signals is possible and their coexistence can lead to more interference crosstalk scenarios than previous network environments.

The crosstalk is a physical impairment caused usually by the imperfect isolation of the optical components inside an optical node, i. e. ROADMs [12]. It originates signal power leakage inside each optical network node, and causes interference between signals that are propagating through the optical link.

The in-band crosstalk is the most detrimental type of crosstalk, since it occurs when the crosstalk and the selected signal have the same nominal wavelength [13]. Consequently, it is impossible to be removed by filtering and can become a serious source of system performance degradation [14], [15]. Moreover, the use of coherent detection receivers on the optical networks leads to a stronger interest in the in-band crosstalk study due to the coexistence of M-QAM modulation formats, OOK and differential modulation formats on the network [11]. Consequently, the interfering signals can have different modulation formats, leading to different impacts on the coherent receiver performance.

The in-band crosstalk and its impact on the network performance was extensively studied, for the OOK [14], DPSK [16] and DQPSK [17] modulation formats, and also for different modulation formats and bit rates than the selected signal [18], [19]. For example, in [19], it was found that the OOK signal is the most detrimental interfering signal in a DPSK 40 Gbps receiver.

However, few studies considering the in-band crosstalk impact on the performance of 100 Gbps coherent receivers can be found in the literature. The work [20] shows that, among the M-QAM modulation formats,

the one that presents greater tolerance to in-band crosstalk is the 4-QAM. In that work, it is considered that the interfering signals have the same modulation format and bit rate than the selected signal. In [21], the in-band crosstalk impact on a 112 Gbps PDM-QPSK receiver performance has been experimentally investigated considering different modulation formats on the interferer. However, the results are not in agreement with [20], particularly, concerning the OSNR degradation of the coherent receiver due to higher crosstalk levels. In this dissertation, we intend to extend and clarify these studies and their conclusions, by studying the interference of signals with a wider variation of the signal parameters: different modulation formats with different orders, several bit rates and pulse shape duty-cycles. In addition, we will also assess the degradation of the 16-QAM coherent receiver performance due to the in-band crosstalk.

This dissertation will also investigate the accuracy of the Error Vector Magnitude (EVM) method in the presence of in-band crosstalk by comparing its estimates with the estimates obtained using Monte-Carlo (MC) simulation.

1.4 Dissertation Organization

The dissertation is organized as follows. The second chapter presents an introduction to coherent detection and its main theoretical concepts. The models for the electrical and optical components of the coherent detection receiver are provided and the methods for evaluating the bit error rate (BER) are described. Additionally, some MC simulation aspects are discussed.

In the third chapter, the filters used in this work are described, and the simulator validation is performed. The optimization of the filters bandwidths is also performed using the MC simulator and the EVM, for the 4-QAM and 16-QAM coherent receivers in presence of amplified spontaneous emission (ASE) noise. This optimization allows to choose the best optical and electrical filters configuration that minimizes the BER of the receiver in presence of ASE noise.

The fourth chapter introduces the crosstalk impairment theoretically and presents the model used in this work to address its impact. Then, the coherent receiver performance for the 4-QAM modulation format in the presence of in-band crosstalk is assessed, considering M-QAM interferers with different duty-cycles, different modulation formats and different bit rates. Additionally, the impact of the time misalignment and the phase difference between the selected and interfering signals is also studied and its influence on the coherent detection performance is discussed. Moreover, the influence of the in-band crosstalk on the 16-QAM coherent receiver performance is also investigated.

Finally, the fifth chapter summarizes the main conclusions obtained in this work and provides some ideas for possible future work.

1.5 Main Original Contributions

In the analysis performed in this work, several original contributions were introduced relative to other studies in the field. In the following, the most important contributions of this work are presented:

- Comparison between the optimization of the -3 dB bandwidth for several non-ideal filters using the DEC and EVM methods, considering the QPSK and 16-QAM coherent receivers.
- Assessment of the impact of the in-band crosstalk on the coherent receiver performance, considering interferers with different modulation format orders and same bit rate as the selected signal.
- Assessment of the impact of the in-band crosstalk on the coherent receiver performance, considering interferers with different duty-cycles but with the same modulation format order as the selected signal.
- Comparison between the assessment of the OSNR penalty at the M-QAM coherent receiver due to in-band crosstalk using the DEC and EVM methods.
- Analysis of the influence of the time misalignment and phase difference between selected and interfering signals on the OSNR penalty variation due to in-band crosstalk.

Chapter 2

Optical Coherent Detection

2.1 Introduction

Nowadays, optical coherent detection is the chosen technology for the implementation of higher data rate networks receivers since it enables the detection of higher SE optical signals. By adding the possibility of PDM signal detection, it is the elected detection technology for 100 Gbps or higher capacity networks [1].

In section 2.2, the coherent detection technique is presented and its advantages are described. Section 2.3 is dedicated to some relevant simulation aspects, such as the generation of the data sequences and its temporal and frequency representations. Also the MC simulation used in this work to study the coherent receiver is described. Then, in section 2.4, the signal modulation formats and duty-cycles considered in this dissertation are presented.

The coherent receiver model is thoroughly described in section 2.5, with a particular emphasis on each component of the coherent receiver. Section 2.6 is dedicated to the analytic description of the coherent detected received signal corrupted by ASE noise. Lastly, in section 2.7, the simulation methods used in this work to assess the coherent receiver performance are described.

2.2 Coherent Detection

The optical coherent detection provides a great flexibility by enabling the reception of higher modulation formats, where the optical signal has its information encoded in the in-phase (I) and quadrature (Q) components [22], allowing to detect modulation formats with high SE such as M-ary Phase-Shift Keying (M-PSK) or M-QAM signals. Alongside with the photodiodes and delay line interferometers (DLI)s, the coherent receiver includes a local oscillator (LO), which signal is coupled with the incoming signal. And the demodulation of the received signal is made in the electrical domain, reducing the optical complexity due to the need of the

DLIs to convert phase to intensity information [6], which is demanded in the demodulation of DPSK or DQPSK optical signals. However, the coherent detection drawback is in the synchronization between the LO signal and the optical signal. Three techniques have been designed to synchronize the LO with the received optical signal. Figure 2.1 illustrates those three techniques: (a) homodyne detection, (b) intradyne detection and (c) heterodyne detection.

Figure 2.1(a) shows the detected signal spectrum after homodyne detection, where the LO frequency (ν_{LO}) is the same as the incoming signal frequency (ν_0). To synchronize the LO signal with the incoming signal, an optical phase-locked loop (OPLL) is required. However, this component is sensible to propagation delay, which makes more difficult the receiver synchronization with the optical signal carrier frequency [6]. Another option is to assume that there is a frequency difference, typically of 100 kHz between both signals [23]. This technique is called intradyne detection and is depicted in Figure 2.1(b). This method uses a free-running local oscillator and has a similar detection bandwidth to the one of homodyne detection. To use a synchronized free-running LO without requiring the use of an OPLL, improved digital signal processing (DSP) technology must be used. Moreover, with the implementation of advanced DSP hardware in recent coherent systems, in substitution of the OPLL, the compensation of the chromatic dispersion and polarization mode dispersion is more efficient, since it is performed in the electrical domain [6].

In heterodyne detection, which is depicted in Figure 2.1(c), the LO frequency is different from the incoming signal carrier frequency. In this case, the optical signal is demodulated to an intermediate frequency f_{IF} before the downconversion to baseband. The implementation of heterodyne detection is simpler than homodyne detection, however the goal of accomplishing higher data rates with high SE, discards the heterodyne detection for optical reception due to the wider bandwidth required.

Coherent detection is usually combined with the PDM technique. This multiplexing technique doubles the SE by transmitting two modulated signals in the same optical carrier frequency, but with orthogonal polarizations. Hence, this multiplexing technique doubles the SE of any modulation format. For instance, if applied together with QPSK modulation, it quadruples the transmission capacity in comparison with the OOK for the same data rate [4].

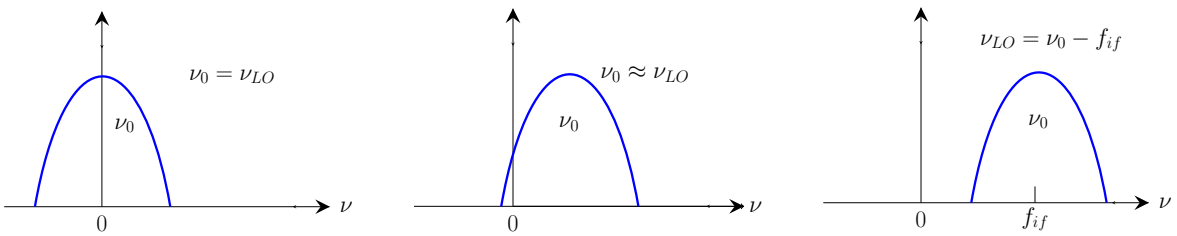

(a) Homodyne. **(b)** Intradyne. **(c)** Heterodyne.

Figure 2.1: Schematic representations of the signal spectrum after the LO beating with the signal.

The capability of receiving optical signals in which the information is encoded in amplitude, phase and polarization provides a higher spectral efficiency, and also enables the use of advanced DSP to compensate any linear impairment occurring during transmission. It remains to say that the coherent technique used in this work is the homodyne, since we will assume an ideal synchronization between the LO and the received signal.

2.3 System Simulation Aspects

In this section, the relevant aspects for the implementation of an optical communication system using computer simulation are briefly described. This description covers the generation of data sequences to represent an optical or an electrical signal and its time and frequency domain representations. Moreover, the MC simulation will also be explained.

2.3.1 Data Sequences

In computer simulations, a suitable choice of the symbols sequence is crucial for obtaining reliable results. Pseudo-random binary sequence (PRBS) are typically used to represent a binary data sequence [24]. By definition, pseudo-random implies that the binary sequence is quasi-random and involves an algorithm to produce a periodic bit pattern with a specific length [25], in order to its autocorrelation function resembles the autocorrelation function of a random binary sequence [24]. Furthermore, in order to take into account the effect of intersymbol interference (ISI) accurately on the signal, the length of the bit pattern should be longer than the communication system memory [6]. However, as the length of the sequence increases, more computational effort is required to process all the symbols [6].

Since this work simulates M-QAM signals, symbols sequences are generated based on the same principle of the PRBS. In a M-ary communication system, the symbols sequences can be generated using Galois Fields (GF) arithmetic [24], which is based on the primitive polynomial of degree m defined by [6]

$$P_m(x) = x^m + a_{m-1}x^{m-1} + ... + a_1 x + a_0 \tag{2.1}$$

where a_i is the coefficient in a finite field of q elements, $P_m(x)$ is the minimal polynomial of a finite field GF(q) which can be implemented by a shift feedback register [24]. So, for the QPSK, the primitive polynomial of GF(2^2) is

$$g(x) = x^2 + x + 1 \tag{2.2}$$

producing a sequence of 256 symbols. For 16-QAM sequences, the same $g(x)$ is used to represent the I and Q components [24] with a 512 symbols length.

Since, the proper GF to generate 64-QAM symbols sequences was not a goal of this dissertation, the Matlab function *rand* is used for generate the symbols sequences for the 64-QAM modulation format. This function produces random numbers following a uniform distribution. However, the sequence length must be long enough to characterize the ISI with accuracy. The size of the sequence of the 64-QAM modulation format used in the simulation will be investigated in section 3.4.1.3.

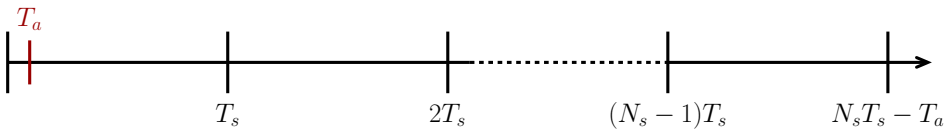

Figure 2.2: Time vector representation.

In Matlab, the symbols sequences are described in the discrete time domain or in the frequency domain. The time vector is depicted in Figure 2.2. The number of positions of the time vector is N_sN_a, where N_s is the number of simulated symbols and N_a is the number of samples per symbol. This will correspond to a continuous time, starting at the time instant $t = 0$ and finishing in $T = N_sT_s - T_a$, where T_s is the symbol time, T_a corresponds to the sampling time defined by $T_a = T_s/N_a$, and T is the overall duration of the simulated signal [24].

Figure 2.3 shows the frequency vector, which has the same number of positions than the time vector, and where f_a is the sampling frequency defined as $1/T_a$ and $\Delta f = 1/(N_sT_s)$ is the frequency resolution. The conversion of a signal in time domain to its frequency representation is computed using the *Fast Fourier Transform*, an algorithm that implements the *Discrete Fourier Transform*. Since this algorithm returns a shifted frequency vector, the Matlab function *fftshift* must be applied to rearrange the signal spectrum from $[-\frac{f_a}{2}, \frac{f_a}{2} - \Delta f]$, where the simulation bandwidth B_{sim} is as $B_{sim} = f_a - \Delta f$.

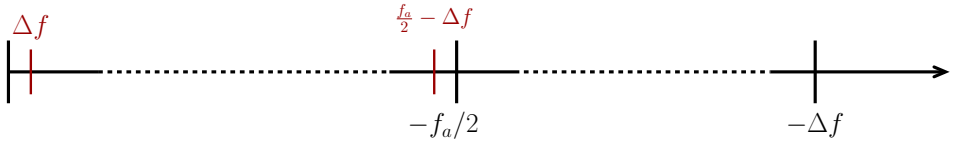

Figure 2.3: Frequency vector representation.

In the continuous time domain, the average power P_{avg} of a generic signal $E_s(t)$ is defined by [26]

$$P_{avg} = \frac{1}{T}\int_0^T |E_s(t)|^2 dt \tag{2.3}$$

In computational simulations, Equation (2.3) can be estimated using the Matlab function *trapz* which implements the trapezoidal method.

The power spectrum density (PSD) of the simulated signal is estimated using the definition of periodogram defined by [26]

$$G_E(f) = \frac{1}{T}|E_s(f)|^2 \tag{2.4}$$

2.3.2 Monte-Carlo Simulation

The MC method is a well known algorithm for statistical simulations in various scientific areas, where there is the need to describe a stochastic process. This method implements a sequence of Bernoulli trials [24], by generating random sequences of numbers based on a certain probabilistic distribution. These random sequences of numbers represent sample functions of the stochastic process intended to be studied.

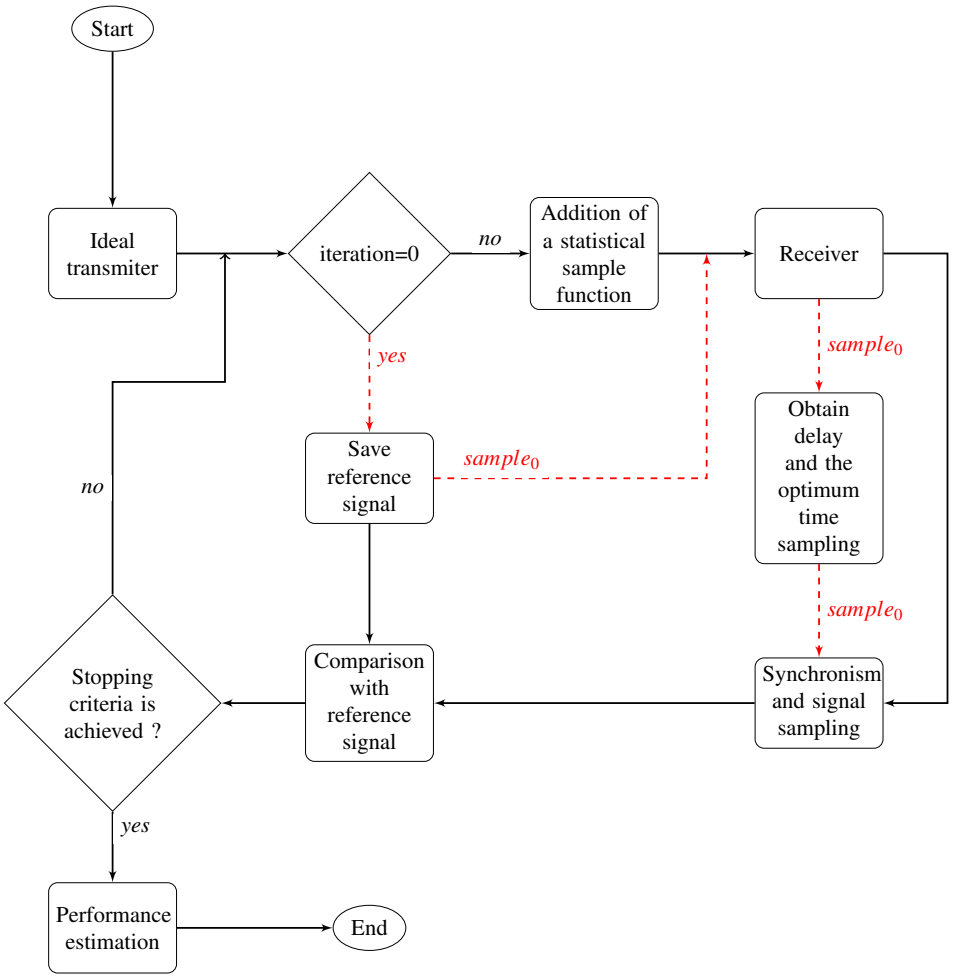

Figure 2.4: MC algorithm flow-chart.

The MC simulation will be described using the flow-chart depicted in Figure 2.4. In the first iteration of the MC simulation, an optical signal with a specific modulation format, such as M-QAM or M-PSK is generated using an ideal transmitter, and it is propagated along the receiver without the addition of any statistical sample function. This first iteration is called the $sample_0$. The detection of this sample will provide a reference signal to the receiver, in order to know which symbols were transmitted. The reference signal is also used to measure the propagation delay of the communication system, in order to assure the synchronization between received and transmitted signals. Then, on the following iterations, random sample functions of the stochastic process are generated and added to the signal, modifying the optical signal at the receiver input. At the end of each iteration, the received symbols are compared with the corresponding symbols of the reference signal, and depending of the assessment method used, the performance of the receiver is estimated. As a stopping criteria, the simulation ends when a pre-defined total number of symbols errors is achieved or a total of samples functions is generated [24].

The ASE noise will be the stochastic process impairing the coherent receiver performance in chapter 3, and in chapter 4, the stochastic processes will be the ASE noise and the in-band crosstalk.

2.4 Transmitter Description

In optical coherent communication systems, the generation of the optical signal is usually accomplished using a laser followed by an IQ modulator [27]. For the sake of simplicity, we will assume an ideal transmitter throughout this work. The optical signal is parametrized by its modulation format, symbol duration, duty-cycle, pulse shape and average power.

2.4.1 Modulation Formats and Constellations

In this subsection, the generation of optical signals with M-ary QAM modulation format is explained. The structure of a M-ary transmitter is shown in Figure 2.5, where the symbols sequence is fed into the mapping block. The main function of this block is to assign at its outputs the amplitude levels corresponding to the

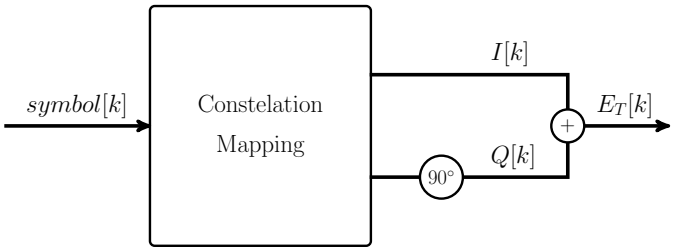

Figure 2.5: Ideal IQ transmitter.

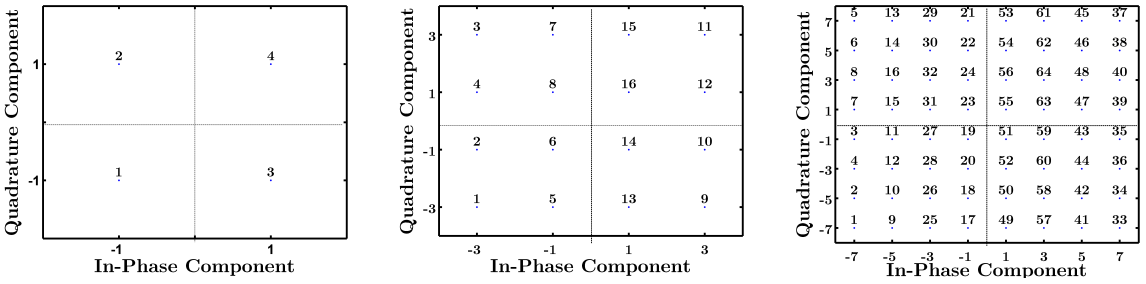

(a) 4-QAM/QPSK. **(b)** Square 16-QAM. **(c)** Square 64-QAM.

Figure 2.6: Ideal constellations for (a) QPSK, (b) 16-QAM and (c) 64-QAM mappings signals.

in-phase $I[k]$ and quadrature $Q[k]$ components [26] accordingly to the sequence of symbols at its input,

$$\begin{aligned} I[k] &= \pm 1, \pm 3, ..., \pm(\sqrt{M}-1) \\ Q[k] &= \pm 1, \pm 3, ..., \pm(\sqrt{M}-1) \end{aligned} \tag{2.5}$$

The signal in the I branch is added to the 90° shifted signal in the Q branch resulting in the complex symbol sequence $E_T[k] = I[k] + jQ[k]$.

Tables 2.1, 2.2 and 2.3 present the mapping used between bits and symbols at the output of the IQ mapper and Figure 2.6 shows the constellations for the (a) 4-QAM, (b) 16-QAM and (c) 64-QAM modulation formats.

Figure 2.7 shows the power spectral density (PSD) of the M-QAM modulated signals having an average power of 1 mW and a 50 Gbps bit rate per polarization, which corresponds to a 100 Gbps signal when using PDM, for (a) QPSK, (b) 16-QAM and (c) 64-QAM signals. For the QPSK modulation format, the bandwidth

Symbol	bits	$E_T[k]$
1	00	$-1-j$
2	01	$-1+j$
3	11	$1-j$
4	10	$1+j$

Table 2.1: QPSK mapping.

Symbol	bits	$E_T[k]$	Symbol	bits	$E_T[k]$
1	0000	$-3-3j$	9	1000	$3-3j$
2	0001	$-3-j$	10	1001	$3-j$
3	0010	$-3+3j$	11	1010	$3+3j$
4	0011	$-3+j$	12	1011	$3+j$
5	0100	$-1-3j$	13	1100	$1-3j$
6	0101	$-1-j$	14	1101	$1-j$
7	0110	$-1+3j$	15	1110	$1+3j$
8	0111	$-1+j$	16	1111	$1+j$

Table 2.2: 16-QAM mapping.

Symbol	bits	$E_T[k]$	Symbol	bits	$E_T[k]$	Symbol	bits	$E_T[k]$	Symbol	bits	$E_T[k]$
1	000000	$-7-7j$	17	010000	$-j-7j$	33	100000	$7-7j$	49	110000	$1-7j$
2	000001	$-7-5j$	18	010001	$-j-5j$	34	100001	$7-5j$	50	110001	$1-5j$
3	000010	$-7-j$	19	010010	$-j-j$	35	100010	$7-j$	51	110010	$1-j$
4	000011	$-7-3j$	20	010011	$-j-3j$	36	100011	$7-3j$	52	110011	$1-3j$
5	000100	$-7+7j$	21	010100	$-j+7j$	37	100100	$7+7j$	53	100100	$1+7j$
6	000101	$-7+5j$	22	010101	$-j+5j$	38	100101	$7+5j$	54	100101	$1+5j$
7	000110	$-7+j$	23	010110	$-j+j$	39	100110	$7+j$	55	100110	$1+j$
8	000111	$-7+3j$	24	010111	$-j+3j$	40	100111	$7+3j$	56	100111	$1+3j$
9	001000	$-5-7j$	25	011000	$-3-7j$	41	101000	$5-7j$	57	111000	$3-7j$
10	001001	$-5-5j$	26	011001	$-3-5j$	42	101001	$5-5j$	58	111001	$3-5j$
11	001010	$-5-j$	27	011010	$-3-j$	43	101010	$5-j$	59	111010	$3-j$
12	001011	$-5-3j$	28	011011	$-3-3j$	44	101011	$5-3j$	60	111011	$3-3j$
13	001100	$-5+7j$	29	011100	$-3+7j$	45	101100	$5+7j$	61	111100	$3+7j$
14	001101	$-5+5j$	30	011101	$-3+5j$	46	101101	$5+5j$	62	111101	$3+5j$
15	001110	$-5+j$	31	011110	$-3+j$	47	101110	$5+j$	63	111110	$3+j$
16	001111	$-5+3j$	32	011111	$-3+3j$	48	101111	$5+3j$	64	111111	$3+3j$

Table 2.3: 64-QAM mapping.

of the main lobe is 50 GHz (Figure 2.7(a)) and the SE is 2 bits/s/Hz; for the 16-QAM (Figure 2.7(b)), the SE is 4 bits/s/Hz with 25 GHz of main lobe bandwidth, and for the 64-QAM (Figure 2.7(c)) the SE is 6 bits/s/Hz with a main lobe bandwidth 16.67 GHz.

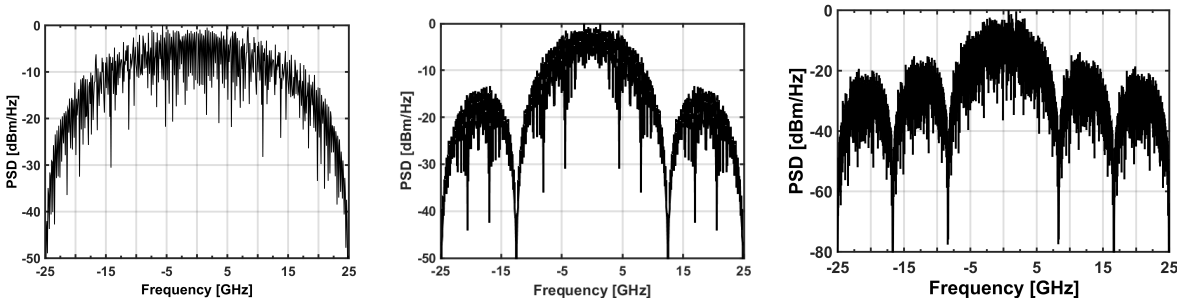

(a) QPSK. **(b)** 16-QAM. **(c)** 64-QAM.

Figure 2.7: PSD of the simulated (a) 4-QAM, (b) 16-QAM and (c) 64-QAM signals.

2.4.2 Duty-Cycle

The shape of the optical pulse can affect significantly the performance of the optical fiber communication system [6]. Assuming ideal synchronization at the receiver, we will study four pulse shapes - the return-to-zero (RZ) with duty- cycles of 66, 50 and 33%, and the non return-to-zero (NRZ) with a 100% duty-cycle.

The rectangular NRZ pulse shape is characterized by having the optical power of each symbol constant throughout the duration of the symbol time. This format has the advantage of having a smaller bandwidth and therefore is commonly used in systems where bandwidth requirements are stringent, for instance in WDM channels [27]. Its main disadvantage is that is highly vulnerable to dispersion and nonlinear effects caused by

fiber transmission [27]. The RZ format is characterized for having the null optical power before the symbol time is over. There are several variants of RZ pulse, depending on the T_p/T_s ratio, referred as the duty-cycle, where T_p is the pulse duration and $T_p < T_s$. The duty-cycle can vary depending on the transmission goals because it affects directly the signal bandwidth. For instance, for a duty-cycle of 50%, the corresponding bandwidth will be twice the NRZ signal bandwidth. Therefore, this pulse shape, when applied in WDM systems, reduces the SE of the transmission, since it demands a larger separation between two consecutive WDM signals [28].

Figure 2.8 shows a (a) rectangular NRZ signal and a (b) rectangular RZ signal with 50% duty-cycle, as a function of the normalized symbol time, and the bandwidth of the NRZ and RZ50 are depicted in (c) and (d), respectively.

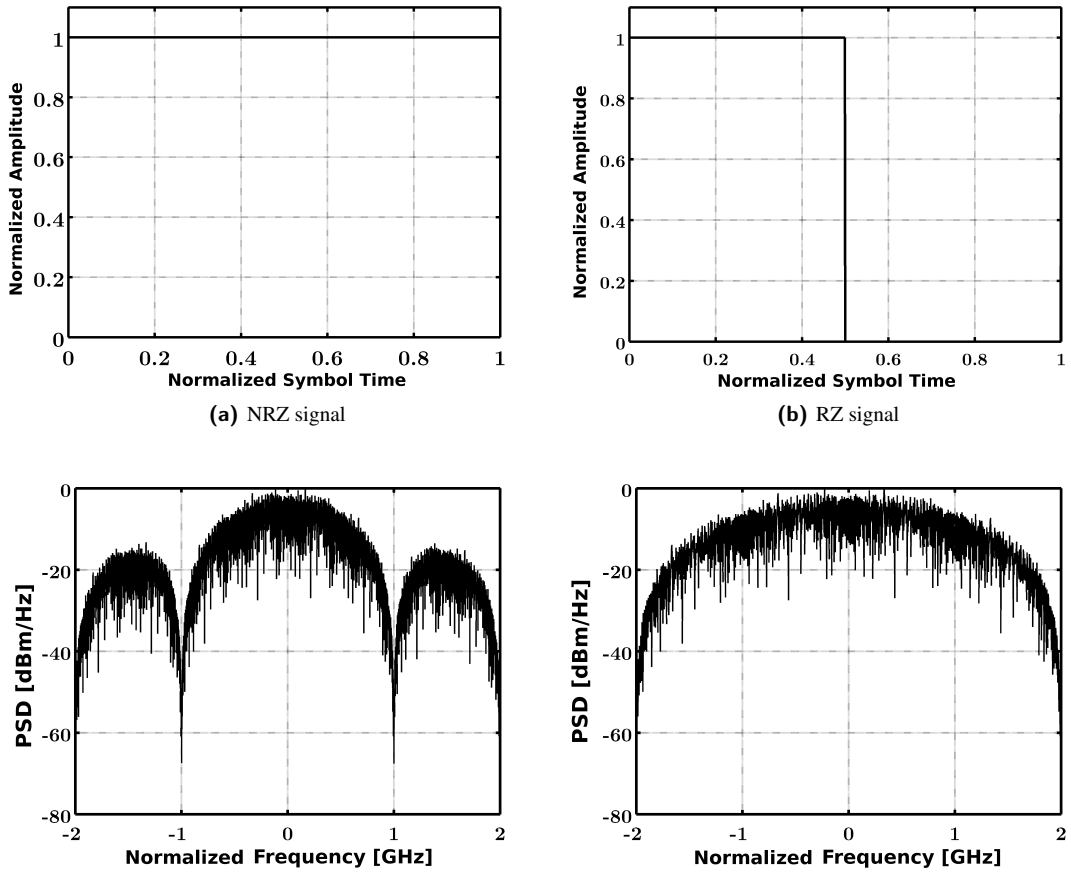

(a) NRZ signal

(b) RZ signal

(c) NRZ PSD

(d) RZ 50% PSD

Figure 2.8: Temporal representation of a (a) NRZ and (b) RZ with 50% duty-cycle pulse shapes and its respective PSDs, (c) and (d).

2.5 Coherent Receiver Model

In this section, the model used in this work for the coherent receiver with PDM is described. Figure 2.9 depicts the block diagram of the coherent receiver. The lowpass equivalent of the PDM signal, $E_{PDM}(t)$, at the coherent receiver input is defined as

$$E_{PDM}(t) = E_{T,x}(t)\hat{x} + E_{T,y}(t)\hat{y} \tag{2.6}$$

where $E_{T,x}(t)$ and $E_{T,y}(t)$ are the transmitted optical signals in the orthogonal polarizations, which directions are defined by the unit vectors $\hat{x}$ and $\hat{y}$. $N(t)$ represents the lowpass equivalent of the ASE noise in both polarizations and it will be described in the next subsection.

The model in Figure 2.9 consists of an optical filter (whose characterization will be made in chapter 3), two polarization beam splitters (PBSs) and two Quadrature Front-ends (QFs). The optical amplifier is considered in Figure 2.9, as the addition of the noise to the signal. One PBS is used to split the PDM incoming signal having ASE noise in both polarizations $E_{0,x}(t)+N_{0,x}(t)$ and $E_{0,y}(t)+N_{0,y}(t)$, which will be detected in their respective QF. The PBS is also applied to the LO signal, in order to separate its two polarizations: $E_{LO,x}$ and $E_{LO,y}$. The goal of the QF is to detect individually the I and Q components of the input signal. At the output of the QF, the I and Q components, in each polarization, are added to form the currents $I_x(t)$ and $I_y(t)$.

The following subsections describe each component of the coherent receiver with more detail.

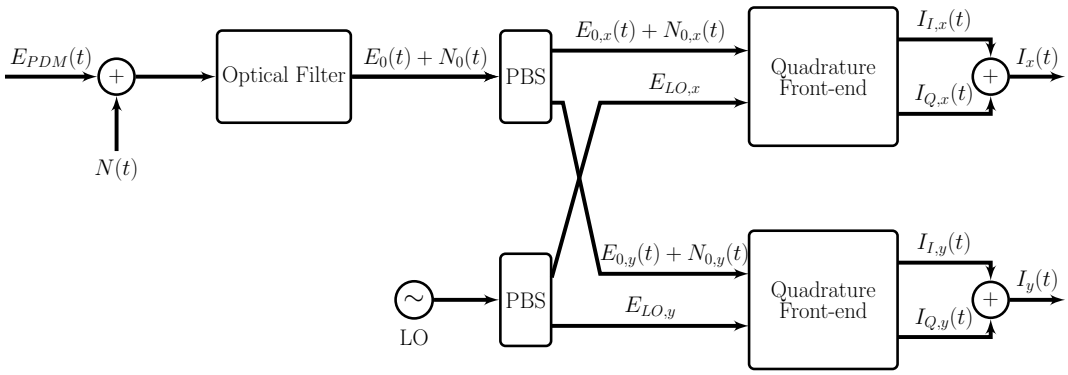

Figure 2.9: Schematic block diagram of a PDM coherent receiver with an optical quadrature frontend.

2.5.1 Optical Amplification

On an optical network, the fiber transmission media causes signal attenuation, as well as several network components, like multiplexers/demultiplexers, couplers and ROADMs. So, signal amplification is required to compensate those losses [7], [29].

There are three main types of optical amplifiers (OA): Erbium-Doped Fiber Amplifier (EDFA), Semiconductor Optical Amplifiers and Raman amplifiers. The most commonly used amplifier is the EDFA, since it can

achieve a gain of about 30 dB and operates in the C band (1530-1565 nm), the wavelength band normally used for optical communications [29]. However, the amplification also adds ASE noise to the signal [7]. In lumped amplification, the ASE noise is accumulated along a chain of cascaded OAs and the resulting ASE noise power of all the amplifiers can be measured at the end of the fiber link using the OSNR, which is defined by

$$\text{OSNR} = \frac{P_{in}}{P_{ASE}} \tag{2.7}$$

where P_{in} is the accumulated power of the signal summed over the two states of polarization [30] and P_{ASE} is the average ASE noise power, which is defined, for both noise polarizations, by

$$P_{ASE} = 2N_{ASE}B_{OSA} \tag{2.8}$$

where B_{OSA} is the Optical Spectrum Analyzer (OSA) bandwidth with the typical value of 12.5 GHz [25]. The OSA is a measurement instrument that is used to evaluate the OSNR at a determined wavelength and B_{OSA} is related to the simulation bandwidth B_{sim} by [25]

$$B_{OSA} = \frac{B_{sim}P_{ASE}}{2P_n} \tag{2.9}$$

where P_n is the ASE noise power used in the simulation. The ASE noise PSD, of one polarization, is given by

$$N_{ASE} = n_{sp}h\nu_0.(g-1) \tag{2.10}$$

where n_{sp} is the spontaneous emission noise factor, h is the Planck constant[1], and g is the power gain.

The ASE noise, in each polarization, $N_{ASE}(t)$, is considered to be an Additive White Gaussian Noise (AWGN), which can be expressed by its lowpass equivalent signal

$$N_{ASE,m}(t) = \frac{1}{\sqrt{2}}\left(N_I(t) + jN_Q(t)\right) \qquad , m = x \text{ or } y \tag{2.11}$$

where $N_I(t)$ and $N_Q(t)$ are respectively, the I and Q components of the ASE noise field. Therefore

$$N(t) = N_{ASE,x}(t)\hat{x} + N_{ASE,y}(t)\hat{y} \tag{2.12}$$

The ASE noise has a zero mean and its variance is defined by

$$E[N_{ASE}(t)N^*_{ASE}(t')] = N_0\delta(t-t') \tag{2.13}$$

[1] Planck's constant $h = 6.62606957 * 10^{-34} m^2 kg/s$

where $E[.]$ is the expected value and $\delta(t)$ represents the Dirac delta function. The property

$$E[N_{ASE}(t).N_{ASE}(t')] = 0 \tag{2.14}$$

is also useful to the derivations presented in this work.

2.5.2 Local Oscillator

The LO is an essential component of the coherent receiver, which signal is required to be mixed with the incoming signal, allowing the recover of the information encoded in the I and Q components of the received optical signal [23]. In order to maximize the coherent receiver performance, the LO frequency must be as close as possible to the optical carrier frequency [23]. Furthermore, if the LO is tunable, it can be equivalent to an ultranarrow WDM optical filter at the front of the coherent receiver [31].

In this work, the LO is considered synchronized with the optical carrier frequency and the intensity noise is neglected. The electrical field of LO signal is defined as:

$$E_{LO}(t) = \sqrt{P_{LO}}e^{j\phi_{LO}(t)} \tag{2.15}$$

where $\phi_{LO}(t)$ is the phase of the LO laser signal and P_{LO} is the LO optical power, which is typically 30 dB higher than the received signal optical power [23].

2.5.3 Quadrature Front-End

Each OFQ, in Figure 2.9 is formed by a 2 x 4 90° Hybrid and two balanced photodetectors followed by a post-detection filter, for reducing the noise and ISI after photodetection [6]. In the following, the model used in this work for these components will be described.

2.5.3.1 Hybrid

There are various possibilities of implementing a hybrid as illustrated in Figure 2.10 [6]. The most common and commercially available configuration is the one composed by four 3 dB couplers, (Figure 2.10(a)). The 90° phase shift in the lower branch guarantees orthogonality between the two branches, and allows the detection of the I and Q signal components.

Another alternative to implement this hybrid is the 4 x 4 Multi-Mode interference (MMI) coupler, which configuration is depicted in Figure 2.10(b). This component is constructed by dimensioning the waveguides that constitute the device in order to provide the phase relations required by a 90°hybrid. Furthermore, the balanced

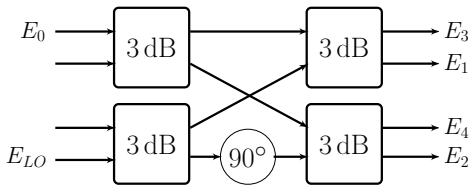

(a) Hybrid with 3 dB coupler.

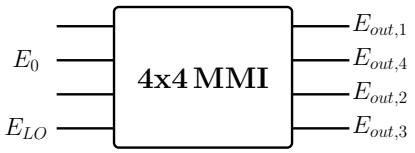

(b) MMI 4x4.

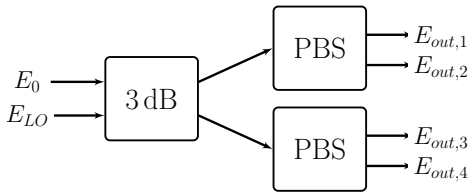

(c) Integrated device.

Figure 2.10: Different configurations of a hybrid.

photodetectors can be integrated, which means that the QF can be fully implemented ona chip, using a MMI coupler [6]. Another interesting characteristic of MMI couplers is their wide bandwidth, which makes them a suitable component for WDM, however this device is not yet commercially available.

The third option is an integrated device of discrete components, composed by two PBS and a 3 dB coupler, as shown in Figure 2.10(c). However, this device requires specific polarizations states for each input signal [6].

In this work, the 2 x 4 90° hybrid depicted in Figure 2.10(a) will be modeled, since it is the most commonly used in optical communications.

The model of the hybrid used in this dissertation is described in the following. We start by introducing the 3 dB coupler. This component is a special case of a directional coupler, which is a passive device constructed from two coupled transmission lines, set closely together such that the energy passing through one arm of the coupler is coupled to the field in the other arm. Structurally, the directional coupler has two inputs and two outputs, intermediated by the coupling region with length L_c [28], as depicted in Figure 2.11. Equation (2.16) describes the output electrical fields of the directional coupler [27],

$$\begin{bmatrix} E_{o,1}(t) \\ E_{o,2}(t) \end{bmatrix} = \begin{bmatrix} \sqrt{\rho} & j\sqrt{1-\rho} \\ j\sqrt{1-\rho} & \sqrt{\rho} \end{bmatrix} \begin{bmatrix} E_{i,1}(t) \\ E_{i,2}(t) \end{bmatrix} \tag{2.16}$$

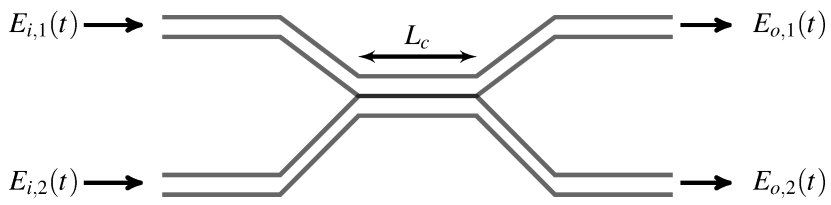

Figure 2.11: Directional coupler.

where ρ is the power coupling coefficient. To get a 3 dB coupler, ρ must equal 0.5, so, the two electric fields at the output of the 3 dB coupler are given by:

$$\begin{aligned} E_{o,1}(t) &= \frac{1}{\sqrt{2}}(E_{i,1}(t) + jE_{i,2}(t)) \\ E_{o,2}(t) &= \frac{1}{\sqrt{2}}(jE_{i,1}(t) + E_{i,2}(t)) \end{aligned} \tag{2.17}$$

An important feature of the 3 dB coupler is to provide two coupled outputs with an 180° shift phase difference between them, and is often known as an 180° hybrid. The 3 dB coupler is a very versatile device since it can be applied to different functions. If only one input is fed, the result is a power divider. If the two inputs are active and only one output inactive, we have a power combiner. A power divider is obtained by making $E_{i,2}(t) = 0$ in Equation (2.17), and the output electric fields become:

$$\begin{aligned} E_{o,1}(t) &= \frac{E_{i,1}(t)}{\sqrt{2}} \\ E_{o,2}(t) &= j\frac{E_{i,1}(t)}{\sqrt{2}} \end{aligned} \tag{2.18}$$

A similar result is obtained by making $E_{i,2}(t)$ active and $E_{i,1}(t) = 0$. By considering Figure 2.10(a) and taking the proper input electrical fields definitions, the transfer function of the 2 x 4 90° hybrid is [6]:

$$\begin{bmatrix} E_1(t) \\ E_2(t) \\ E_3(t) \\ E_4(t) \end{bmatrix} = \frac{1}{2}\begin{bmatrix} 1 & -1 \\ j & j \\ j & -1 \\ -1 & j \end{bmatrix}\begin{bmatrix} E_s(t) \\ E_{LO}(t) \end{bmatrix} \tag{2.19}$$

2.5.3.2 Polarization Beam Splitter

The PBS consists of a fiber-based Mach-Zehnder interferometer (MZI) [32], consisting of two 3 dB couplers with two delay lines as shown in Figure 2.12 [25].

This device is used to separate the input optical signal into horizontal and vertical polarization components. In ideal conditions, the input PDM signal power is equally split between the two outputs of the PBS [25], i.e. $P_p = P_{in}/2$, where P_p is the average signal power of each PBS output. Since the signal power is halved, the respective P_{ASE} is proportionally reduced, which means $P_{ASE,p} = P_{ASE}/2 = N_{ASE}B_{OSA}$. Therefore, the OSNR of each polarization (OSNR_p) is given by [30]

$$\text{OSNR}_p = \frac{P_p}{N_{ASE}B_{OSA}} = \frac{P_{in}}{2N_{ASE}B_{OSA}} \tag{2.20}$$

where OSNR_p defines the OSNR in each polarization, which means that the OSNR after an ideal PBS for a PDM ideal optical signal is the same as if the optical signal has been transmitted in a single polarization.

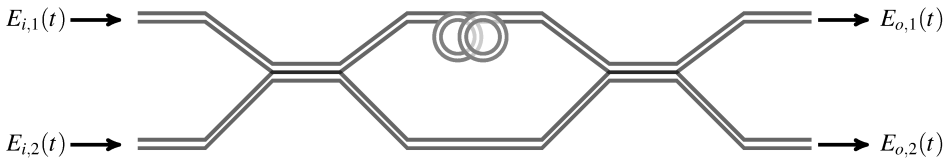

Figure 2.12: Mach-Zehnder interferometer

2.5.3.3 Photodetector

In order to recover all the information from an optical signal, an optical-electrical conversion has to be performed using a photodetector. These devices are made of semiconductors materials to respond to the requirements demanded by a lightwave system: high sensitivity, low noise, fast response, high reliability and a size compatible with the fiber core [7]. The operation of a photodetector can be described by its responsivity defined by [7]:

$$R_\lambda = \frac{I_p(t)}{P_{in}(t)} \qquad [A/W] \tag{2.21}$$

where $I_p(t)$ is the current produced by the incident optical power $P_{in}(t)$ on the photodetector. In this work, for simplification, a unit responsivity, i.e. $R_\lambda = 1\,A/W$ will be assumed. Hence $P_{in}(t) = |E_{in}(t)|^2$, where $E_{in}(t)$ is the electrical field incident on the photodetector.

2.5.3.4 Post-Detection Electrical Filter

All optical receivers have a low-pass filter for reducing the noise and ISI after photodetection [6]. This post-detection filter also models the frequency limitations of the photodetector.

The filter design aims maximizing the electrical Signal-to-Noise (SNR) at the decision circuit input, so the shape of the filter must be closely, or ideally, the same as the incoming signal. A filter with this property is called a *matched filter* [33]. In fact, one of the most important objective in the design of filters is that, its shape must be as close to the ideal shape as possible. The 4^{th}-order Super Gaussian or the 5^{th}-order Bessel filter are some examples of filters typically used [34], [35].

2.6 Detected Signal Statistics

This section describes the theory and the mathematical analysis behind the detection of the electrical I and Q components of the optical signal in one polarization direction.

Figure 2.13 depicts the model of the QF used in this work. Therefore, by taking Equation (2.19), the optical

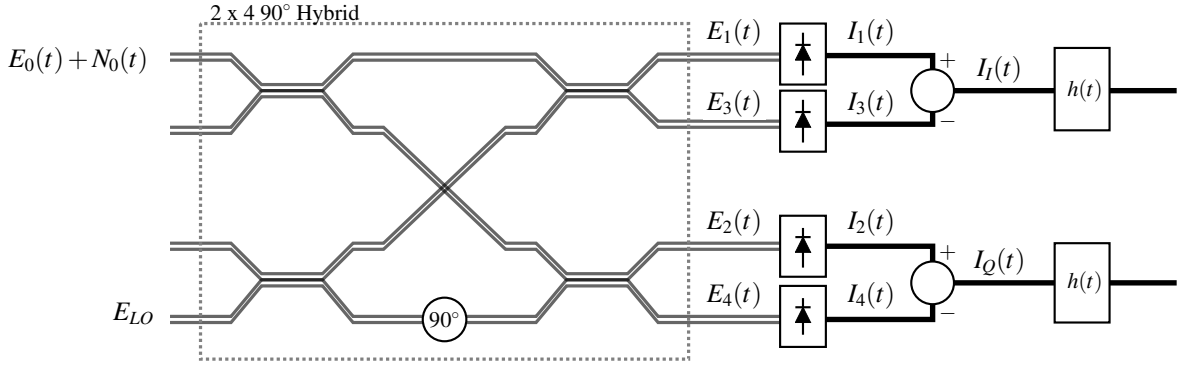

Figure 2.13: Setup of a typical QF based on the configuration presented in Figure 2.9.

fields at the four photodetectors inputs are described by:

$$\begin{aligned}
E_1(t) &= \frac{1}{2}\left[(E_0(t)+N_0(t)) - E_{LO}(t)\right] \\
E_2(t) &= \frac{j}{2}\left[(E_0(t)+N_0(t)) + E_{LO}(t)\right] \\
E_3(t) &= \frac{1}{2}\left[j(E_0(t)+N_0(t)) - E_{LO}(t)\right] \\
E_4(t) &= \frac{1}{2}\left[-(E_0(t)+N_0(t)) + jE_{LO}(t)\right]
\end{aligned} \tag{2.22}$$

After square-law photodetection, the output photocurrent in each photodetector is written, respectively, as:

$$\begin{aligned}
I_1(t) &= \frac{1}{4}\left|(E_0(t)+N_0(t)) + E_{LO}(t)\right|^2 \\
I_2(t) &= \frac{1}{4}\left|(E_0(t)+N_0(t)) + jE_{LO}(t)\right|^2 \\
I_3(t) &= \frac{1}{4}\left|(E_0(t)+N_0(t)) - E_{LO}(t)\right|^2 \\
I_4(t) &= \frac{1}{4}\left|(E_0(t)+N_0(t)) - jE_{LO}(t)\right|^2
\end{aligned} \tag{2.23}$$

By developing the absolute square of complex number in each term, we have:

$$\begin{aligned}
I_1(t) &= \frac{1}{4}\left[\left[|(E_0|^2 + |N_0|^2 + 2\Re\{E_0N_0^*\}\right] + |E_{LO}|^2 - 2\Re\{E_0E_{LO}^* + N_0E_{LO}^*\}\right] \\
I_2(t) &= \frac{1}{4}\left[\left[|(E_0|^2 + |N_0|^2 + 2\Re\{E_0N_0^*\}\right] + |E_{LO}|^2 + 2\Re\{E_0E_{LO}^* + N_0E_{LO}^*\}\right] \\
I_3(t) &= \frac{1}{4}\left[\left[|(E_0|^2 + |N_0|^2 + 2\Re\{E_0N_0^*\}\right] + |E_{LO}|^2 - 2\Im\{E_0E_{LO}^* + N_0E_{LO}^*\}\right] \\
I_4(t) &= \frac{1}{4}\left[\left[|(E_0|^2 + |N_0|^2 + 2\Re\{E_0N_0^*\}\right] + |E_{LO}|^2 + 2\Im\{E_0E_{LO}^* + N_0E_{LO}^*\}\right]
\end{aligned} \tag{2.24}$$

where $\Re\{Z\}$ and $\Im\{Z\}$ stands for, respectively, the real part and the imaginary part of a complex number Z, with the complex conjugate represented by Z^*. Next, the I and Q components are defined as: $I_I(t) = I_2(t) - I_1(t)$

(in-phase) and $I_Q(t) = I_4(t) - I_3(t)$ (quadrature), which gives [30]:

$$I_I(t) = \Re\{E_0(t)E_{LO}^*(t) + N_0(t)E_{LO}^*(t)\} \tag{2.25}$$

$$I_Q(t) = \Im\{E_0(t)E_{LO}^*(t) + N_0(t)E_{LO}^*(t)\} \tag{2.26}$$

Examining Equations (2.25) and (2.26), the term $E_0(t)E_{LO}^*(t)$ is the desired received electrical signal and the right hand side term is the beating between the LO and the optical ASE noise field (LO-ASE), which is the only significant beating noise, since the ideal balanced detection eliminates the ASE-ASE noise beating and the signal-ASE noise beating [30].

For simplicity of notation, the time dependence in the equations will be omitted for the rest of the subsection.

The power of LO-ASE noise beating is given by its variance. The expression of the variance is given by

$$\sigma_x^2 = E[(X - m_x)^2] \tag{2.27}$$

where X is the random variable and m_x is the mean value. Since the ASE noise has zero mean, as described in section 2.5.1, the variance of the LO-ASE beat noise in the in-phase component is simplified to

$$\sigma_{I_I,LO}^2 = E[|\Re\{N_0E_{LO}^*\} * h(t)|^2] \tag{2.28}$$

where * is the convolution operator. By writing the convolution in its integral form, the variance becomes

$$\sigma_{I_I,LO}^2 = E\left[\left|\int \Re\{N_0(\tau)E_{LO}^*\}h(t-\tau)d\tau\right|^2\right] \tag{2.29}$$

By applying the propriety $|X|^2 = XX^*$ and then by expressing the real part in the sum of conjugated terms, we have

$$\sigma_{I_I,LO}^2 = E[\int \frac{N_0(\tau)E_{LO}^* + N_0^*(\tau)E_{LO}}{2}h(t-\tau)d\tau \int \frac{N_0^*(\tau')E_{LO} + N_0(\tau')E_{LO}^*}{2}h(t-\tau')d\tau'] \tag{2.30}$$

By multiplying the two integrals, we will have

$$\begin{aligned}\sigma_{I_I,LO}^2 = \frac{1}{4}E\Bigg[\iint N_0(\tau)N_0^*(\tau')E_{LO}E_{LO}^*h(t-\tau)h(t-\tau')d\tau d\tau' + \iint N_0^*(\tau)N_0(\tau')E_{LO}^*E_{LO} \\ h(t-\tau)h(t-\tau')d\tau d\tau' + 2\Re\{\iint N_0(\tau)N_0(\tau')E_{LO}E_{LO}^*h(t-\tau)h(t-\tau')d\tau d\tau'\}\end{aligned} \tag{2.31}$$

by making use of Equation (2.15), we arrive to

$$\sigma^2_{I_I,LO} = P_{LO}\Re\left\{\iint E\left[N_0(\tau)N_0^*(\tau')\right]h(t-\tau)h(t-\tau')d\tau d\tau'\right\} \tag{2.32}$$

By using Equation (2.13), Equation (2.32) becomes

$$\sigma^2_{I_I,LO} = P_{LO}\Re\left\{\iint N_o\delta(\tau-\tau')h(t-\tau)h(t-\tau')d\tau d\tau'\right\} \tag{2.33}$$

Now, by applying the convolution property of dirac delta, i.e. $\int v(t)\delta(t-t_d)dt = v(t_d)$ [26] we arrive to

$$\sigma^2_{I_I,LO} = P_{LO}\Re\left\{\int N_o h(t-\tau')h(t-\tau')d\tau'\right\} \tag{2.34}$$

Finally, assuming $\int h^2(t)dt = \int |H(f)|^2 df = 2B_h$, the final expression of the variance of the LO-ASE beating noise is

$$\sigma^2_{I_I,LO} = 2P_{LO}N_oB_h \tag{2.35}$$

The same procedure can be applied for calculating the variance of the LO-ASE beating noise in the Q component, $\sigma^2_{I_Q,LO}$.

2.7 Performance Evaluation Methods

Since the main goal of this work is to study the performance of the coherent receiver, in order to quantify its performance, we use the BER. In the following pages, we will describe the methods used in this work to obtain the BER of the optical communication system: the theoretical BER based on the Gaussian distribution, the Direct Error Counting (DEC) and the EVM.

2.7.1 Theoretical BER

Since the modulation format used in the simulation is the QAM, the theoretical BER for a M-ary QAM signal is defined as [33]

$$BER_{QAM} = 2\left(1-\frac{1}{\sqrt{M}}\right)Q\left(\sqrt{\frac{3}{(M-1)}\text{SNR}}\right) \tag{2.36}$$

where $Q(x)$ is the Q function defined by [26]

$$Q(x) = \frac{1}{\sqrt{2\pi}} \int_x^{\infty} exp(-t^2/2)dt \tag{2.37}$$

Equation (2.36) provides the required electrical SNR to achieve a determined BER. By expressing the SNR as a function of the OSNR, we have [6]

$$SNR = \frac{2\,\mathrm{OSNR}\,B_{OSA}}{R_s} \tag{2.38}$$

where R_s is the symbol rate. Then, Equation (2.36) can be rewritten as

$$BER_{QAM} = 2\left(1 - \frac{1}{\sqrt{M}}\right) Q\left(\sqrt{\frac{6\,\mathrm{OSNR}\,B_{OSA}}{(M-1)R_s}}\right) \tag{2.39}$$

2.7.2 Direct Error Counting

This is the most common and simplest simulation method for the performance assessment of an optical communication system, since is based on the definition of the BER, i.e. the ratio of the number of bit errors over the total number of transmitted bits. By assuming Gray mapping, the BER is obtain by direct error counting using

$$BER = \frac{N_e}{N_{MC} N_s (\log_2 M)} \tag{2.40}$$

where N_e is the number of counted errors at the decision circuit, N_{MC} is the number of generated sample functions.

With a large number of counted errors, this method is very accurate, however, it demands a large number of sample functions, resulting in a huge computational effort, for very low error probabilities ($\leq 10^{-5}$) [36].

2.7.3 Error Vector Magnitude

EVM is a very useful tool for evaluating the received signal quality, when the information is mapped in amplitude and phase, because it compares the received constellation with the transmitted constellation [37]. Since each symbol corresponds to a complex number, the constellation diagrams are useful to visualize signals [38], as they display the signal as a two-dimensional scatter diagram in the complex plane at each symbol sampling time instant and allow to observe signal distortion or constellation spreading due to noise. In this work, the EVM method is obtained from MC simulation. For each received symbol, an error vector is defined, measuring

the difference between its point location in the received constellation and its ideal constellation location.

In order to efficiently calculate the EVM, the error vectors must be measured in a normalized constellation. The EVM is defined as the root-mean-square (rms) value as [37]

$$EVM_{rms} = \sqrt{\frac{\sum_{k=1}^{N_s} |s_o[k] - s_i[k]|^2}{\sum_{k=1}^{N_s} |s_i[k]|^2}} \tag{2.41}$$

where s_o and s_i are, respectively the magnitude of the received and transmitted symbols in the normalized constellation diagram. In order to find the BER based on the EVM measurements (BER_{EVM}), we use the expression [37]

$$BER_{EVM} = 4\frac{(1-1/\sqrt{M})}{\log_2(M)} Q\left(\sqrt{\frac{3}{(M-1)EVM_{rms}^2}}\right) \tag{2.42}$$

In the EVM assessments, the MC simulator uses the number of generated sample functions as the stopping criteria. When the simulator stops, the BER is calculated using Equation (2.42). In this situation, the EVM_{rms} will be the average of all the rms values measured for each sample function, $EVM_{rms,k}$, i.e

$$EVM_{rms} = \frac{1}{N_{MC}} \sum_{k=1}^{N_{MC}} EVM_{rms,k} \tag{2.43}$$

Equation (2.42) can be rewritten as a function of the OSNR, as the relation between the EVM_{rms} and the electrical SNR is given by [37]

$$EVM_{rms} = \sqrt{\frac{1}{\text{SNR}}} \tag{2.44}$$

Then, by making use of Equations (2.38) and (2.44), is possible to modify Equation (2.42) as follows

$$BER_{EVM} = 4\frac{(1-1/\sqrt{M})}{\log_2(M)} Q\left(\sqrt{\frac{6\,\text{OSNR}\,B_{OSA}}{(M-1)R_s}}\right) \tag{2.45}$$

In order to show the relationship between the EVM_{rms} and the BER estimation, Figure 2.14 was obtained using Equation (2.42). Note that the Equation (2.45) assumes a Gaussian distribution for the received signal statistics [39].

From Figure 2.14, it can be seen that higher EVM_{rms} leads to higher BERs. This corresponds to scenarios where there is a major difference between the received constellation and the ideal one. Also, higher modulation format orders also lead to a significant BER increase for lower EVM_{rms}, than for lower orders.

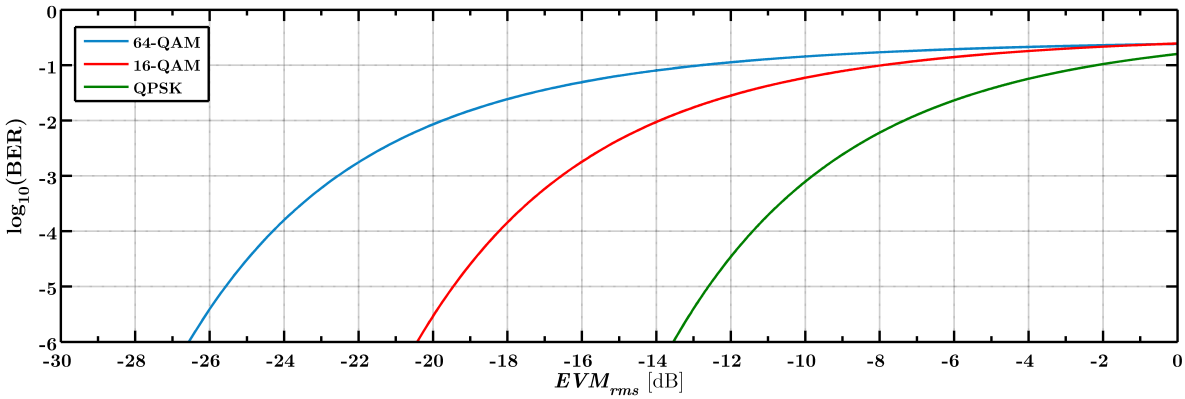

Figure 2.14: BER as a function of the EVM_{rms} in dB.

2.8 Conclusion

In this chapter, the optical coherent detection receiver and its model were described with detail. Its main advantage over direct detection is that the SE of the transmission is enhanced, since coherent receivers enables the detection of optical signals with information encoded in amplitude, phase and polarization. The disadvantages reside in a more complex structure of the receiver than in direct detection and the need of synchronization between the receiver and the optical signal carrier frequencies. However, nowadays, high developed DSPs are added to the coherent receiver to provide a simpler and more efficient receiver synchronization, and are commonly used in nowadays long-haul optical networks. Then, some important aspects of the simulation were described, such as the data sequences generation and its temporal and frequency representations. Also, the MC simulation tool to assess the coherent receiver performance was described in detail.

The transmitter model used in this work was described, along with the modulation formats and duty-cycles considered in our study. Additionally, the coherent receiver model used in this work was also presented and its components were extensively described. A particular emphasis has been given to the QF characterization.

The mathematical analysis of the detected signal by the coherent receiver was presented and the statistical description of the ASE noise at the output of the coherent receiver was derived. Finally, the performance evaluations methods used in this work to estimate the BER using the MC simulation were presented: the theoretical BER, the DEC and the EVM.

Chapter 3

M-QAM Receiver Performance in Presence of ASE Noise

3.1 Introduction

This chapter starts with the description of the optical filters (OFs) and the electrical filters (EFs) used in this work, in sections 3.2 and 3.3.

In section 3.4, the validation of the coherent receiver simulation will be performed, by analyzing the DEC and EVM estimations for the M-QAM receiver performance in the presence of ASE noise, using ideal filtering. Additionally, the EVM accuracy for the BER estimations will be evaluated by comparison with the BER predictions obtained using the DEC method.

In section 3.5, the optimization of the -3 dB bandwidth of non-ideal optical and electrical filters will be performed, in order to identify the best OF/EF combination that minimizes the BER for a QPSK coherent receiver. This optimization will define the OF and the EF used in the subsequent chapter of this dissertation.

Finally, in section 3.6, the optimization of the OF/EF pair will be performed for a 16-QAM coherent receiver.

3.2 Optical Filtering

The optical filtering is an essential process in an optical transmission system due to its applications: filtering noise produced by the OAs [29] and multiplexing/demultiplexing wavelengths in WDM systems. The OFs are characterized by their impulse response and transfer function for a specific -3 dB bandwidth B_o, which defines the passband bandwidth and corresponds to the normalized amplitude of $1/\sqrt{2}$ [40].

In the following, the ideal and the n-order Super-Gaussian OFs are described.

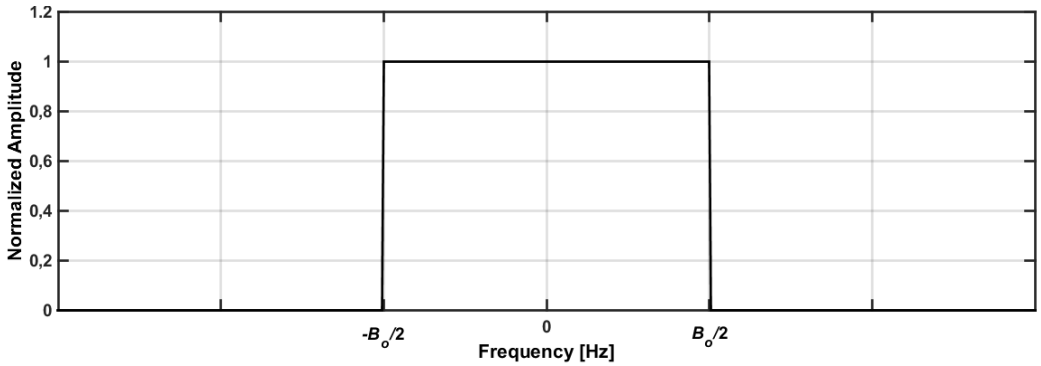

Figure 3.1: Transfer function of the ideal filter.

3.2.1 Ideal Filter

This ideal filter has a rectangular shape in the frequency domain, as represented in Figure 3.1. Hence it rejects all the frequency components outside the passband bandwidth and passes all the frequency components inside its passband bandwidth B_o. The impulse response of the ideal optical filter, in its lowpass equivalent definition, is given by

$$h(t) = B_o \operatorname{sinc}(B_o t) \tag{3.1}$$

In the frequency domain, its amplitude response is defined by

$$H(f) = \mathscr{F}\{h(t)\} = \operatorname{rect}\left(\frac{f}{B_o}\right) \tag{3.2}$$

where $\mathscr{F}\{\}$ is the Fourier Transform function.

Remark that, since the OF is a passband filter, its bandwidth limits, in its passband representation, are $[\nu_0 - B_o/2, \nu_0 + B_o/2]$.

3.2.2 Super-Gaussian Filter

The Super-Gaussian filter can be used as an optical or as an electrical filter. The n-order Super-Gaussian filter impulse response is defined by [6]

$$h(t) = \sqrt{\frac{2\pi}{\ln 2}} \frac{B_o}{2} \exp\left[\frac{2\pi^2}{\ln 2}\left(\frac{B_o}{2}t\right)^{2n}\right] \tag{3.3}$$

The respective transfer function is given by

$$H(f) = \exp\left[-\left(\frac{f \ln 2}{2B_o}\right)^{2n}\right] \tag{3.4}$$

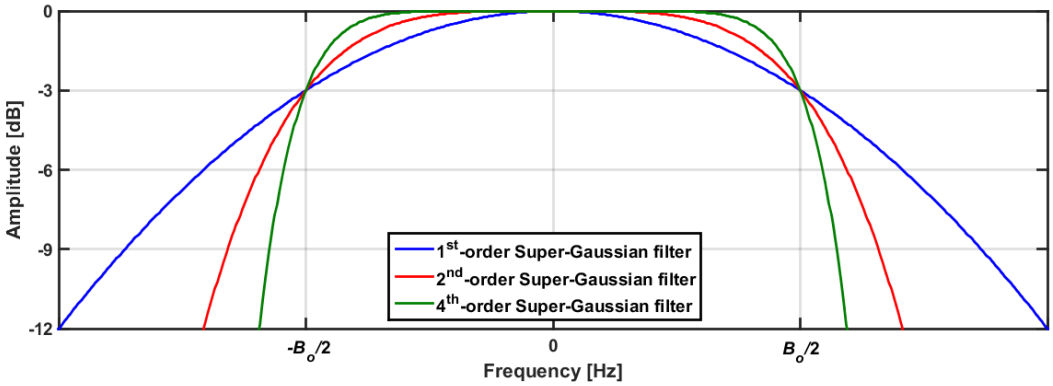

Figure 3.2: Transfer function of n-order Super-Gaussian filter.

which is depicted in Figure 3.2, for several orders. As the order of the filter is increased, a sharper amplitude cut-off and a flatter passband are observed, and theoretically, when $n \to \infty$, the shape of the optical filter tends to a rectangular shape. The 1^{st}-order Super-Gaussian is usually called Gaussian filter, and the 4^{th}-order Super-Gaussian filter can be found in several works as a pulse carver [34] and [35], or as a tunable-OF [35]. Therefore, as these are the most common models, the Super-Gaussian with $n = 1$ and 4 will be the OFs studied in this dissertation. In this work, the Gaussian filter will be also used as an EF. In this case, in Equation (3.3), the optical filter bandwidth, B_o, is substituted by $B_e/2$, where B_e is the electrical filter -3 dB bandwidth.

3.3 Electrical Filtering

As seen in section 2.6, after square-law detection, the LO-ASE beating noise is present and therefore the electrical filtering is needed to reduce the noise power and the ISI in the received signal, which can be introduced by narrow optical filtering. The EF is a low-pass filter with its -3 dB bandwidth defined as B_e.

3.3.1 Integrator-and-Dump Filter

The integrator filter is the ideal matched filter for the rectangular pulses detection [41]. At each incoming pulse, the filter integrates the pulse energy until the end of the impulse duration, then resets, or dumps, to zero [26], which gave origin to its name, integrator-and-dump.

For a rectangular pulse matched filter, the EF -3 dB bandwidth of the integrator-and-dump must be equal to the incoming signal bandwidth, $B_e = 1/T_s$.

The impulse response of the integrator filter is given

$$h(t) = \text{rect}\left(\frac{t}{T_s}\right) \tag{3.5}$$

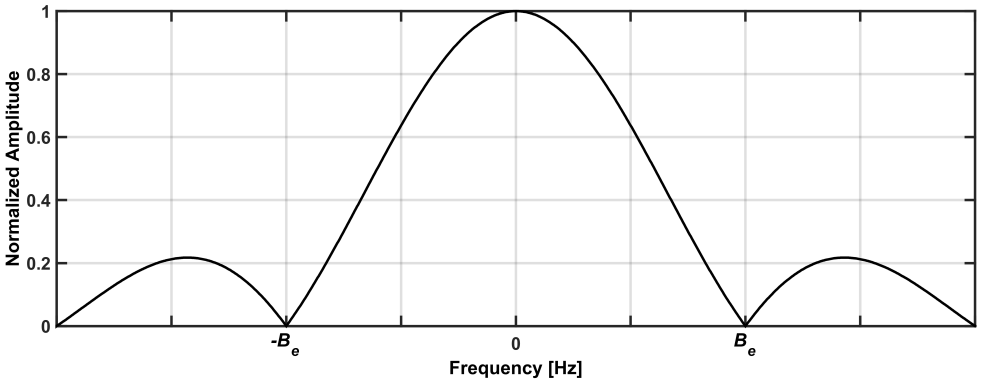

Figure 3.3: Transfer function of the integrator-and-dump filter.

and its respective transfer function is

$$H(f) = T_s \,\mathrm{sinc}(fT_s) \tag{3.6}$$

which is depicted in Figure 3.3.

3.3.2 Bessel Filter

This filter is characterized by having a delay response maximally flat [24], which results in a minimal overshoot in the filtering of signals in the passband frequency. The Bessel filter transfer function is defined by [6]

$$H(s) = \frac{d_0}{B_n(s)} \tag{3.7}$$

where $s = j2\pi f$ and d_0 is a normalizing constant given by

$$d_k = \frac{(2n-k)k!}{2^{n-k}k!(n-k)!} \tag{3.8}$$

by taking $k = 0$. Finally, $B_n(s)$ is the nth-order Bessel polynomial defined by

$$B_n(s) = \sum_{k=0}^{n} d_k(s)^k \tag{3.9}$$

which can be recursively calculated using

$$B_n(s) = (2n-1)B_{n-1}(s) + s^2 B_{n-2} \tag{3.10}$$

In terms of amplitude response, the low order Bessel filters have a slow pass-band cutoff, as it can be seen in Figure 3.4. Therefore, it is necessary to implement higher orders filters to achieve a higher selectivity. As the filter order increases, the Bessel filter tends to have a similar shape as the 1^{st}-order Super-Gaussian filter [42].

Figure 3.5 depicts the group delay for the $\{1,3,5\}$-order Bessel filter. Increasing the order of the EF provides a better group delay response. Analyzing the group delay response for the 5^{th}-order Bessel filter, which is the one that is used in this work, it is clear that its group delay is flat inside the pass-band region. Therefore, this type of EF is commonly used in optical networks due to its low delay distortion [40].

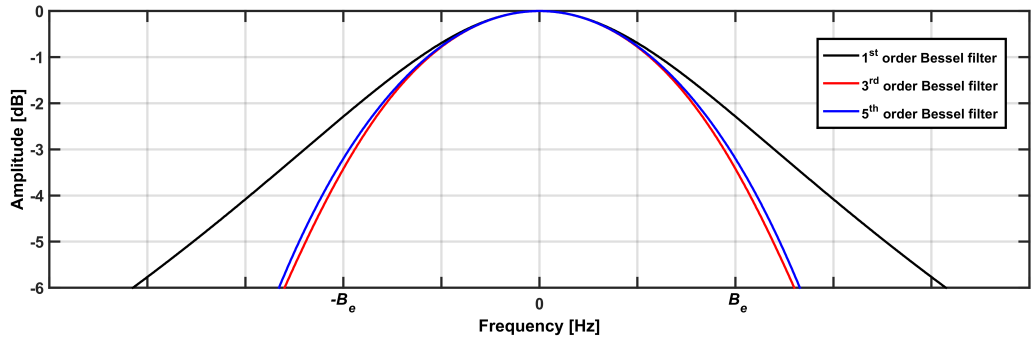

Figure 3.4: Transfer function of the n-order Bessel filter.

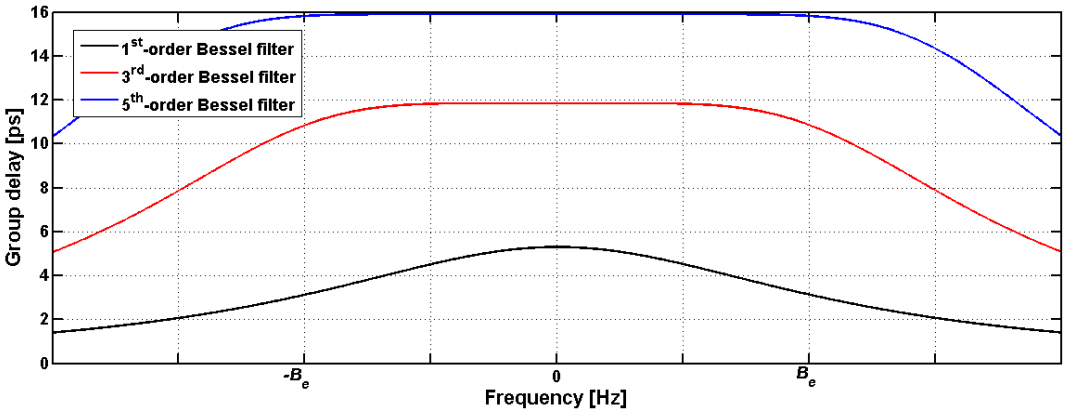

Figure 3.5: Group delay of the n-order Bessel filter.

3.4 System Validation

In this section, we will describe the validation of the coherent receiver simulator through comparison of the BER obtained using the DEC and from the EVM with the BER theoretical curves for several M-QAM modulation formats.

The theoretical BER presented in section 2.7.1 is obtained for a rectangular optical filter, as described in

Equation (3.2), with a very large bandwidth and with the integrator-and-bump filter defined in Equation (3.6). In our study, the normalized -3 dB bandwidth of the ideal OF varies for the values of $B_o/R_s = \{1,2,5,10,100\}$ and the signal pulse shape considered throughout this section is the rectangular NRZ.

Additionally, the simulation time using the EVM method will be compared with the simulation time obtained using the DEC method.

3.4.1 DEC Method

For the system performance validation, we choose as a stopping criteria 1000 counted errors for the DEC assessments, in order to obtain a BER estimation as most accurate as possible, without demanding a significant simulation time.

3.4.1.1 QPSK Modulation Format

The DEC BER estimations as a function of the OSNR for the QPSK coherent receiver performance are depicted in Figure 3.6. For the bandwidths of $B_o/Rs \geq 10$, the simulations results agree with the theoretical ones. So, our simulator can be considered validated for this receiver configuration. However, for lower OF bandwidths ($B_o/R_s = 1$ and $B_o/R_s = 2$), a notorious discrepancy can be observed between the theoretical BER and the simulated BER. Using an ideal OF with lower -3 dB bandwidth, the performance degradation is due to the existence of ISI, which is not taken into account by the theoretical BER formula, given in Equation (2.39). Analyzing the noiseless eye pattern of the received signal after the post-detection filter for $B_o/R_s = 1$, shown in Figure 3.7(a), the ISI of the QPSK NRZ signal is clearly visible. The ISI effect is so dominant that the full aperture of the eye is not reached. For larger OF -3 dB bandwidths, for example with $B_o/R_s = 100$, since the

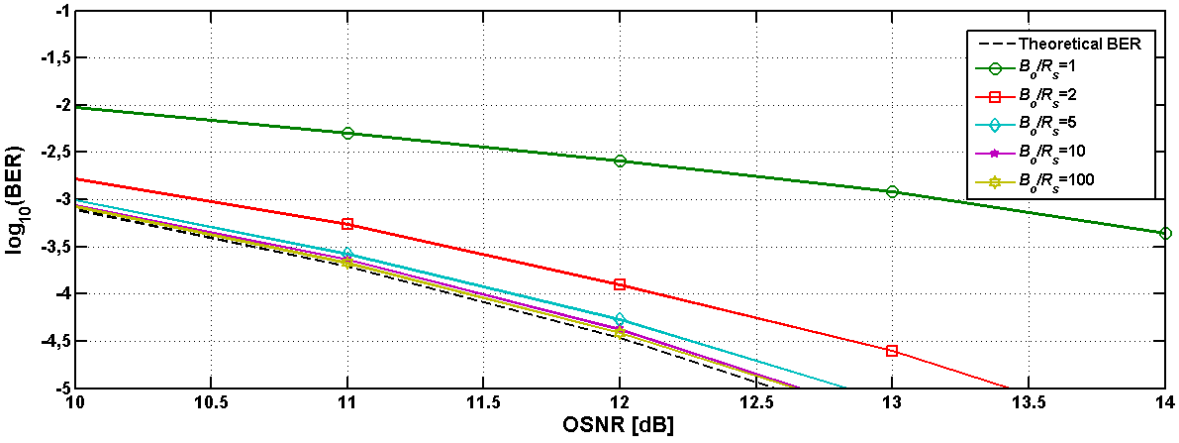

Figure 3.6: BER as a function of the required OSNR, using an ideal OF and integrator-and-dump EF, for the QPSK modulation format.

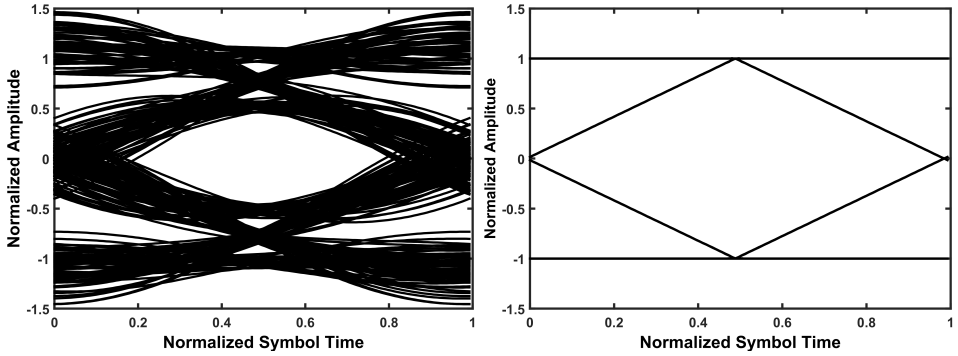

(a) $B_o/R_s = 1$ **(b)** $B_o/R_s = 100$

Figure 3.7: Eye diagrams of a QPSK signal with ideal filtering for (a) $B_o/R_s = 1$ and (b) $B_o/R_s = 100$ without ASE noise.

ideal OF plus the integrator-and-dump EF act as a matched filter for the rectangular pulses [26], the eye diagram (ED) is completely open, as we can see in Figure 3.7(b).

Regarding the simulation time of the QPSK receiver performance assessed using the DEC method, we choose to measured the elapsed time of the MC simulation for $B_o/R_s = 100$, since its BER estimation curve overlaps the theoretical one. The BER estimation curve was obtained after 3952 seconds and the BER of 10^{-5} prediction demanded 126976 sample functions.

Figure 3.8 depicts the probability mass function (PMF) of the signal amplitudes for the I and Q components for the QPSK modulation format, where it can be observed that all symbol amplitudes have equal probabilities. As said in section 2.3.1, the QPSK symbols sequence is generated using Galois Fields, which results in a sequence with 256 symbols, having all the transitions for the symbols combination for the QPSK modulation format and consequently, all symbol amplitudes have equal probabilities and the ISI is efficiently characterized.

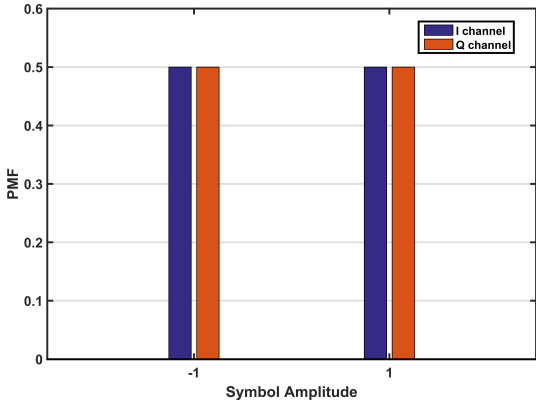

Figure 3.8: PMF of the symbols sequence amplitude for a QPSK signal.

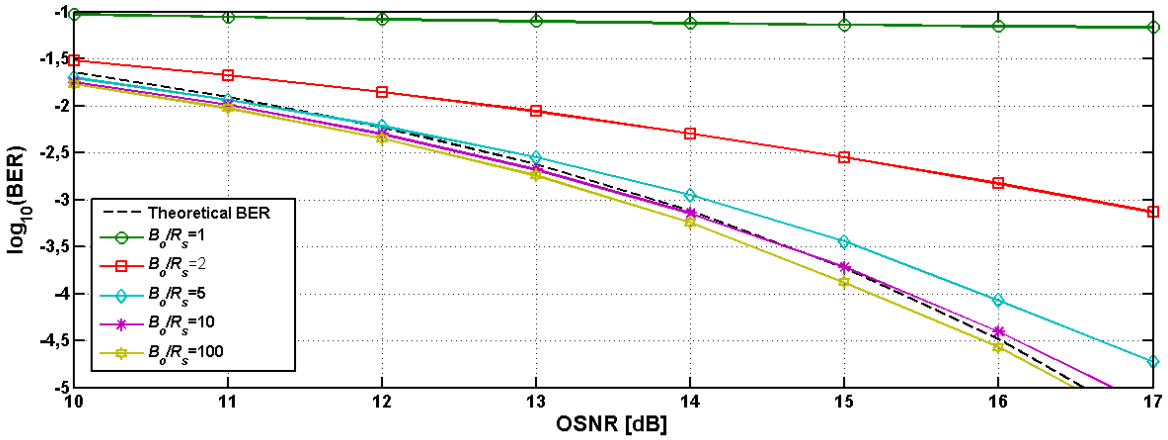

Figure 3.9: BER as a function of the required OSNR, using an ideal OF and an integrator EF, for the 16-QAM modulation format.

3.4.1.2 16-QAM modulation format

The BER as a function of the OSNR for the 16-QAM modulation format using the DEC method is depicted in Figure 3.9. Here, the simulated BERs for larger normalized bandwidths ($B_o/Rs = \{10, 100\}$) practically overlap the theoretical ones. The impact of the ISI caused by lower filter bandwidths results in a stronger performance degradation comparing to the performance of the QPSK receiver. The ISI is enhanced by the more abrupt symbol transitions in a 16-QAM signal, comparing to the QPSK signal. As an example, for $B_o/R_s = 1$, the BER is practically constant with the OSNR variation. Moreover, comparing with the same bandwidth in Figure 3.6, the BER is approximately ten times higher than the QPSK receiver performance for the OSNR of 10 dB. Even though, the simulator can be considered validated for the 16-QAM modulation format.

The noiseless EDs for $B_o/R_s = 2$ and $B_o/R_s = 100$ are depicted in Figures 3.10(a) and 3.10(b), respectively.

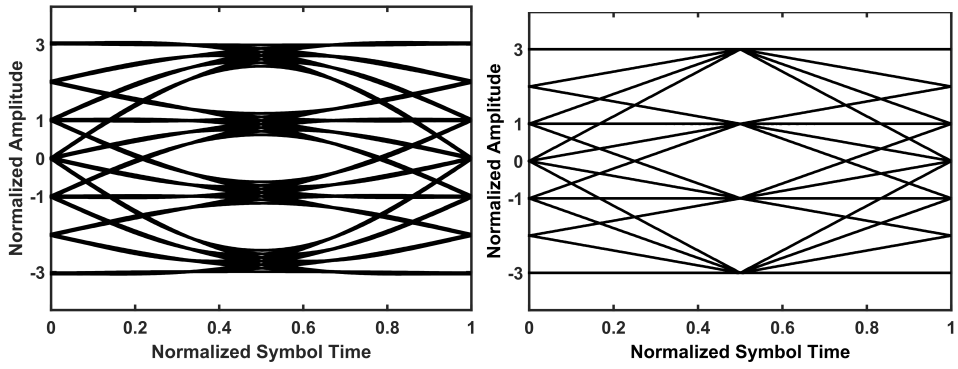

(a) $B_o/R_s = 2$ **(b)** $B_o/R_s = 100$

Figure 3.10: Eye diagrams of a 16-QAM signal with ideal filtering for (a) $B_o/R_s = 2$ and (b) $B_o/R_s = 100$ without ASE noise.

We choose to represent the eye diagram corresponding to $B_o/R_s = 2$, instead of $B_o/R_s = 1$, because the latter bandwidth leads to a closed eye diagram, due to the considerable ISI at the sampling time instant.

The PMF of the I and Q components of the 16-QAM modulation format with 512 symbols is depicted in Figure 3.11, where the occurrence of all the possible signal amplitudes have equal probabilities, as in the case of the QPSK signal.

The performance of the 16-QAM receiver having the normalized OF -3 dB bandwidth of $100R_s$ was assessed in 1677 seconds and the BER of 10^{-5} was estimated after 60928 sample functions. Therefore, this simulation took approximately half of the time needed for the QPSK receiver performance assessment and half of the sample function required for the BER of 10^{-5} estimation. This is attributed to the 16-QAM symbols sequence length, which is the double of the QPSK symbols sequence length. By increasing the sequence length, the stopping criteria of the MC simulation is achieved faster, since for a given OSNR, the number of errors per sample functions increases, and consequently, the MC simulator requires less sample functions to achieve a stabilized BER for the 16-QAM modulation format.

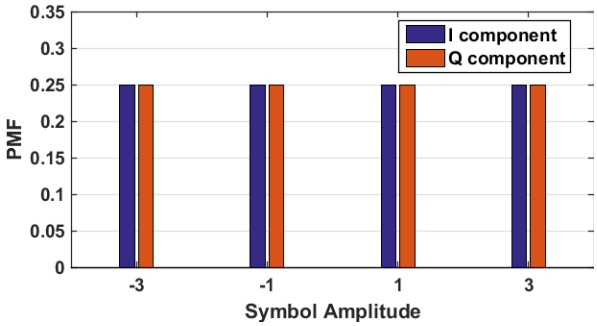

Figure 3.11: PMF of the symbols sequence amplitude for a 16-QAM signal.

3.4.1.3 64-QAM Modulation Format.

For the 64-QAM modulation format, the symbols generation was performed using the Matlab function *rand*. So, it is relevant to investigate how many random symbols are required to reach reliable performance results to account accurately the ISI in the simulation. Figure 3.12 shows the BER as a function of the OSNR for different symbols sequence lengths for the 64-QAM modulation format having $B_o/R_s = 10$. This bandwidth was chosen because it introduces some ISI on the 64-QAM signal at the decision circuit input, without exaggeratedly degrading the receiver performance. Figure 3.12 shows that the BERs as a function of the OSNR by using different symbols sequence lengths are practically stabilized for sequences longer than 2^5 symbols. As seen in previous sub-sections, we conclude that by using longer sequences, the stopping criteria is achieved more rapidly, and hence less sample functions are needed to observe more errors at the decision circuit input.

In order to guarantee that all symbols transitions are considered in the 64-QAM symbols sequences and ISI

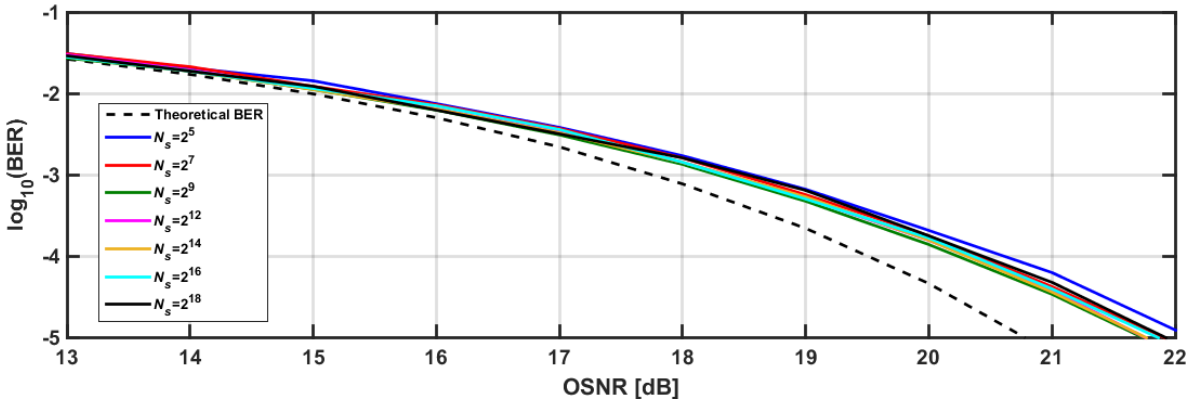

Figure 3.12: BER as a function of the OSNR, using an ideal OF with $B_o/R_s = 10$ and an integrator EF, for different 64-QAM symbols sequence lengths.

is taken in account accurately in the simulation, we choose to generate a random sequence with 2^{18} symbols. This sequence length leads practically to the same simulation time as the ones required for shorter symbols sequences, as shown in Table 3.1, which presents the required simulation time to estimate the BER for all OSNRs shown in Figure 3.12.

Figure 3.13 depicts the PMF of a 64-QAM symbols sequence having 2^{18} symbols. As it can been seen in the PMF, the equiprobability of all possible 64-QAM signal amplitudes is nearly achieved.

Figure 3.14 shows the BER as a function of the OSNR for the 64-QAM modulation format considering different OF -3 dB bandwidths. In this case, the ISI has a stronger impact than the one observed in Figure 3.9, since for $B_o/R_s = 1$ and $B_o/R_s = 2$, due to the ISI, the BER is very high and its reduction is almost insignificant with the OSNR increase. In opposition to what happened in the validation of QPSK and 16-QAM modulation formats, shown in Figure 3.6 and 3.9, respectively, the receiver performance for the bandwidths of $B_o/R_s = 10$ and $B_o/R_s = 100$, for lower BERs, does not overlap the theoretical BER curve. This is attributed to the ISI enhancement caused by the more abrupt amplitude transitions of the 64-QAM signal. However, the receiver performance for $B_o/R_s = 100$ is sufficiently close to the theoretical BER estimation and the 64-QAM coherent receiver simulation can be considered validated.

Table 3.1: Simulation times of the sequences length optimization for the generation of 64-QAM random symbols sequences.

Number of symbols	Simulation time [s]
2^5	1418
2^7	1544
2^9	1669
2^{12}	947
2^{14}	1837
2^{16}	1758
2^{18}	1676

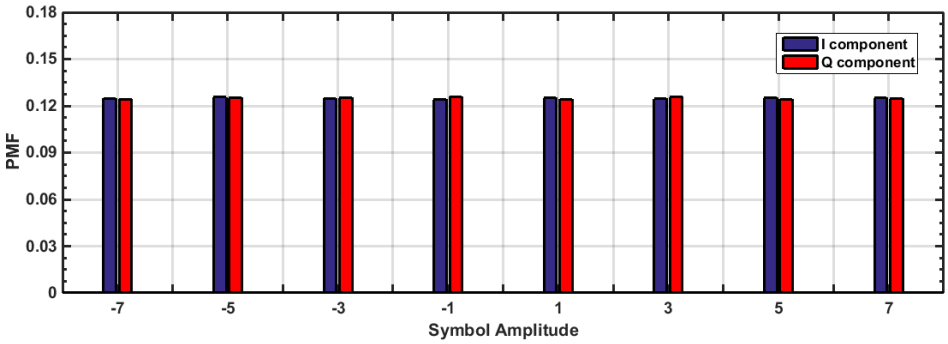

Figure 3.13: PMF of the symbols sequence amplitude for a 16-QAM signal with 2^{18} symbols.

Figure 3.15 represents the EDs of the received signal to illustrate the ISI impact on the 64-QAM receiver with $B_o/R_s = 2$ (Figure 3.15(a)) and with $B_o/R_s = 100$ (Figure 3.15(b)). From the ED obtained for $B_o/R_s = 2$, it is clear that the ISI leads to a very closed eye pattern, due to the abrupt symbol transitions observed for the 64-QAM modulation format. The EDs obtained for $B_o/R_s = 100$ are completely open.

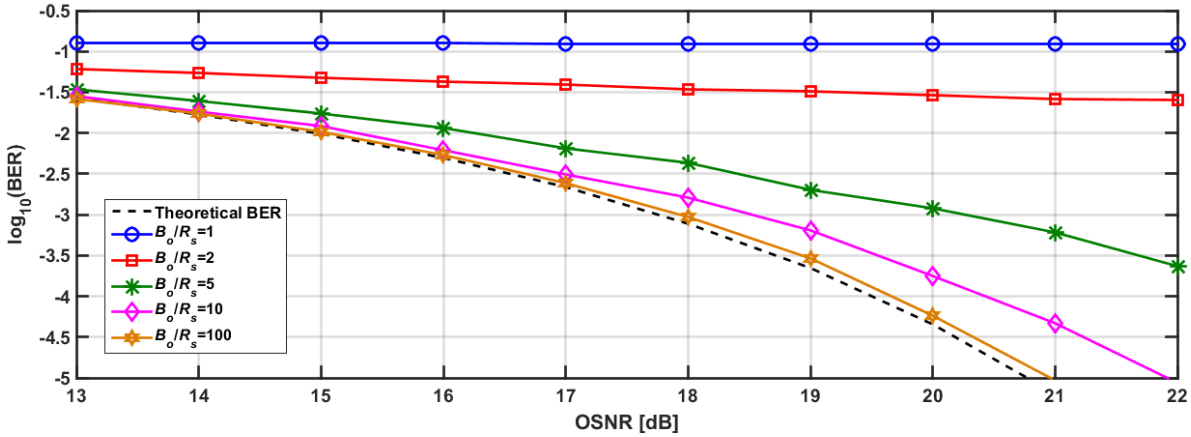

Figure 3.14: BER as a function of the required OSNR, using an ideal OF and an integrator-and-dump EF, for the 64-QAM modulation format.

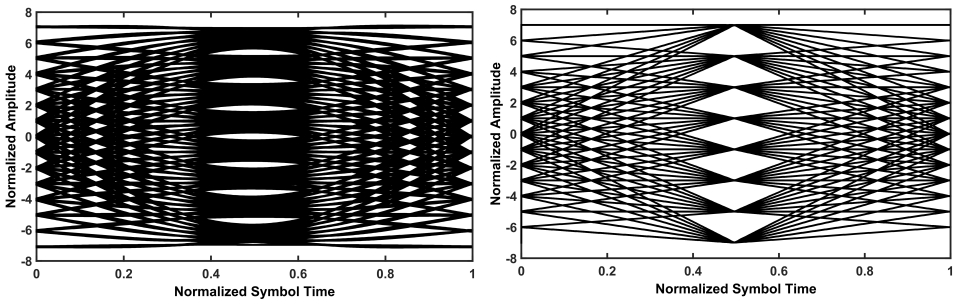

(a) $B_o/R_s = 2$ **(b)** $B_o/R_s = 100$

Figure 3.15: Eye diagrams of a 64-QAM signal with ideal filtering for (a) $B_o/R_s = 2$ and (b) $B_o/R_s = 100$ without ASE noise.

3.4.2 EVM Method

With the EVM method, two questions arise: first, how accurate the EVM can be in comparison with the DEC, and second, how many sample functions are sufficient to reach a stabilized BER estimation. Therefore, in this section, the system performance will be evaluated using the EVM method and the cases where each method (DEC and EVM) is recommended for a less computational time with sufficient BER accuracy will be identified.

To assess the EVM accuracy, we choose the ideal filter configuration with $B_o/R_s = 100$. Figure 3.16 shows the BER as a function of the number of sample functions, for the DEC and EVM methods. Only 250 sample functions of ASE noise have been simulated. To a better distinction of the results of Figure 3.16, the EVM estimations are indicated by a dash-dot blue line, while the DEC estimations are highlighted with different line colors per $\log_{10}$(BER) value.

In our studies, we define the maximum and minimum probability values in which a BER measurement is considered to be accurate as $\log_{10}(BER) \pm 0.1$. The OSNRs that lead to the BERs of 10^{-2}, 10^{-3}, 10^{-4} and 10^{-5} are 7.5 dB, 9.9 dB, 11.5 dB and 12.6 dB, respectively. Those OSNRs were obtained from the theoretical formula obtained for the QPSK modulation format using Equation (2.39).

From Figure 3.16, we see that the DEC estimations become more unstable for lower BERs. Therefore, the DEC requires much more sample functions than the EVM, in order to obtain a stabilized BER estimate. In contrast, independently of the BER estimation value, the EVM method needs fewer sample functions for a stabilized BER estimation which allows using the EVM method to estimate very low BERs [36]. Furthermore, the BER estimations using the EVM are within the accuracy limits. Comparing the BER estimates for 10^{-5}, the EVM estimation becomes stabilized, inside the accuracy limits, with approximately 37 sample functions, while the DEC method requires more than 250 sample functions for an accurate estimation. In this work, the EVM

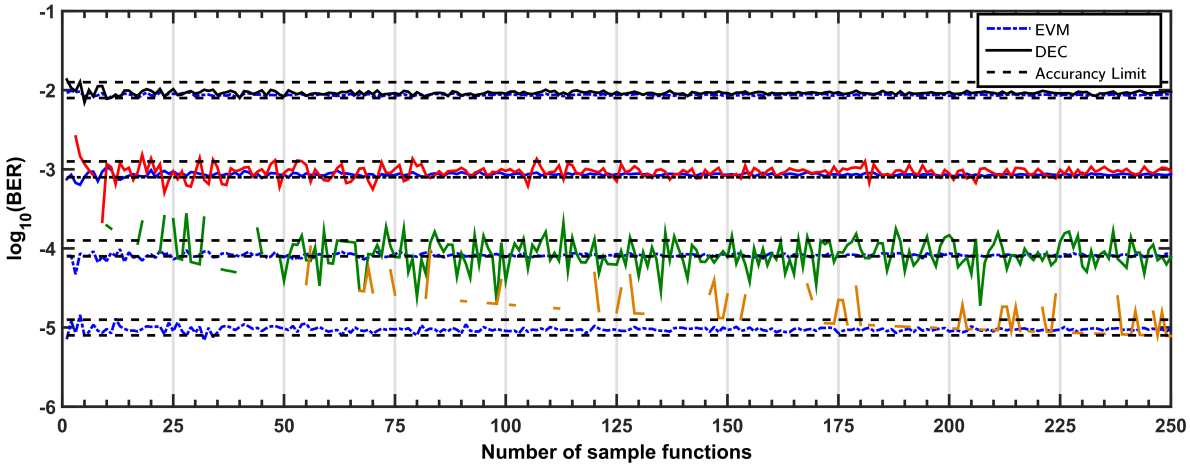

Figure 3.16: BER as a function of the generated N_{MC} with ideal filtering, obtained using the EVM method and considering $N_{MC} = [1, 250]$.

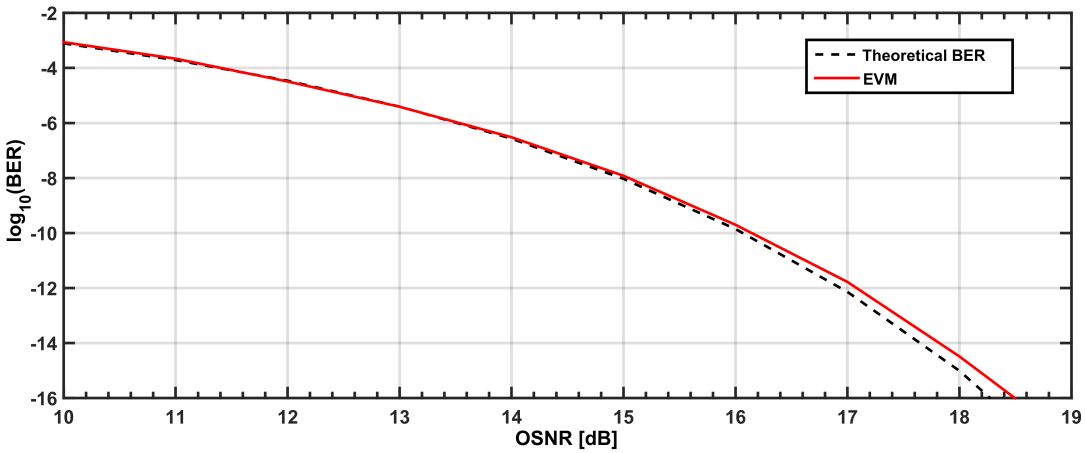

Figure 3.17: BER as a function of the OSNR by using the EVM method for the QPSK modulation format and considering lower BERs.

estimations is obtained after generating 64 sample functions.

Then, the EVM accuracy was studied for very low BERs. Those results are shown in Figure 3.17, for ideal filtering with $B_o/R_s = 100$ and with 64 generated sample functions. The simulation only took 166 seconds to finish. The EVM curve practically overlaps the theoretical BER curve, even for BER$= 10^{-15}$. For this BER, the theoretical required OSNR is 18 dB against the 18.2 dB estimated using the EVM method, which is a negligible difference. Therefore, using ideal filtering, the EVM method has proven to be a good semi-analytical tool for assessing the receiver performance for very low BERs. The EVM has also the advantage of demanding very low computational time in comparison with the DEC method.

In the following, we evaluate the coherent receiver performance using the EVM, for the ideal receiver with $B_o/R_s = \{1,2,5,10,100\}$ by comparing with the BER theoretical curves. The EVM BER estimations for the QPSK receiver performance as a function of the OSNR are depicted in Figure 3.18. As observed for the DEC estimations, Figure 3.18 shows that the EVM BER estimates overlap the theoretical BERs for $B_o/R_s \geq 5$. Only for lower optical bandwidths, $B_o/R_s = 1$ and $B_o/R_s = 2$, a very high discrepancy between the BER assessments and the theoretical BER is noticed. The optical bandwidth $B_o/R_s = 1$ leads to a slow decrease of the BER as the OSNR increases, due to the ISI, and with $B_o/R_s = 2$, the required OSNR for a BER of 10^{-5} is almost 1 dB higher than the OSNR theoretically estimated.

The EVM BER estimates for the 16-QAM modulation format are depicted in Figure 3.19. Also, for larger bandwidths ($B_o/R_s = 10$ and $B_o/R_s = 100$), the EVM method provides the same performance results as the ones obtained theoretically. However, for $B_o/R_s \leq 5$, when the ISI has a more deteriorating effect on the receiver performance, a larger difference between the 16-QAM performance obtained using the EVM and the theoretical curves is found, comparing to the one observed in Figure 3.18. This effect is mainly due to the higher symbols amplitude transitions in the 16-QAM signal comparing to the QPSK signal.

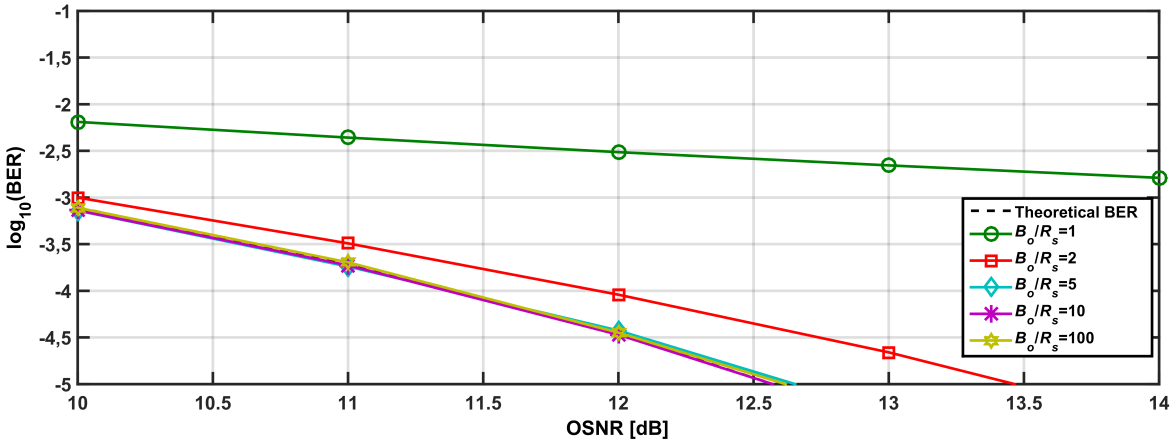

Figure 3.18: BER as a function of the OSNR, for a QPSK ssignal with 50 Gbps using an ideal OF and an integrator EF, estimated using the EVM, Equation (2.42) and the theoretical formula given by Equation (2.39).

The assessment results of the 64-QAM coherent receiver performance obtained from the EVM method are depicted in Figure 3.20. The 64-QAM receiver performance estimation using the EVM method is practically similar to the DEC assessment for the 64-QAM receiver performance in all the considered OF -3 bandwidths, depicted in Figure 3.14. However, the simulation time for the EVM method has increased significantly comparing with the simulation time for the QPSK and the 16-QAM receiver performance assessments, which were only 11 and 22 seconds, respectively. In this case, the simulation took approximately 1850 seconds for each B_o/R_s performance assessment. The increase of the simulation time is attributed to the increased length of the symbols sequence. Having longer symbols sequence increases significantly the computation of the EVM using Equation (2.41). Therefore, the EVM becomes an unattractive method for the performance assessment, since it leads to practically the same computation time as the DEC method with a sequence length of 2^{18}.

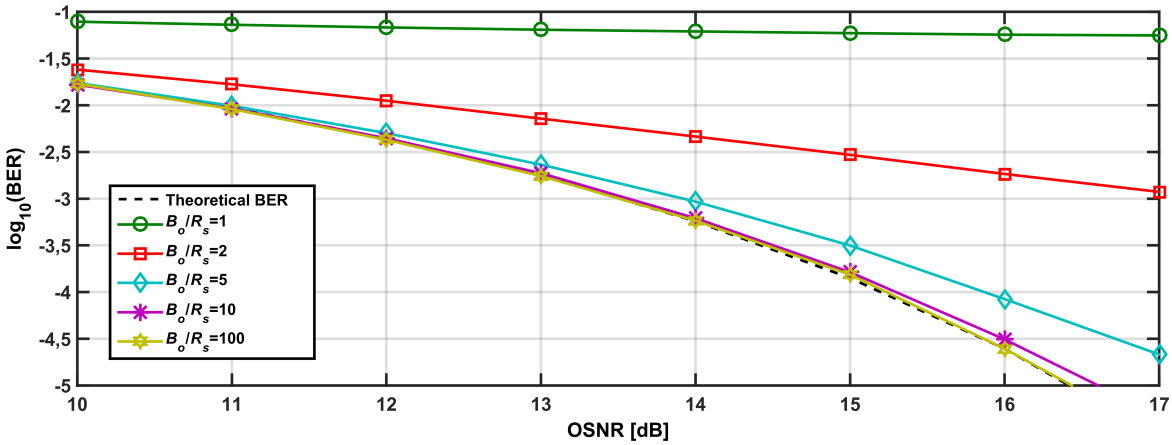

Figure 3.19: BER as a function of the OSNR, for a 16-QAM signal with 50 Gbps using an ideal OF and an integrator EF, estimated using the EVM, Equation (2.42) and the theoretical formula given by Equation (2.39).

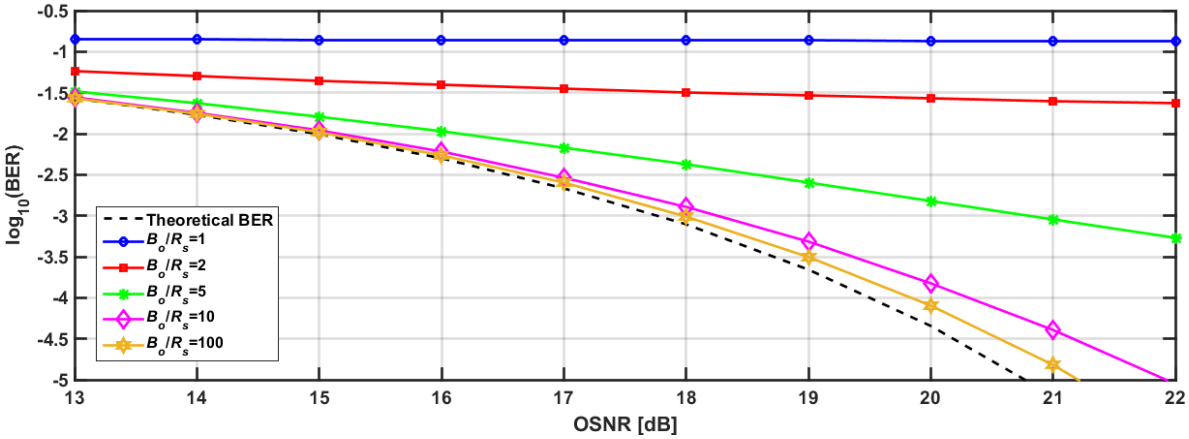

Figure 3.20: BER as a function of the OSNR, for a 64-QAM signal with 50 Gbps using an ideal OF and an integrator EF, estimated using the EVM, Equation (2.42) and the theoretical formula given by Equation (2.39).

3.5 Filters Optimization for the QPSK Modulation Format

In this section, the performance of the QPSK coherent receiver will be assessed using different combinations of optical and electrical filters, in order to identify the filters bandwidths that minimize the BER of the optical coherent detection receiver, for all the four duty-cycles, considering the BER of 10^{-3} as a target to achieve. This BER is typically chosen for performance optimization, since it corresponds to the forward error correction (FEC) with 7% overhead threshold [35], [43]. Additionally, this target BER assures a reasonable simulation time for the DEC method, regarding that the optimization required to evaluate all the OF and EF bandwidths with a good accuracy uses 1000 counted errors as the stopping criteria for the DEC estimations. As for the EVM receiver performance assessments, the required number of sample functions for a stabilized BER estimation was evaluated by repeating the test performed in Figure 3.16, but using the different non-ideal OF/EF filters combinations used in this dissertation and having a -3 dB bandwidth of 25 GHz. The results allowed to conclude that 64 sample functions is also sufficient for a stable BER estimation by using non-ideal filtering.

The next sub-sections also describe the optimization of the four pairs of optical and electrical filters covered in this work: the Gaussian OF and the 5^{th}-order Bessel filter (GB); the Gaussian OF and EF (GG); the 4^{th}-order Super-Gaussian OF and 5^{th}-order Bessel EF (4GB) and finally the 4^{th}-order Super-Gaussian OF and the Gaussian as the EF (4GG). The comparison between the accuracy of DEC and EVM methods is also assessed, regarding the prediction for the optimum filters bandwidths and the BER estimations.

In the simulations, filters bandwidths are normalized to the symbol rate and the duty-cycle of the optical signal is 33, 50, 66 or 100%.

In each sub-section, the best optical and electrical filters bandwidths that minimize the BER of the optical coherent detection receiver, for all the four duty-cycles, is chosen by following the next procedure: first, the EF bandwidth is chosen to reach the BER of 10^{-3} on all the considered duty-cycles, and its value is chosen in

order not to be too wide for the NRZ pulse shape and too narrow for the RZ33 pulse shape. Then, considering the chosen EF bandwidth, the best OF bandwidth is the one that leads to the lowest BER for each duty-cycle. At the end of this section, the best filter configuration is elected, considering the DEC results obtained for each filters optimization.

The simulation parameters for this study are presented in Table 3.2.

Table 3.2: Parameters for the QPSK system optimization.

Parameter	**DEC**	**EVM**
Signal modulation format	QPSK (single polarization)	
OSNR	10.5 dB	
R_s	25 Gbaud	
Number of symbols	256	
Number of samples per symbol (N_a)	64	
Target BER	10^{-3}	
Variation of B_o	[0.5, 5.5]R_s	
Variation of B_e	[0.2, 2.4]R_s	
MC stopping criteria	1000 counted errors	64 sample functions

3.5.1 Gaussian Optical Filter and Fifth Order Bessel Electrical Filter

Figure 3.21 shows the BER estimated using the DEC (left-hand side) and the EVM (right-hand side) for the receiver with a QPSK modulation format, having the GB filters pair, for different duty-cycles.

Figure 3.21 shows that both methods agree in the optimum OF and EF -3 dB bandwidths estimations. However, there is a slight difference between the BERs estimated using the DEC and EVM methods. For the optimum filters bandwidths, the $\log_{10}$(BER) predicted using the EVM method is approximately -3.3 for the RZ signals, and -3.2 for the NRZ pulse shape, while the DEC estimates the BER of -3.1 for the RZ pulse shapes and -3 for the NRZ signal. The discrepancy between both methods increases with the reduction of the duty-cycle and the normalized EF -3 dB bandwidth. In Figure 3.21(d), the $\log_{10}$(BER) predicted using the EVM method is approximately -1 for the QPSK RZ33 receiver performance having the EF -3 dB bandwidth of $0.3R_s$ and the OF -3 dB bandwidth of R_s, while the DEC estimates a $\log_{10}$(BER) of -1.5 for the same filters bandwidths. The discrepancy between both methods is attributed to the ISI introduced by narrow filter bandwidths. However, both methods are in conformity concerning the predicted BERs for higher filters bandwidths.

The best filters configuration that minimizes the BER of the optical coherent receiver, for all the four duty-cycles, can be extracted from Figure 3.21. In each figure, a vertical line was added to serve as a guideline to identify the optimum OF -3 dB bandwidth for each pulse, using the chosen EF bandwidth. Remark that the

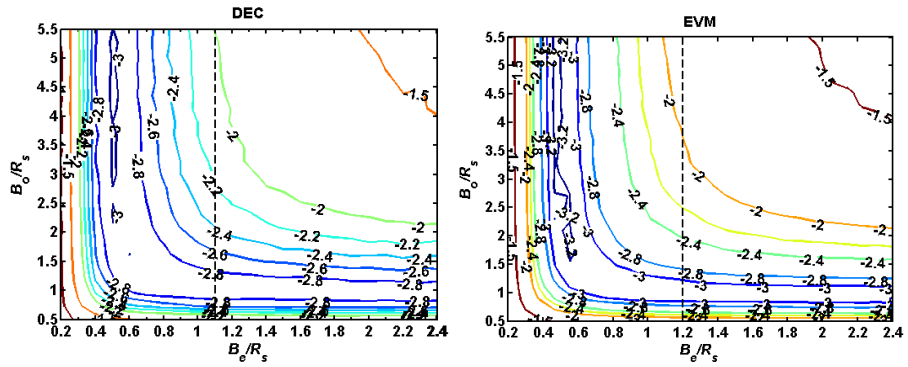

(a) QPSK NRZ

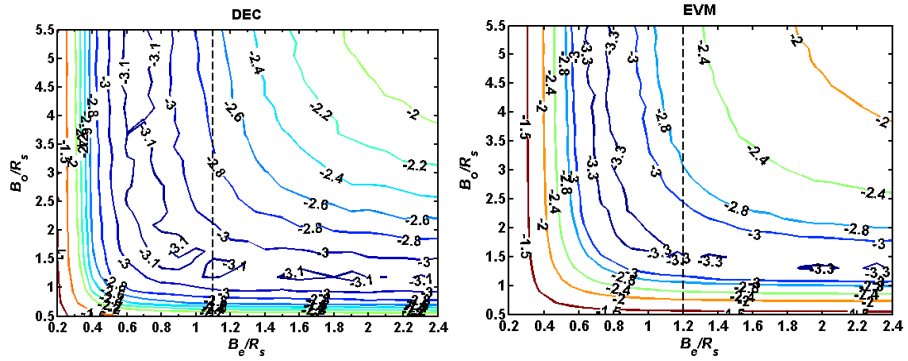

(b) QPSK RZ66

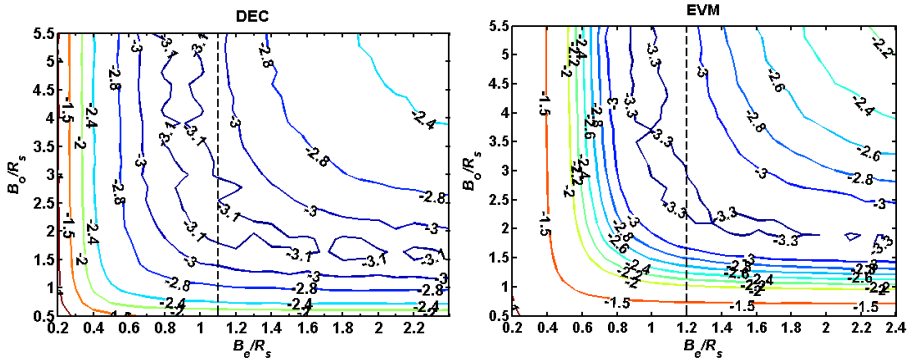

(c) QPSK RZ50

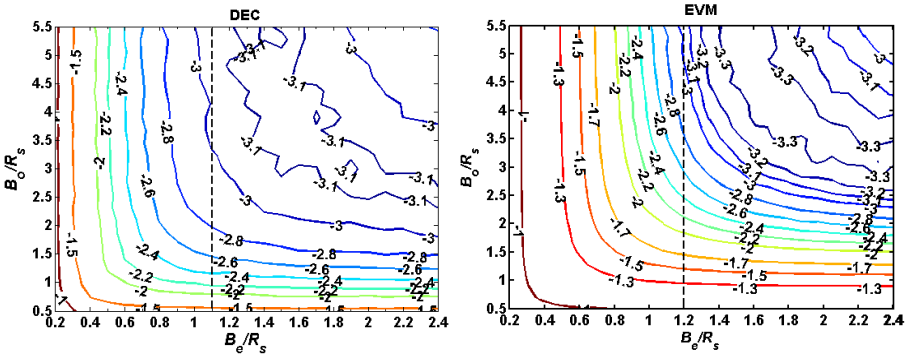

(d) QPSK RZ33

Figure 3.21: Contour plots of the DEC (left side) and the EVM (right side) $\log_{10}(BER)$ estimates as a function of the normalized -3 dB bandwidths of the Gaussian OF and 5^{th}-order Bessel EF, for the QPSK (a) NRZ, (b) RZ66, (c) RZ50 and (d) RZ33 receiver.

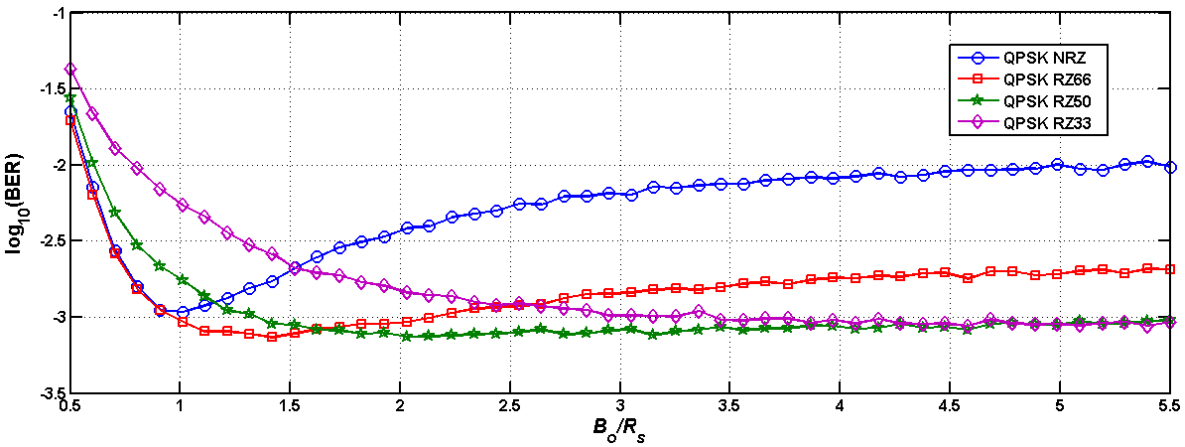

Figure 3.22: BER as a function of B_o/R_s for the Gaussian OF bandwidth and the NRZ, RZ66, RZ50 and RZ33 pulse shapes, with OSNR=10.5 dB and having the 5^{th}-order Bessel EF with a bandwidth of $1.1R_s$.

EF -3 dB bandwidth is chosen to reach the BER of 10^{-3} on all the considered duty-cycles and it results from a compromise between the ASE noise and filter-induced ISI. Figure 3.22 depicts the BER as a function of the normalized OF -3 dB bandwidth, for the OSNR of 10.5 dB and the chosen EF -3 dB bandwidth of $1.1R_s$. Table 3.3 shows the optimum OF -3 dB bandwidth per signal duty-cycle, normalized to R_s for the QPSK receiver having the GB filter configuration.

Figure 3.23 shows the noiseless EDs of the four signals pulse shapes at the input of the decision circuit, obtained using the GB filters pair with the EF -3 dB bandwidth of $1.1R_s$ and the optimum OF -3 dB bandwidths. The eye-closure penalty (ECP) is calculated from the EDs using Equation (5.4.26) of [28]. The ECPs are 1.6, 1.7, 1.7 and 2.7 dB for the NRZ, RZ66, RZ50 and RZ33 signals, respectively. As seen in the ED for the QPSK NRZ (Figure 3.23(a)), the signal filtering leads to ISI at the receiver sampling time instant. However, the eye is sufficiently open to provide a good noise margin. For the remaining signals, the ISI does not occur but as the pulse width decreases, the maximum amplitude of the received signal is not reached, leading to a closure of the ED for each duty-cycle.

Table 3.3: Summary of the -3 dB bandwidths for the GB filters configuration, normalized to R_s, per pulse shape, for the QPSK receiver, considering the DEC and EVM results.

Modulation Format	**Pulse Shape**	**DEC**		**EVM**	
		$B_{e,opt}$	$B_{o,opt}$	$B_{e,opt}$	$B_{o,opt}$
QPSK at 50 Gbps (per polarization)	**NRZ**	1.1	1	1.2	1
	RZ66		1.2		1.5
	RZ50		2		2.3
	RZ33		3.5		3.5

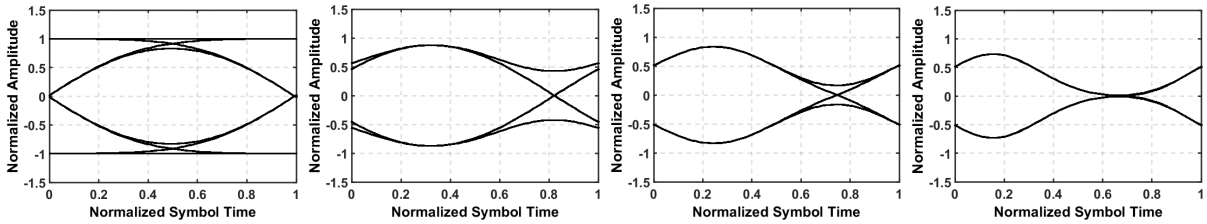

(a) NRZ **(b)** RZ66 **(c)** RZ50 **(d)** RZ33

Figure 3.23: Received eye diagrams of the QPSK modulation format with (a) NRZ, (b) RZ66, (c) RZ50 and (d) RZ33 pulse shapes, after Gaussian OF and 5^{th}-order Bessel EF having the respective optimum -3 dB bandwidths.

3.5.2 Gaussian Optical Filter and Gaussian Electrical Filter

In this section, the optimization of the QPSK coherent receiver performance was performed for the Gaussian OF and Gaussian EF. The optimization results are presented in Figure 3.24 for the NRZ, RZ66, RZ50 and RZ33 signals. The DEC estimates are depicted at the left-hand side and the EVM estimations are shown at the right-hand side.

From Figure 3.24, regarding the optimum Gaussian OF and EF -3 dB bandwidths for the QPSK coherent receiver, both methods are in agreement for all the duty-cycles considered. However, as in the previous filter configuration, the lowest $\log_{10}$(BER) predicted by the EVM, for the NRZ signal, is -3.1 while for the DEC method, the lowest $\log_{10}$(BER) is -2.8. For the RZ signals, the minimum $\log_{10}$(BER) predicted by the EVM is -3.3, while the DEC estimates -3.1. It is also observed that the discrepancy between the BER estimations from both methods for lower EF -3 dB bandwidths, where the ISI is dominant, becomes higher as the signal duty-cycle decreases. Figure 3.24(d) shows that the DEC estimates a $\log_{10}$(BER) of -1.5 for the EF -3 dB bandwidth of $0.3R_s$ and OF -3 dB bandwidth of R_s for the QPSK RZ33 coherent receiver, while, for the same filters -3 dB bandwidths, the EVM predicts a $\log_{10}$(BER) of -1. Finally, for higher OF and EF bandwidths, the BER estimates from both methods are in a better agreement.

The filters bandwidths that minimize the BER for the QPSK coherent receiver having the GG filters configuration are presented in Table 3.4. The Gaussian EF -3 dB bandwidth predicted by the DEC method is slightly narrow than the one found in the GB scenario. Regarding the OF -3 dB bandwidths, they are similar to the GB filters pair.

The noiseless EDs of each filtered pulse shape are similar to ones obtained for the GB configuration. The ECPs are 1.7, 1.6, 1.7 and 2.8 dB for the NRZ, RZ66, RZ50 and RZ33 signals, respectively. However, from Figure 3.24(a), we conclude that this filters configuration leads to a worse receiver performance than the filter configuration using the 5^{th}-order Bessel EF and the Gaussian OF, since the lowest $\log_{10}$(BER) is almost -2.9, while the optimum bandwidths for the GB configuration leads to a $\log_{10}$(BER) of -3 on the QPSK NRZ coherent receiver performance.

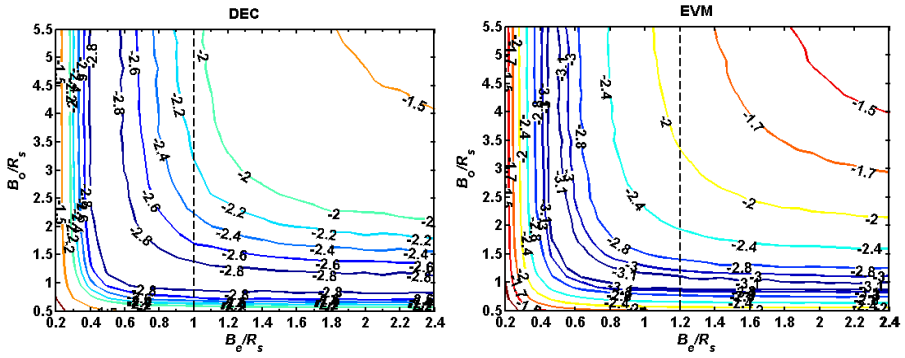

(a) QPSK NRZ

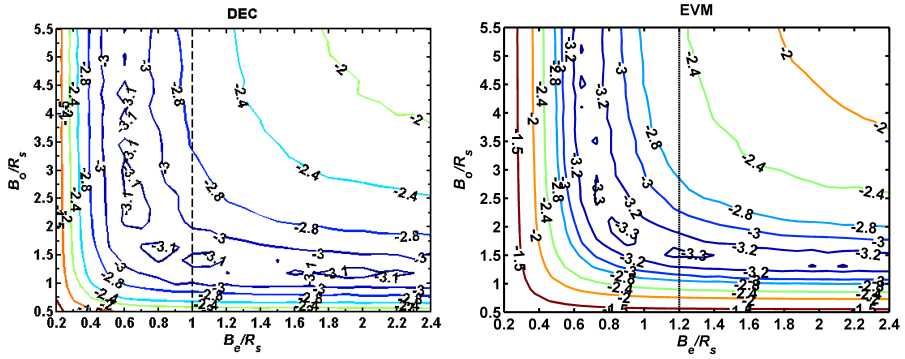

(b) QPSK RZ66

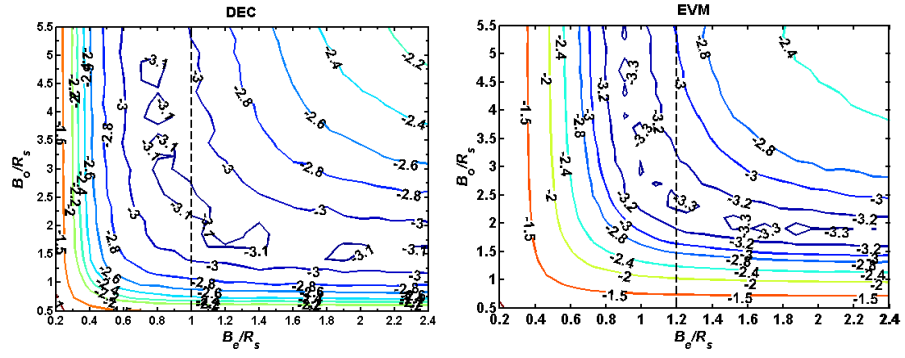

(c) QPSK RZ50

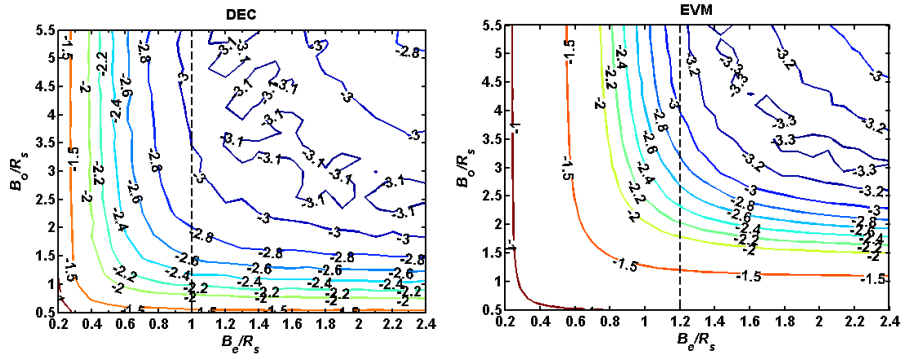

(d) QPSK RZ33

Figure 3.24: Contour plots of the DEC (left side) and the EVM (right side) $\log_{10}(BER)$ estimates as a function of the normalized -3 dB bandwidths of the Gaussian OF and the Gaussian EF, for the QPSK (a) NRZ, (b) RZ66, (c) RZ50 and (d) RZ33 receiver.

Table 3.4: Summary of the -3 dB bandwidths for the GG filters configuration, normalized to R_s, per pulse shape, for the QPSK receiver, considering the DEC and EVM results.

Modulation Format	Pulse Shape	DEC		EVM	
		$B_{e,opt}$	$B_{o,opt}$	$B_{e,opt}$	$B_{o,opt}$
QPSK at 50 Gbps (per polarization)	NRZ	1	1	1.2	1
	RZ66		1.2		1.5
	RZ50		2		2.3
	RZ33		3.5		3.5

3.5.3 Fourth Order Super-Gaussian Optical Filter and Fifth Order Bessel Electrical Filter

Figure 3.25 depicts the BERs estimated using the DEC (left-hand side) and the EVM (right-hand side) as a function of the normalized -3 dB bandwidths for the 4^{th}-order Super-Gaussian OF and the 5^{th}-order Bessel EF.

Figure 3.25 shows that the optimum OF and EF bandwidths estimated by both methods are nearly the same. However, as in the previous filters configurations, a slight difference between the BER estimations of both methods is observed, for these optimum bandwidths. The EVM predicts lower BER values than the DEC. It is also noticed that the receiver performance estimated using the 4GB configuration has slightly improved in comparison with the previous filters pairs. From the left-hand of Figure 3.25(a), it can be seen that for the QPSK NRZ receiver, the lowest $\log_{10}$(BER) estimated using the DEC method is -3.1, while for the GB or the GG configuration is -3 and -2.8, as noticed in Figures 3.21(a) and 3.24(a), respectively.

The reduction of the EF -3 dB bandwidth and the signal duty-cycle leads to a higher discrepancy between both methods BER estimations. Analyzing Figure 3.25(d), concerning the QPSK RZ33 receiver performance, for $B_e/R_s = 0.6$ and $B_o/R_s = 1$, the DEC method estimates a $\log_{10}$(BER) of -1.5, whereas the EVM predicts a $\log_{10}$(BER) of -1.1. A discrepancy between both methods concerning the BER estimations is also noticed for larger filters bandwidths, which is enhanced as the signal duty-cycle decreases. In Figure 3.25(c), the $\log_{10}$(BER) for the QPSK RZ50 receiver having the EF -3 dB bandwidth of $2.4R_s$ and the OF bandwidth of $3.5R_s$ is -2.9 while, for the same filters bandwidths, the EVM estimates a $\log_{10}$(BER) of -2.4. Once again, this discrepancy is attributed to ISI, however, in this case, it is induced by the higher selectivity of the 4^{th}-order Super-Gaussian OF in comparison with the Gaussian OF selectivity.

The filters bandwidths for the 4GB configuration that minimize the BER for the optical coherent receiver for the QPSK signal with different duty-cycles are presented in Table 3.5. The 4GB filters configuration demands larger OF -3 dB bandwidths than the ones predicted by the GB and the GG filters configurations.

The received EDs for the optimized 4GB filters configuration are shown in Figure 3.26. The corresponding ECPs are 1.2, 0.7, 0.8 and 2.6 dB, for the NRZ, RZ66, RZ50 and RZ33 signals, respectively. Comparing with the results of the previous filters configurations, a Super-Gaussian OF with higher order leads to a slightly larger eye-opening, and consequently to a noise margin enlargement, due to its higher selectivity. This partially

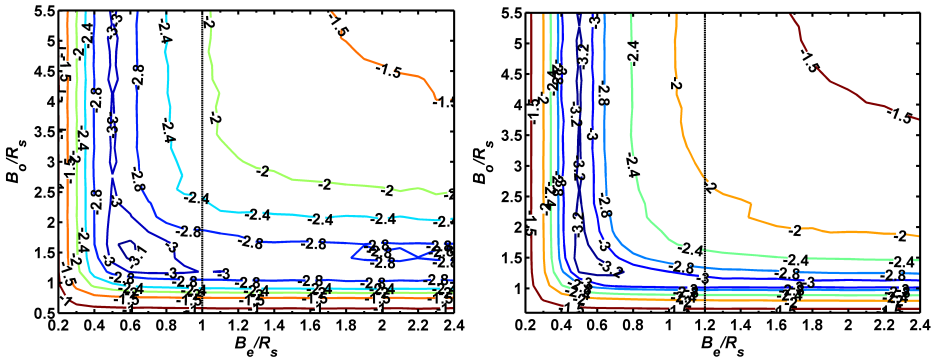

(a) NRZ

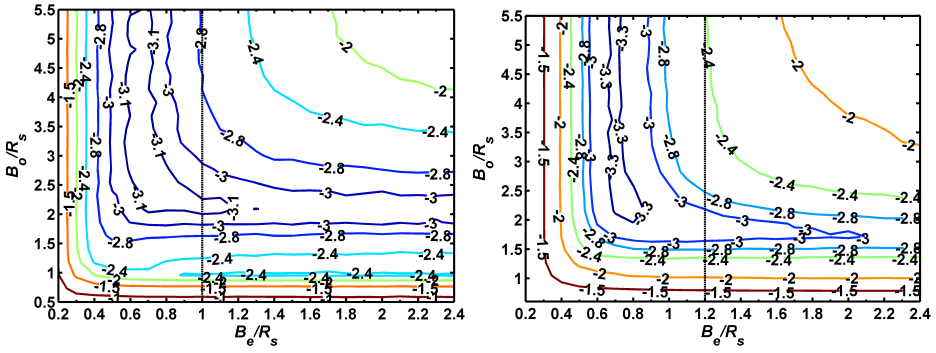

(b) RZ66

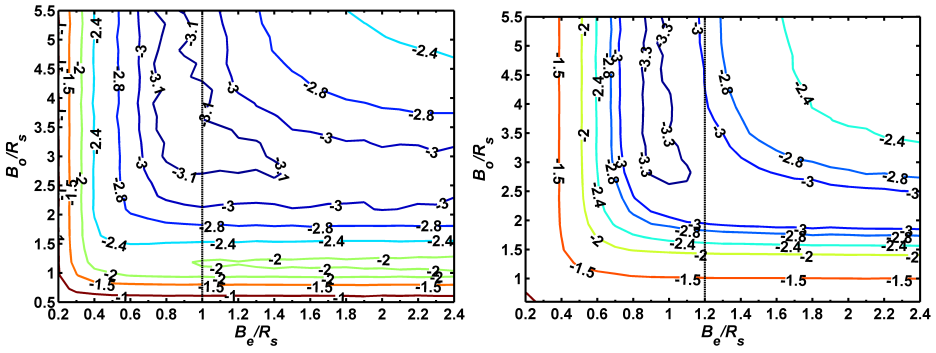

(c) RZ50

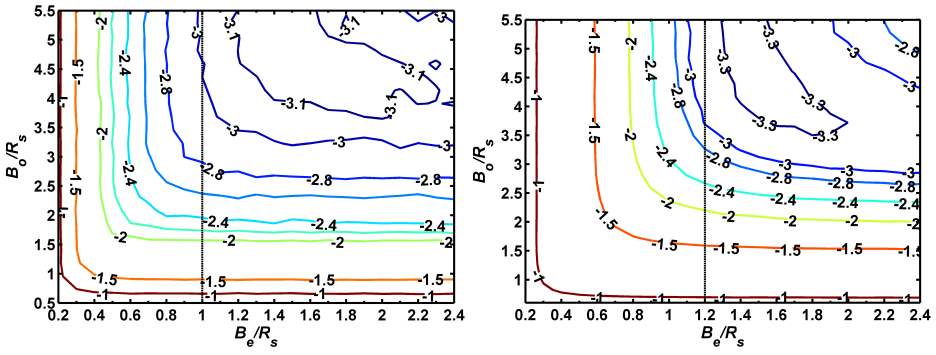

(d) RZ33

Figure 3.25: Contour plots of the DEC (left side) and the EVM (right side) $\log_{10}(BER)$ estimates as a function of the -3 dB bandwidths for the 4^{th}-order Super-Gaussian OF and the 5^{th}-order Bessel EF, for the QPSK (a) NRZ, (b) RZ66, (c) RZ50 and (d)RZ33 receiver.

Table 3.5: Summary of the −3 dB bandwidths for the 4GB filters configuration, normalized to R_s, per pulse shape, for the QPSK receiver, considering the DEC and EVM results.

Modulation Format	Pulse Shape	DEC		EVM	
		$B_{e,opt}$	$B_{o,opt}$	$B_{e,opt}$	$B_{o,opt}$
QPSK at 50 Gbps (per polarization)	NRZ	1	1.2	1.2	1.2
	RZ66		2		2
	RZ50		3		2.8
	RZ33		4		4.2

explains the use of this OF in WDM systems for filtering the channels bandwidths, since it removes the ISI in an efficient way [35].

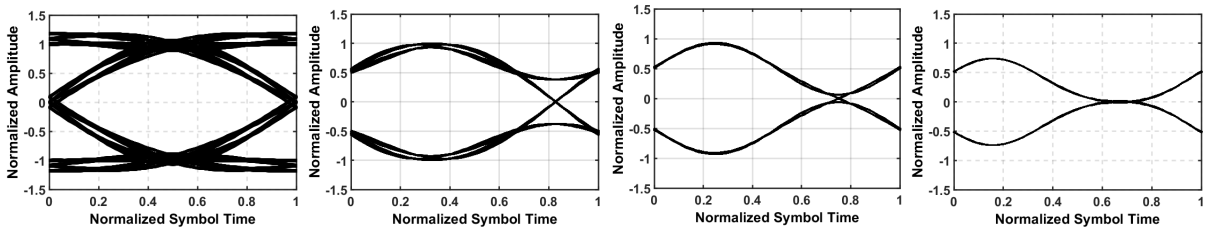

(a) NRZ **(b)** RZ66 **(c)** RZ50 **(d)** RZ33

Figure 3.26: Received eye diagrams of the QPSK modulation format with (a) NRZ, (b) RZ66, (c) RZ50 and (d) RZ33 pulse shapes, after Gaussian OF and 5^{th}-order Bessel EF having the respective optimum −3 dB bandwidths.

3.5.4 Fourth Order Super-Gaussian Optical Filter and Gaussian Electrical Filter

Figure 3.27 depicts the BER of the QPSK performance as a function of the normalized −3 dB bandwidths, for the 4GG filters configuration, using the DEC (left column) and the EVM (right column) methods.

In Figure 3.27, it can be noticed that DEC and EVM predict nearly the same optimum bandwidths for all the considered pulse shapes. The difference lies in the BER estimated for the EF and OF optimum −3 dB bandwidths by each method, as the EVM predicts a $\log_{10}$(BER) of −3.3, while the DEC estimates −3.1, as it can be seen in Figure 3.27(b) to 3.27(d). It is also noticed, that the reduction of the EF −3 dB bandwidth and the signal duty-cycle leads to higher discrepancy between the BER estimations of both methods. For instance, Figure 3.27(d) shows that the DEC method predicts that the $\log_{10}$(BER) of −2.4 is achieved with a EF −3 dB bandwidth of $0.5R_s$ and an OF −3 dB bandwidth of $2.5R_s$, while, for the same filters bandwidths, the EVM estimates a $\log_{10}$(BER) of −1.5.

The BER estimations of each method, considering RZ signals, are mismatched for higher filter bandwidths. Analyzing Figure 3.27(c), the DEC estimates a $\log_{10}$(BER) of −2.8 for the QPSK RZ50 receiver having an OF bandwidth of $3.5R_s$ and an EF bandwidth of $2.4R_s$, whereas the EVM estimates a $\log_{10}$(BER) of −2.4 for the same filters −3 dB bandwidths.

Table 3.6 presents the normalized filters −3 dB bandwidths that minimize the BER for the QPSK coherent

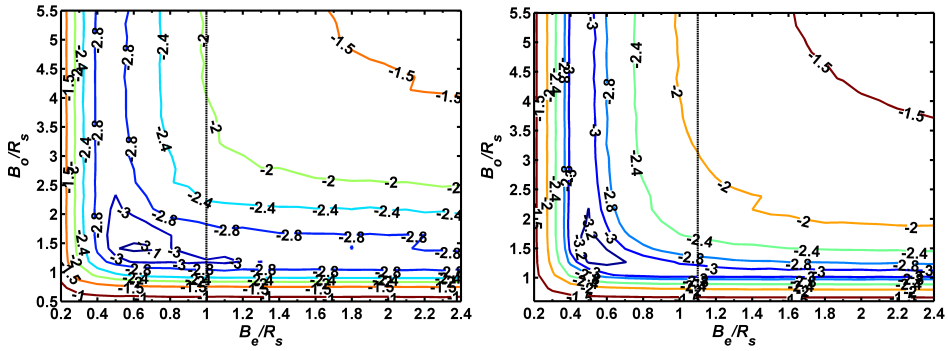

(a) NRZ

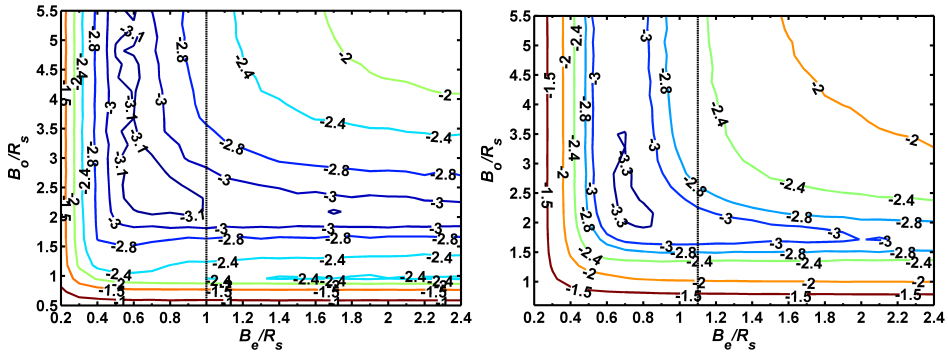

(b) RZ66

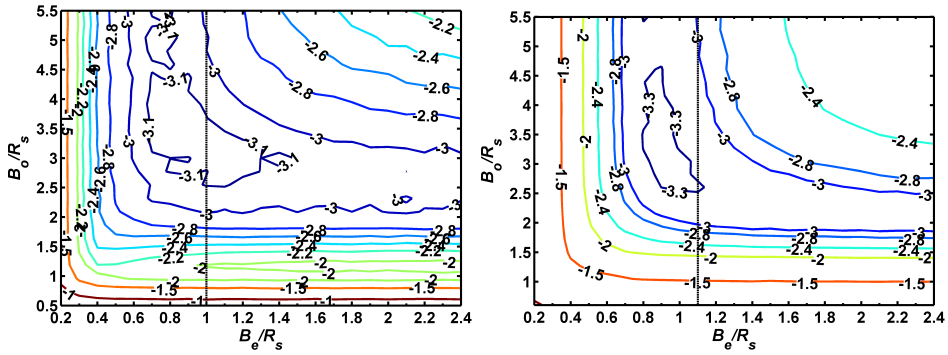

(c) RZ50

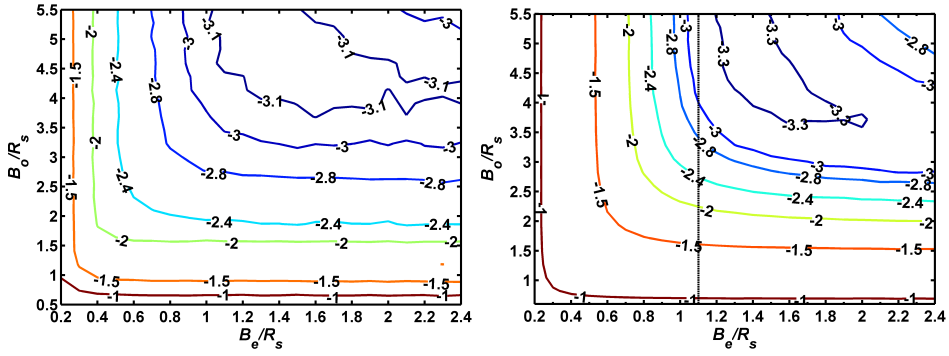

(d) RZ33

Figure 3.27: Contour plots of the DEC (left side) and the EVM (right side) $\log_{10}(BER)$ estimates as a function of the -3 dB bandwidths for the 4^{th}-order Super-Gaussian OF and the Gaussian EF, for the QPSK (a) NRZ, (b) RZ66, (c) RZ50 and (d)RZ33 receiver.

receiver with the 4GG configuration. Comparing with the optimization of the 4GB configuration, the $B_{o,opt}$ are slightly wider for the RZ pulse shapes.

The received eye diagrams for the 4GG configuration are similar to the EDs obtained for the 4GB configuration and the respective ECPs are 1.2, 0.4, 0.7 and 2.2 dB, for the NRZ, RZ66, RZ50 and RZ33 pulse shapes, respectively. Although the ECPs obtained by using the 4GG configuration are slightly lower than the ones obtained from the 4GB pair, in order to achieve the same performance, the 4GG configuration demands larger OF -3 dB bandwidths.

Table 3.6: Summary of the -3 dB bandwidths for the 4GG filters configuration, normalized to R_s, per pulse shape, for the QPSK receiver, considering the DEC and EVM results.

Modulation Format	**Pulse Shape**	**DEC**		**EVM**	
		$B_{e,opt}$	$B_{o,opt}$	$B_{e,opt}$	$B_{o,opt}$
QPSK at 50 Gbps (per polarization)	**NRZ**	1	1.2	1.2	1.2
	RZ66		2.2		2.1
	RZ50		3.1		3
	RZ33		4.7		4.9

3.5.5 Best Filters Configuration for the QPSK Coherent Receiver

The filters configuration for the QPSK receiver, used henceforth in this dissertation, is based on the DEC results, since it is the most accurate method used for the coherent receiver performance assessments. We start by choosing the OF that leads to the best performance, by confronting the 4^{th}-order Super-Gaussian OF with the Gaussian OF results. The 4^{th}-order Super-Gaussian filter allows to have the same EF -3 dB bandwidth of the 5^{th}-order Bessel or the Gaussian EF. Furthermore, since the 4^{th}-order Super-Gaussian has a higher selectivity than the Gaussian OF, it leads to a better receiver performance. Therefore, we choose the 4^{th}-order Super-Gaussian OF to be the best optical filter for the coherent receiver which is used for the remaining work in this dissertation. Then, by only considering the 4GB and the 4GG configurations, our results shows that the 5^{th}-order Bessel EF demands the lowest OF bandwidths in all the received signals and leads to the best receiver performance. So, this filter is the one chosen to study the optical coherent receiver performance.

3.6 Filters Optimization for the 16-QAM Modulation Format

In previous section, we have concluded that the best filters configuration is the 4GB. Therefore, the -3 dB bandwidths of the 4GB configuration is also optimized for the 16-QAM receiver using the DEC and EVM methods. Table 3.2 shows the parameters used in this optimization, differing in the modulation format (which leads to R_s =12.5 Gbaud) and OSNR parameter, which is 14.5 dB. The optimization results are depicted in Figure 3.28.

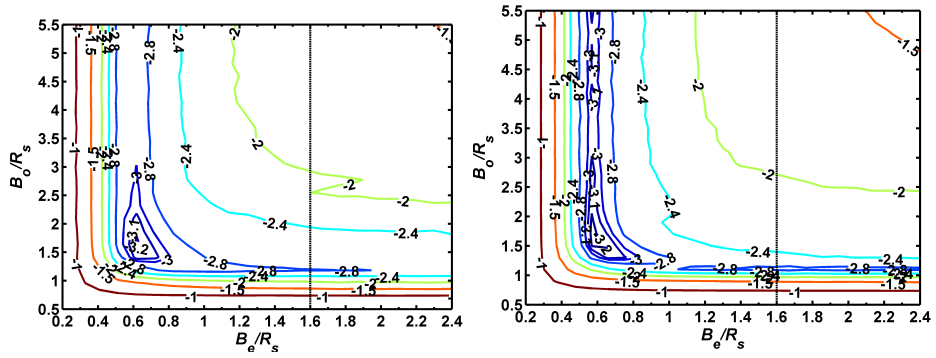

(a) NRZ

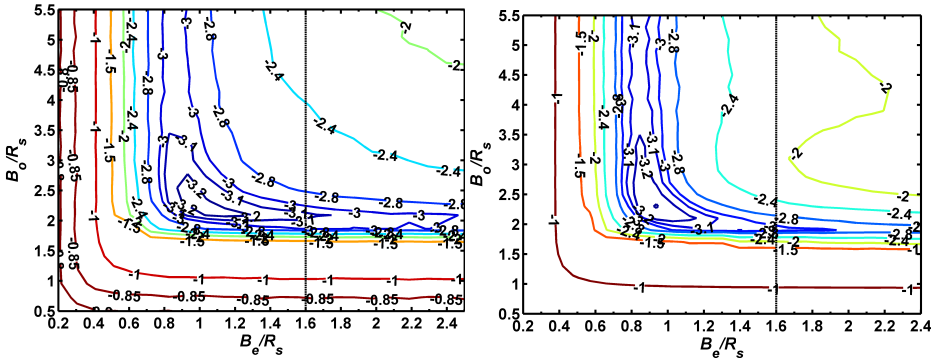

(b) RZ66

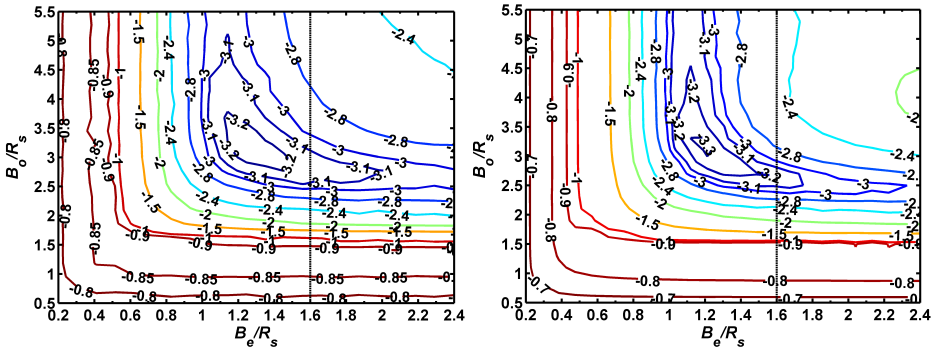

(c) RZ50

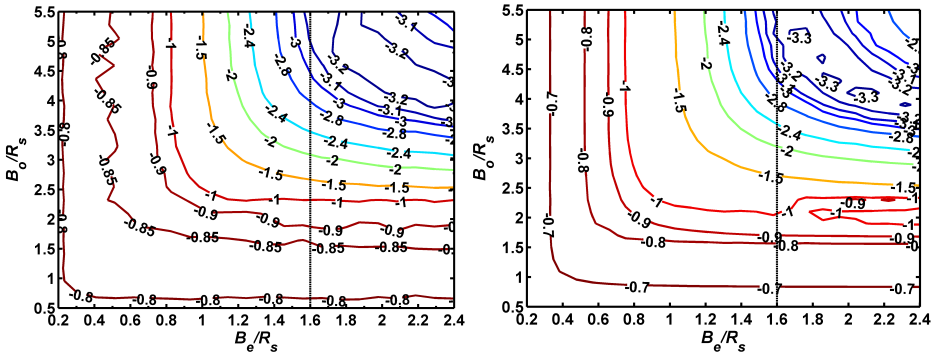

(d) RZ33

Figure 3.28: Contour plots of the DEC (left side) and the EVM (right side) $\log_{10}(BER)$ estimates as a function of the normalized -3 dB bandwidths of the 4^{th}-order Super-Gaussian OF and the 5^{th}-order Bessel EF, with (a) NRZ, (b) RZ66, (c) RZ50 and (d)RZ33 pulse shapes for the 16-QAM receiver.

By inspection of Figure 3.28, the DEC and EVM agree on the predicted optimal filter bandwidths and also in the BER estimations for those bandwidths. Remark that in the QPSK receiver and for all the filters configurations, both methods disagreed slightly in theirs BER estimations for the optimum filters bandwidths. These results are in agreement with [38], where is reported that the accuracy of the EVM estimation for lower BERs improves as the order of the modulation format increases.

Regarding the performance of the receiver for lower EF -3 dB bandwidths, both methods estimate nearly the same BERs. In opposition with the results obtained from the QPSK coherent receiver, shown in Figure 3.25, where a higher discrepancy between both methods BER estimations was noticed when the EF bandwidth was narrower.

At larger filters bandwidths, a discrepancy between the estimates from the EVM method and the DEC method is noticed, which becomes higher as the duty-cycle decreases. Figure 3.28(c) shows that the DEC method estimates a $\log_{10}(\text{BER})$ of -2.9 for the OF bandwidth of $3R_s$ and the EF bandwidth of $2.4R_s$, while the EVM method predicts a $\log_{10}(\text{BER})$ of -2.4 for the same filters bandwidths.

The EF and OF optimum bandwidths for the 16-QAM receiver are presented in Table 3.7. Comparing the optimized OF bandwidths for the 16-QAM receiver with the ones obtained for the QPSK receiver, they are similar. However, the EF -3 dB bandwidths are quite different. This dissimilarity is caused by the more abrupt amplitude symbol transitions in the 16-QAM modulation format, that demands the EF bandwidth enlargement, in order to reduce the ISI caused by those transitions. The same effect was also observed with ideal filtering, concerning the MC simulator validation, presented in section 3.4.

The received EDs for the 16-QAM signal with various duty-cycles at the decision circuit input, for the 4GB filters configuration, are depicted in Figure 3.29. The ECPs are estimated as the average between the three EDs of the 16-QAM eye pattern and they are 2.7 dB for the NRZ; -0.2 dB for the RZ66; -0.1 dB for the RZ50 and 0.6 dB for the RZ33. The increase of the amplitude levels of the signal enhances the ISI at the receiver sampling time instant, resulting in the ECP increase observed for the NRZ pulse shape. Concerning the RZ66 and RZ50 signals, the maximum amplitude levels of the pulses are detected with negligible ISI, and the corresponding ECPs are negligible. Regarding the RZ33 pulse shape, the risetime of the EF filter is slower than the pulse duration, so the maximum signal amplitude is not reached and, consequently the EOP is slightly enhanced.

Table 3.7: Summary of the -3 dB bandwidths optimization, normalized to R_s, per pulse shape, for the 16-QAM receiver, considering the DEC and EVM results.

Modulation Format	**Pulse shape**	**DEC**		**EVM**	
		$B_{e,opt}$	$B_{o,opt}$	$B_{e,opt}$	$B_{o,opt}$
16-QAM	NRZ	1.6	1.2	1.6	1.5
	RZ66		2.5		2.5
	RZ50		3		3
	RZ33		4.7		4.7

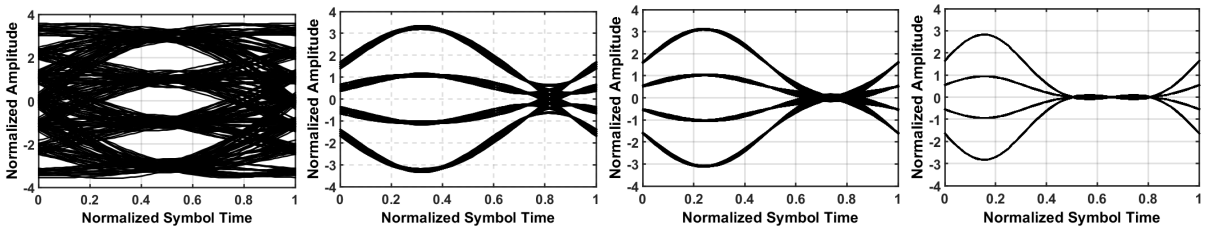

(a) NRZ **(b)** RZ66 **(c)** RZ50 **(d)** RZ33

Figure 3.29: Received eye diagrams of the 16-QAM modulation format with (a) NRZ, (b) RZ66, (c) RZ50 and (d) RZ33 pulse shapes, after the fourth order Super-Gaussian OF and fifth order Bessel EF having the respective optimum -3 dB bandwidths.

3.7 Conclusions

In this chapter, the OFs and the EFs used in this work were characterized. Then, this chapter was devoted to the performance assessment of the coherent receiver, in presence of ASE noise using two methods: the DEC and the EVM. The comparison between the EVM and the DEC BER estimates with the theoretical BER for QPSK, 16-QAM and 64-QAM modulation formats allowed the MC simulator validation: both BER estimation methods practically overlapped the BER theoretical results, considering filter bandwidths larger than B_o/R_s=10, where the assumptions of the theoretical derivation still hold. Since the theoretical model assumes the absence of ISI on the received signal, discrepancies between the simulation estimations of the receiver performance and the theoretical BER were noticed for narrow filter bandwidths, where the ISI is dominant. Furthermore, we also have demonstrated that as the modulation format order increases, the receiver filter bandwidth must be larger, in order to get the same BER predictions using the simulation and theory. This was attributed to the abrupt transitions of the signal pulse, which after filtering lead to higher signal distortion and consequently, to the ISI enhancement.

Additionally, we have concluded that the EVM and DEC agree in their assessments, but the EVM requires less computational effort. The EVM results stabilize with significantly less sample functions then the required by the DEC method. This conclusion has more importance when estimating very low BERs.

Then, with the simulator validated, the optimization of the -3 dB bandwidth for several non-ideal filters, using the DEC and EVM methods, in order to achieve the best performance of the QPSK and 16-QAM coherent receivers was performed considering NRZ, RZ66, RZ50 and RZ33 pulse shapes. The optimization allowed to conclude that the 4^{th}-order Super-Gaussian OF, having a higher selectivity than the Gaussian OF, leads to a more efficient ASE noise filtering. In other hand, due to its higher selectivity, this filter causes more ISI, when the signal bandwidth is too large, therefore demanding a larger EF bandwidth as the signal duty-cycle decreases, in order to minimize the BER. The EF that exhibited the best performance was the 5^{th}-order Bessel filter, since it allows to reduce the OF -3 dB bandwidths. This conclusion holds for each duty-cycle studied.

Additionally, the EVM accuracy was studied in comparison with the DEC estimations, in a non-ideal filtering scenario. For all the modulation formats and pulse shapes, both methods estimated practically the same optimum filter bandwidths. Therefore, it can be concluded that the EVM is a good performance method regarding the optimization of the filters bandwidths. However, in the QPSK receiver optimization, discrepancies between the BER estimation from both methods were observed, especially when considering lower EF bandwidths. For the 16-QAM receiver, both methods are in a better agreement regarding the BER estimations for narrow EF bandwidths, in comparison with the QPSK coherent receiver.

Chapter 4

M-QAM Receiver Performance in Presence of In-Band Crosstalk

4.1 Introduction

In this chapter, the performance of a M-QAM coherent receiver impaired by in-band crosstalk and ASE noise is analyzed in a back-to-back configuration using MC simulation.

In section 4.2, the in-band crosstalk origin in an optical network is described. Then, in section 4.3, the implementation of the in-band crosstalk on the MC simulation is presented and its validation is also performed.

In section 4.4, the impact of in-band crosstalk on the coherent receiver performance, considering the QPSK modulation format as the original signal is studied and discussed. This study is performed by estimating the OSNR penalty caused by a single interferer in three distinct scenarios: in section 4.4.1, the modulation formats of the interfering signals can have equal or higher order than the selected signal modulation format (bit rate and duty-cycle of crosstalk and selected signals are the same); in section 4.4.2, the interfering signal and the selected signal have the same modulation format and bit rate, but the duty-cycle of the interfering signal is changed; in section 4.4.3, the interference due to different modulation formats with different bit rates is studied.

The coherent receiver performance considering the 16-QAM modulation format as the original signal in presence of in-band crosstalk is studied and discussed in section 4.5.

Additionally, and throughout this chapter, the accuracy of the EVM method in presence of in-band crosstalk is evaluated by comparison with the results obtained using the DEC method. Finally, the conclusions of this chapter are drawn in section 4.6.

4.2 In-Band Crosstalk Origin

Crosstalk is a physical impairment caused by the imperfect isolation of the optical components (de/multiplexers, switches) inside an optical node, e.g. ROADM [12]. This imperfection isolation originates signal power leakage inside each optical network node, and causes interference between the signals that are being transmitted through the optical link. There are two forms of crosstalk: out-of-band crosstalk and in-band crosstalk, as depicted schematically in Figure 4.1, where the crosstalk signal is represented as XT.

The out-of-band crosstalk is less detrimental to the optical network performance, since it arises when the wavelength spacing between the crosstalk signal centered at λ_{XT} and the selected signal centered at λ_0 is larger than the receiver bandwidth [12], and can be fully suppressed with a narrow-band filter at the receiver, as shown in Figure 4.1(a). On the other hand, in the case of in-band crosstalk, when $\lambda_{XT} \approx \lambda_0$, the degradation of the network performance is superior since the interfering signal cannot be removed by filtering [12]. This type of crosstalk is illustrated in Figure 4.1(b).

In an optical network, the selected signal suffers accumulative crosstalk interference, as it is propagated through several network nodes as exemplified in Figure 4.2. On the left-hand side of Figure 4.2, two optical signals, with the same wavelength, λ_0, enter the network from different sources and having different destinations. The black optical signal represents the selected signal and the red optical signal is the interfering signal. The path of each optical signal is represented by arrows with the same color as the optical signal. The dashed arrows represent the optical power leakage originated by imperfect switching inside the ROADMs. The selected signal arrives at the destination of the selected signal (right bottom of the Figure 4.2) carrying the interference of the optical signal represented in red. The crosstalk signal can be a replica of the selected signal, depending of the path followed through the optical network and the differential delay between the crosstalk signal and the coherence time of the source, If the delay is less than the source coherence time, then the crosstalk is called coherent in-band crosstalk, otherwise is called incoherent in-band crosstalk [13]. In this dissertation, we assumed that the in-band crosstalk is originated by different sources, and so, we only considered incoherent in-band crosstalk.

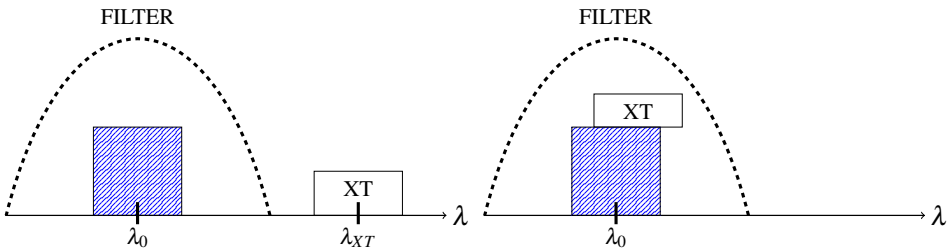

(a) Out-of-band crosstalk **(b)** In-band crosstalk

Figure 4.1: Different types of crosstalk.

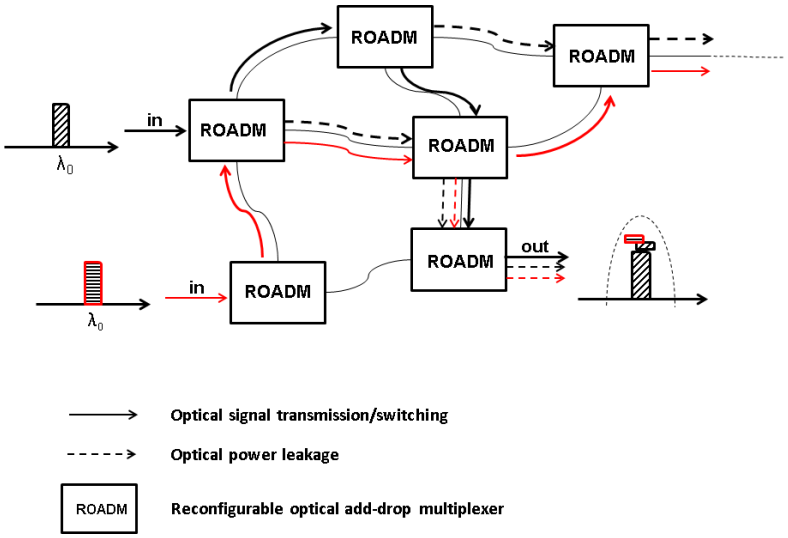

Figure 4.2: Optical network with in-band crosstalk coming from different sources.

4.3 Crosstalk Simulation Model and Validation

In this section, the influence of in-band crosstalk on a M-QAM coherent receiver is described analytically and the MC simulation model for the in-band crosstalk is presented.

4.3.1 Simulation Model Description

The total electrical field of the lowpass equivalent of an optical signal, at the input of the coherent receiver (Figure 2.9), in the presence of ASE noise and in-band crosstalk can be expressed by

$$E_r(t) = E_0(t) + \sum_{i=1}^{N_x} E_{x,i}(t - t_i)e^{j\phi_{\varepsilon,i}} + N_0(t) \tag{4.1}$$

where $E_0(t)$ is the electrical field of the selected optical signal, $E_{x,i}(t)$ is the electrical field corresponding to one of N_x interfering signals. t_i and $\phi_{\varepsilon,i}$ are, respectively, the time delay and the phase error between the selected and i-th interfering signals. The crosstalk level $X_{c,i}$ of each interferer is defined as

$$X_{c,i} = \frac{P_{x,i}}{P_0} \tag{4.2}$$

where $P_{x,i}$ is the average power of the i-th interfering signal and P_0 represents the average power of the selected signal. Assuming that all interfering signals are equal, i.e. $E_{x,i}(t) = E_x(t)$ and by omitting the dependence on t_i and $\phi_{\varepsilon,i}$, Equation (4.1) can be rewritten as [14]

$$E_r(t) = [E_0(t) + N_x E_x(t)] + N_0(t) \tag{4.3}$$

By following Figure 2.13, the resulting photocurrent in each photodetector, modeled as a square-law detection, is

$$\begin{aligned} I_1(t) &= \frac{1}{4}\left|[(E_0(t)+N_xE_x(t)+N_0(t)]+E_{LO}(t)\right|^2 \\ I_2(t) &= \frac{1}{4}\left|[(E_0(t)+N_xE_x(t)+N_0(t)]+jE_{LO}(t)\right|^2 \\ I_3(t) &= \frac{1}{4}\left|[(E_0(t)+N_xE_x(t)+N_0(t)]-E_{LO}(t)\right|^2 \\ I_4(t) &= \frac{1}{4}\left|[(E_0(t)+N_xE_x(t)+N_0(t)]-jE_{LO}(t)\right|^2 \end{aligned} \tag{4.4}$$

So, by developing the absolute square in each term, we have:

$$\begin{aligned} I_1(t) = \frac{1}{4}\big[\big[\big[|E_0|^2+N_x^2|E_x|^2+2N_x\Re\{E_0E_x^*\}\big] &+|N_0|^2+2\Re\{(E_0+N_xE_x)N_0^*\}]+|E_{LO}|^2 \\ &-2\Re\{(E_0+N_xE_x)E_{LO}^*+N_0E_{LO}^*\}] \\ I_2(t) = \frac{1}{4}\big[\big[\big[|E_0|^2+N_x^2|E_x|^2+2N_x\Re\{E_0E_x^*\}\big] &+|N_0|^2+2\Re\{(E_0+N_xE_x)N_0^*\}]+|E_{LO}|^2 \\ &+2\Re\{(E_0+N_xE_x)E_{LO}^*+N_0E_{LO}^*\}] \\ I_3(t) = \frac{1}{4}\big[\big[\big[|E_0|^2+N_x^2|E_x|^2+2N_x\Re\{E_0E_x^*\}\big] &+|N_0|^2+2\Re\{(E_0+N_xE_x)N_0^*\}]+|E_{LO}|^2 \\ &-2\Im\{(E_0+N_xE_x)E_{LO}^*+N_0E_{LO}^*\}] \\ I_4(t) = \frac{1}{4}\big[\big[\big[|E_0|^2+N_x^2|E_x|^2+2N_x\Re\{E_0E_x^*\}\big] &+|N_0|^2+2\Re\{(E_0+N_xE_x)N_0^*\}]+|E_{LO}|^2 \\ &+2\Im\{(E_0+N_xE_x)E_{LO}^*+N_0E_{LO}^*\}] \end{aligned} \tag{4.5}$$

where the time dependence was omitted.

Comparing with the photocurrents derived in Equation (2.24), three additional beat terms appear: the signal-crosstalk beating term denoted by $E_0E_x^*$ is known as interferometric beat noise [13], the term $N_x|E_x|^2$ is the crosstalk-crosstalk beating [14] and $N_xE_xE_{LO}^*$ is the N_x crosstalk-LO signal beating. Finally, as the I component is given by $I_I(t)=I_2(t)-I_1(t)$ and the Q component by $I_Q(t)=I_4(t)-I_3(t)$, the currents at the OQF output are

$$I_I(t) = \Re\{(E_0(t)+N_xE_x(t))E_{LO}^*(t)+N_0(t)E_{LO}^*(t)\} \tag{4.6}$$

$$I_Q(t) = \Im\{(E_0(t)+N_xE_x(t))E_{LO}^*(t)+N_0(t)E_{LO}^*(t)\} \tag{4.7}$$

which means that the coherent receiver fully eliminates the interferometric noise. This feature has a significant importance, since this type of noise is characterized as an important source of performance degradation in direct detection receivers [44]. In these receivers, the interferometric noise can lead to a non-Gaussian statistic distribution of the received decision variable, making the performance analysis more difficult, since this noise becomes hard to be modeled [13], [14].

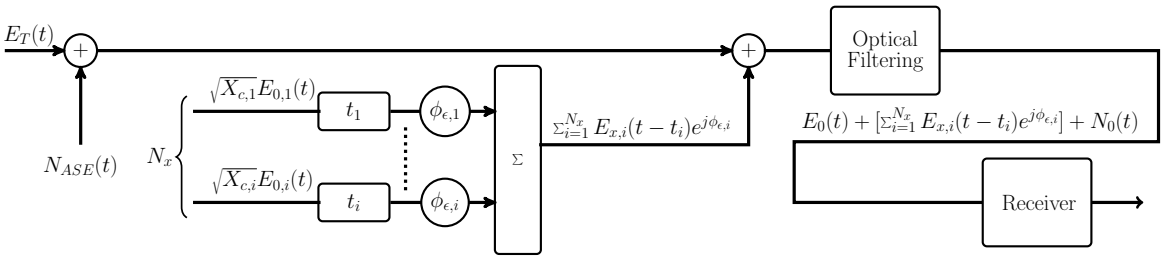

Figure 4.3: Crosstalk simulation model for one sample function of in-band crosstalk and ASE noise in one polarization.

Figure 4.3 depicts the implementation of the crosstalk model in the MC simulation and it is based on the analytical description of the in-band crosstalk previously presented. In each iteration of the MC simulator, a crosstalk sample function is added to the optical signal, after the addition of an ASE noise sample function. Each crosstalk sample function can consider N_x interferers. In this work, as a worst case assumption, it is assume that the interferers and selected signal have the same polarization. Each interfering signal sample function is composed of a random symbols sequence with the same size as the selected signal symbols sequence. Then, each crosstalk symbols sequence is generated accordingly to the desired modulation format, using the symbol mapping presented in Tables 2.1, 2.2 and 2.3. Finally, the average power of the i-th interferer is changed accordingly with Equation (4.2), resulting in the i-th interfering signal $E_{x,i}(t)$. In order to simulate the time misalignment and the phase difference impairments between the interferer and the selected signal, a time delay t_i is modeled as a uniformly distributed random variable between 0 and T_s [45] and a phase noise has a uniform distribution within the interval $[0, 2\pi]$ [45] are imposed on the i-th interferer sample function. Finally, all N_x interfering signals are summed and added to the selected signal, resulting in an optical signal with ASE noise and in-band crosstalk, which is filtered by the OF and gives the electrical field defined in Equation (4.1), which in a back-to-back situation arrives at coherent receiver input.

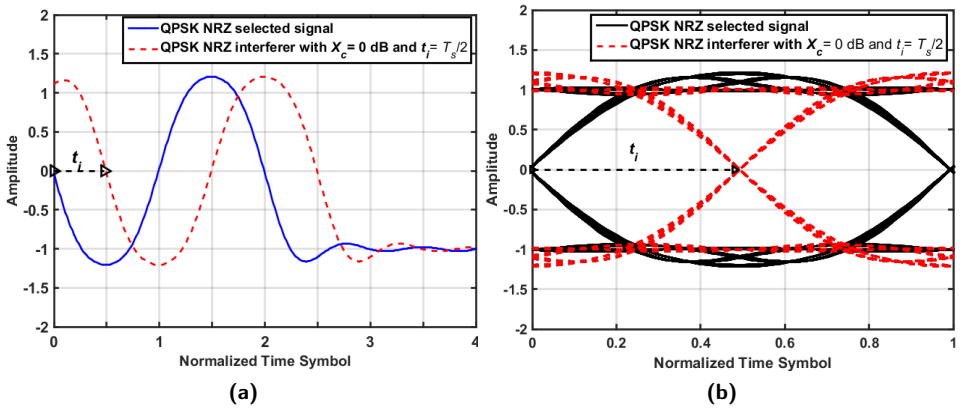

Figure 4.4: (a) Time misalignment simulation, exemplified using a QPSK NRZ single interferer with a time mismatch of $T_s/2$ in relation with the QPSK NRZ original signal, with X_c =0 dB and the (b) corresponding eye diagram.

The simulation of the time misalignment between the selected signal and a single interfering signal is illustrated in Figure 4.4. The time misalignment impairment is simulated by shifting the position of the vector corresponding to the interfering symbols sequence, according with the desired time mismatch. Figure 4.4(a) exemplifies a $T_s/2$ time mismatch between a QPSK NRZ selected signal and a QPSK NRZ interfering signal having a crosstalk level of 0 dB, and the corresponding eye diagram is shown in Figure 4.4(b).

Figure 4.5 depicts the phase noise impact on the received constellation. Figure 4.5(a) depicts the received constellation with a single interfering signal having a null phase difference in relation to the original signal, which results in a symbols dispersion with a rectangular shape. In Figure 4.5(b), the constellation with 45° phase difference is shown, where it can be observed a 45° rotation of the symbols dispersion comparing with the constellation depicted in Figure 4.5(a) [20].

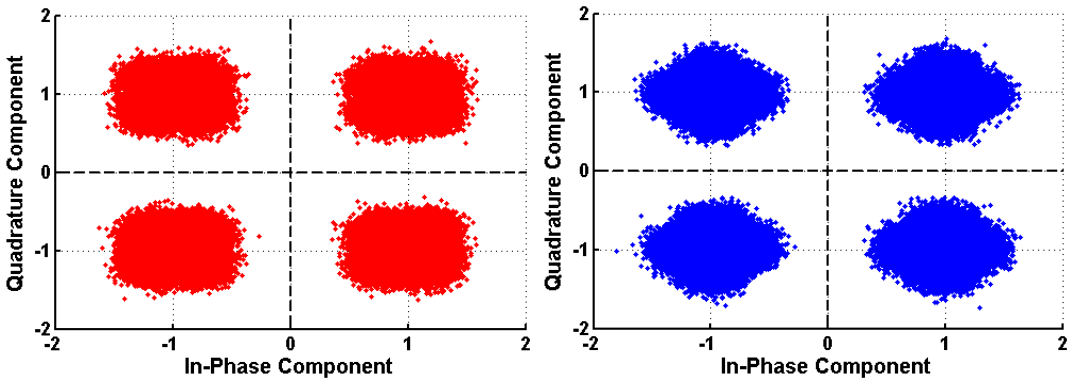

(a) 0° phase noise. **(b)** 45° phase noise.

Figure 4.5: Impact of (a) 0° and (b) 45° phase difference on the constellation of the selected signal.

4.3.2 Validation of the MC Simulator

In order to validate the simulation model presented in Figure 4.3, the probability density functions (PDF)s of the decision variable for the QPSK NRZ selected signal with a QPSK NRZ interfering signal having $X_c = -25, -15$ and -5 dB are obtained and depicted in Figure 4.6. The OSNR is 50 dB, with the intention of neglecting the ASE noise, with the PDFs solely reflecting the in-band crosstalk impact on the statistical distribution of the received decision variable. From Figure 4.6, it is noticed that the increase of the crosstalk level leads to the increase of the variance of the decision variable, since the respective PDFs become larger for higher crosstalk levels. The corresponding BER will also increase since the inside tails of the PDFs become closer. Additionally, it is clear that the PDFs of the decision variable with a single interferer and in absence of ASE noise do not follow a Gaussian distribution, as also shown in [14].

The impact of the crosstalk is evaluated by quantifying the OSNR penalty at the BER of 10^{-3} [20]. The

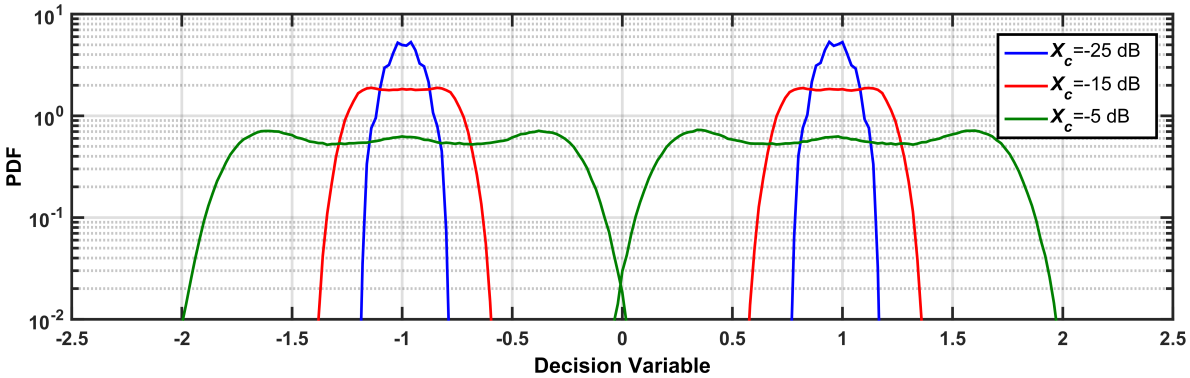

Figure 4.6: PDFs of the QPSK NRZ received signal for an OSNR of 50 dB and a single QPSK NRZ interferer with the crosstalk levels of $-25, -15$ and -5 dB.

crosstalk level that leads to a 1 dB OSNR degradation is defined as $X_{c,max}$. The $X_{c,max}$ estimation starts by finding the OSNR that leads to the BER of 10^{-3} for each modulation format and duty-cycle, without crosstalk. Then, in the next iterations of the MC simulator, a crosstalk signal sample function with a determined modulation format and a specific duty-cycle is added to the selected signal and the BER of the receiver is evaluated. In the simulation, the crosstalk level is inside the interval $[-40, -5]$ dB, and the OSNR is changed in order to achieve BER estimates between 10^{-4} and 10^{-2}. Then, the OSNR for the BER of 10^{-3} is obtained using a linear regression of the logarithm of the BER estimates and the OSNR penalty due to crosstalk is evaluated by calculating the difference, δ_{XT}, between the linear regressions of $\log_{10}(BER)$, obtained with a specific crosstalk value and without crosstalk. This procedure is repeated for each crosstalk level.

Figure 4.7 shows an example of how the OSNR penalty due to a QPSK NRZ interfering signal is estimated using the MC simulation. In this case, the selected signal is also a QPSK NRZ having an OSNR of 10.4 dB and the filters bandwidths are $1.2R_s$ for the 4^{th}-order Super-Gaussian OF and R_s for 5^{th}-order Bessel EF. The

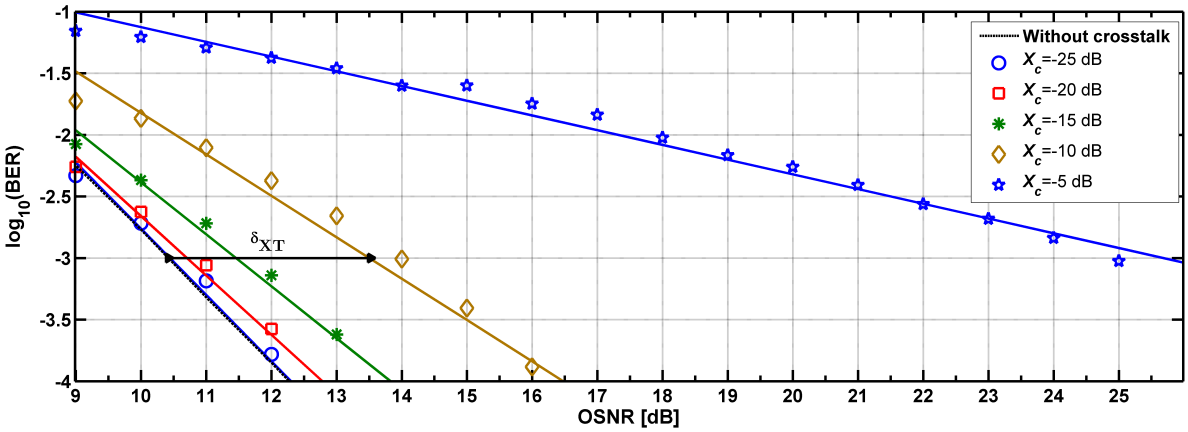

Figure 4.7: BER as a function of the OSNR for a QPSK NRZ interfering signal. The linear regression used to estimate the δ_{XT} is also shown by the solid lines.

OSNR penalty for a crosstalk level of -10 dB is indicated in the figure. In this case, the OSNR penalty is approximately 3 dB. From this figure, it can be also concluded that the crosstalk level of -25 dB leads to a negligible performance degradation, since the performance estimations with crosstalk overlap the predicted receiver performance without crosstalk.

The validation of the coherent receiver simulation in the presence of in-band crosstalk is done by comparing the results of Figure 4.8 with the results found in [20], where the OSNR penalty at the BER of 10^{-3} is calculated, in a back-to-back coherent receiver at a symbol rate of 21.4 Gbaud and considering a single interfering signal with the same modulation format as the selected signal QPSK, 16-QAM and 64-QAM modulation formats. The crosstalk levels for a 1 dB OSNR penalty from Figure 4.8 are in complete agreement with the results found in [20]. Figure 4.8 shows that the crosstalk levels for a 1 dB OSNR penalty are approximately -16, -23, and -32 dB for the QPSK, 16-QAM, and 64-QAM modulation format, respectively, as in [20]. The QPSK is the most robust M-QAM modulation format in presence of in-band crosstalk, since it is the one that exhibits a higher crosstalk level for a 1 dB OSNR degradation. From Figure 4.8, it can be also concluded that as the order of the selected signal modulation format increases, the receiver tolerance to in-band crosstalk is worsened [20], since the $X_{c,max}$ decreases with the increase of the modulation format order of the selected signal. So, the estimation of the receiver performance in presence of ASE noise and in-band crosstalk, through the MC simulation, can be considered validated.

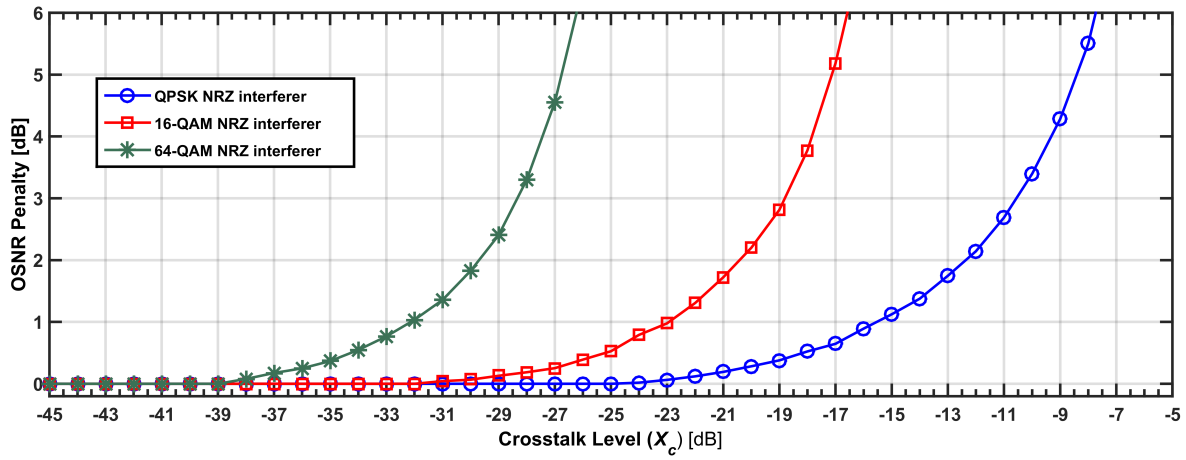

Figure 4.8: OSNR penalty as a function of the crosstalk level for a single interfering crosstalk signal considering the modulation formats QPSK, 16-QAM and 64-QAM with a symbol rate of 21.4 GBaud.

4.4 QPSK Receiver Performance in Presence of In-band Crosstalk

This section describes the study of the impact of the in-band crosstalk on the coherent receiver performance due to a single interfering term for a 4-QAM/QPSK selected signal at the binary rate of 50 Gbps. Moreover,

the in-band crosstalk can be considered to be dominated by a single interferer [46], and hence, the impact of the in-band crosstalk will be analyzed, throughout this dissertation, considering a single interfering signal. The OSNR degradation due to the in-band crosstalk will be estimated using the DEC and EVM methods.

As detailed in section 4.3.2, the OSNR penalty estimation due to in-band crosstalk has the reference defined by the required OSNR to get the BER of 10^{-3} without in-band crosstalk. So, in Table 4.1, the OSNRs that lead to a BER of 10^{-3} in each QPSK signal duty-cycle are presented, considering the DEC and the EVM estimation. The normalized filters -3 dB bandwidths are also indicated for each selected signal duty-cycle, which were obtained from the filters optimization, performed using the DEC method in chapter 3, for the QPSK receiver having the 4GB filter configuration.

Table 4.1: Required OSNR, without in-band crosstalk, for the QPSK receiver to reach a BER of 10^{-3} per pulse shape, using the indicated -3 dB bandwidths normalized to the symbol rate for the EF and the OF.

Modulation format	**Duty-Cycle**	**OSNR [dB]**		**EF**[1] **[$/R_s$]**		**OF**[2] **[$/R_s$]**	
		DEC	**EVM**	**DEC**	**EVM**	**DEC**	**EVM**
QPSK at 50 Gbps (per polarization)	100%	10.5	10.3	1		1.2	
	66%	10.3	10.2			2	
	50%	10.2	9.8			3	
	33%	10.5	12.4			4	

4.4.1 Different Modulation Format Orders

Figure 4.9 depicts the DEC (left-hand side) and the EVM (right-hand side) estimations of the OSNR penalty as a function of the crosstalk level for a QPSK original optical signal with different modulation format orders on the interfering signal but with the same pulse shape and bit rate as the original signal.

Regarding the DEC estimations, it can be concluded that the QPSK crosstalk signal leads to a lower OSNR degradation than the 16-QAM and 64-QAM interferers. Furthermore, Figure 4.9 shows also that the crosstalk tolerance to a 64-QAM interferer is slightly lower than the tolerance to the 16-QAM interfering signal, and this effect is enhanced with the reduction of the duty-cycle. For example, for a duty-cycle of 33%, the estimated crosstalk levels for a 1 dB OSNR penalty are -12 dB, -14 dB, and -15 dB, respectively for the QPSK, 16-QAM and 64-QAM modulation formats on the crosstalk signal. It can be also concluded that the reduction of the selected signal duty-cycle enhances the crosstalk tolerance [47]. This improvement is particularly relevant comparing the $X_{c,max}$ for the QPSK NRZ selected signal (Figure 4.9(a)) with the RZ selected signals, depicted in Figures 4.9(b) to 4.9(d). From Figure 4.9(a), it can be observed that the $X_{c,max}$ for each interferer in a QPSK NRZ receiver is at least 2 dB lower than the ones found for the QPSK RZ receivers.

From inspection of the right-hand side of Figure 4.9(a) and 4.9(b), concerning the EVM estimations for the

[1] 5^{th}-order Bessel filter
[2] 4^{th}-order Super-Gaussian filter

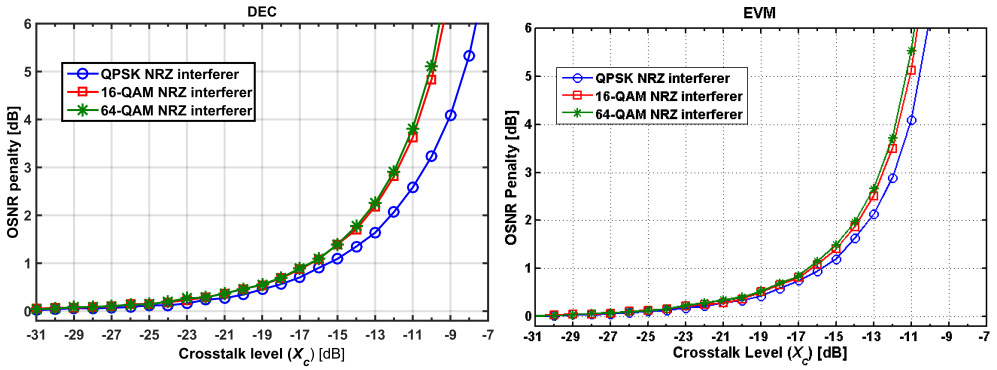

(a) QPSK NRZ

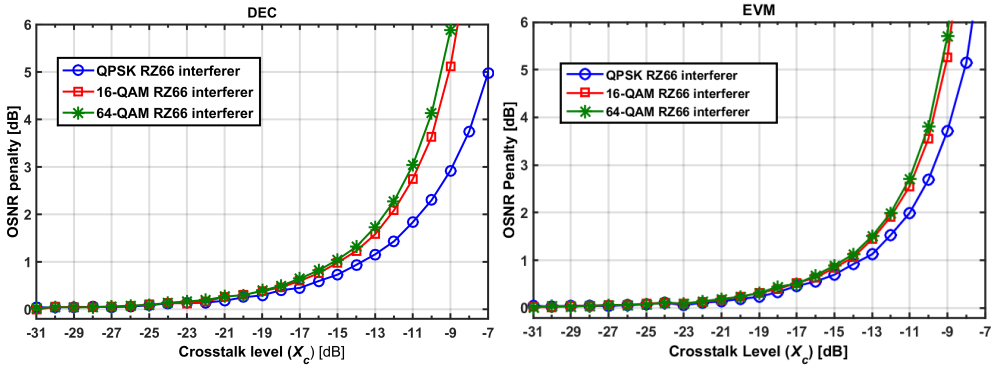

(b) QPSK RZ66

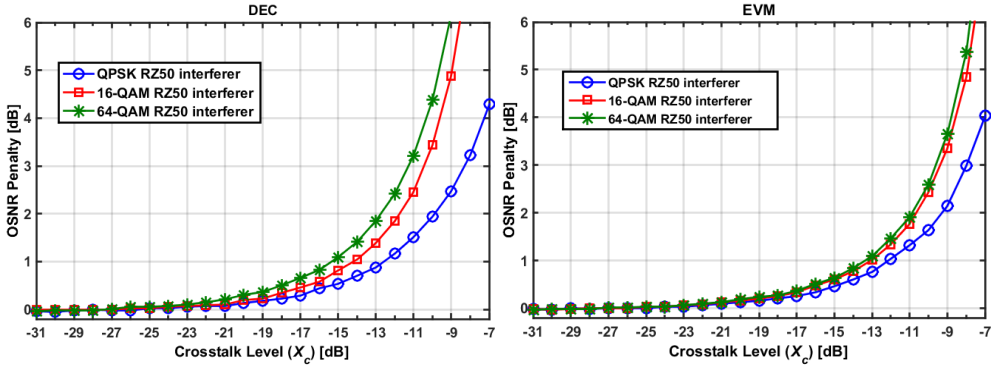

(c) QPSK RZ50

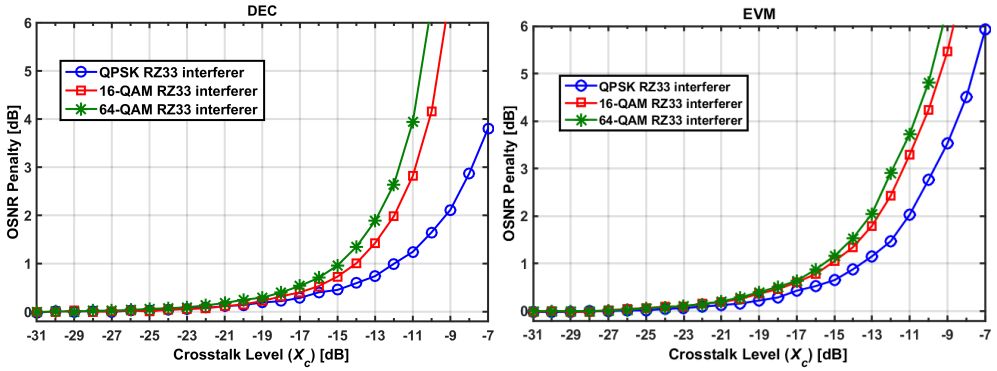

(d) QPSK RZ33

Figure 4.9: OSNR penalty as a function of the crosstalk level due to a single interfering signal with different modulation formats but having the same pulse shape as the (a) QPSK NRZ, (b) QPSK RZ66 (c) QPSK RZ50 and (d) QPSK RZ33 selected optical signal.

QPSK NRZ and RZ66 receiver, respectively, an agreement with the DEC results concerning the $X_{c,max}$ predictions is noticed. However, for lower duty-cycles of the selected signal, a discrepancy between both methods is visible. For example, the right-hand side of Figure 4.9(c) shows that the EVM predicts that the interference of a 64-QAM RZ50 signal, with a crosstalk level of nearly -13 dB leads to a 1 dB OSNR penalty at the QPSK RZ50 receiver, while the DEC estimates a crosstalk level of -15 dB for the same OSNR degradation and interfering signal. In the same figure, for the remaining crosstalk signals, the EVM estimations for each $X_{c,max}$ are more than 1 dB higher than the ones predicted by the DEC method. In Figure 4.9(d), which concerns to the QPSK RZ33 selected signal, it can be observed that the $X_{c,max}$ estimations from the EVM method are more than 1 dB higher than the DEC estimation for the QPSK RZ33,16-QAM RZ33 and 64-QAM interferers. Finally, the EVM predictions for the OSNR penalty clearly disagree with the DEC estimations for higher crosstalk levels.

Since the EVM estimation is based on the comparison between the received constellation and the transmitted constellation, the discrepancies between the EVM and the DEC estimations for the $X_{c,max}$ at the QPSK RZ50 and the QPSK RZ33 coherent receiver, noticed in Figure 4.9(c) and 4.9(d) respectively, are investigated

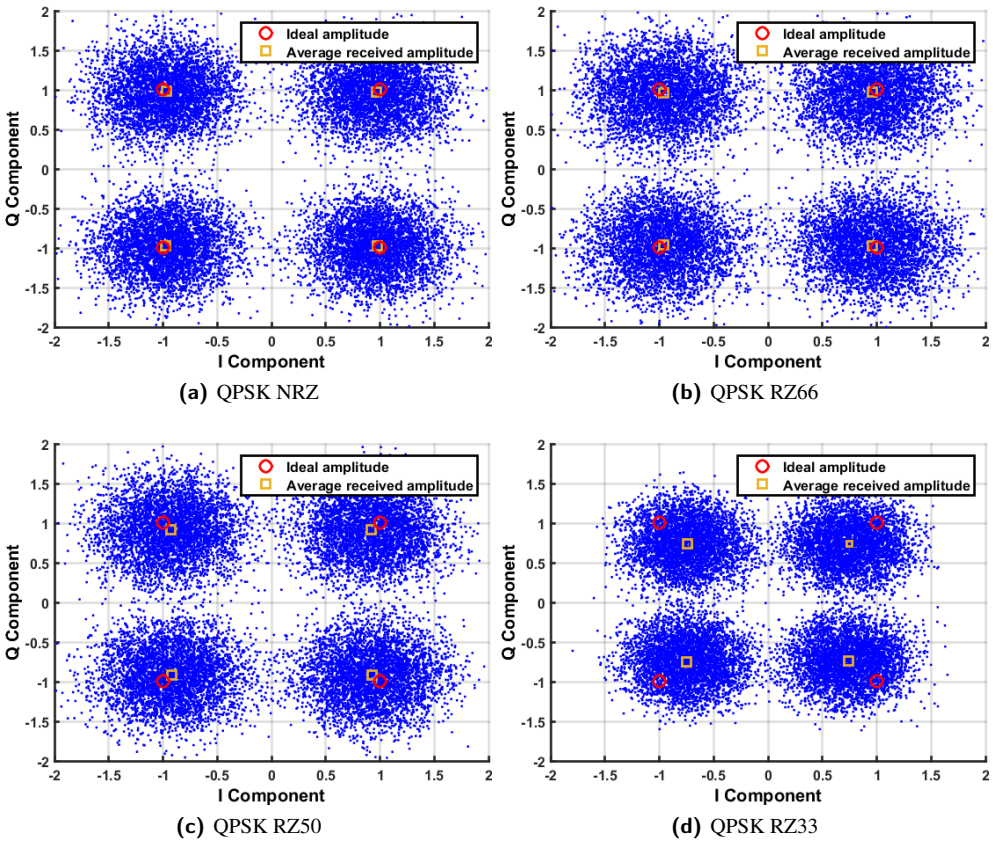

(a) QPSK NRZ **(b)** QPSK RZ66

(c) QPSK RZ50 **(d)** QPSK RZ33

Figure 4.10: Received constellations of the QPSK selected signal with a QPSK interfering signal having the corresponding crosstalk level for 1 dB OSNR degradation for the (a) QPSK NRZ, (b) QPSK RZ66, (c) QPSK RZ50 and (c) QPSK RZ33 pulse shapes, respectively.

by inspection of the constellation of the received signal impaired by in-band crosstalk and ASE noise. Figure 4.10 depicts the received constellations for the duty-cycles of the selected signal considered in Figure 4.9. In each case, the received signal has a QPSK interferer having the crosstalk level that leads to a 1 dB OSNR penalty. Additionally, the ideal symbol amplitudes for the QPSK modulation format are represented with a red circle. The averages of the symbol amplitudes of the received signal are also marked with a orange square. From Figure 4.10, it can be seen that the locations of the averages symbols amplitudes at the constellation of the QPSK NRZ selected signal (Figure 4.10(a)) and QPSK RZ66 selected signal (Figure 4.10(b)) are practically the same as the ones obtained for the ideal constellation. Therefore, in this situation, the EVM assessment of the receiver performance is in agreement with the one predicted by the DEC, as observed in Figures 4.9(a) and 4.9(b). Regarding the received constellation of the QPSK RZ33 selected signal, depicted in Figure 4.10(d), the locations of the averages symbols amplitudes are clearly mismatched from the ideal ones, and leads to discrepancies between the EVM and DEC estimations observed in Figure 4.9(d). For the QPSK RZ50 selected signal, Figure 4.10(c) shows that the received constellation is slight different from the ideal constellation, and leads to the differences between the EVM and DEC estimations observed in Figure 4.9(c).

Additionally, the PDFs for the QPSK RZ33 selected signal in presence of a QPSK RZ33, 16-QAM RZ33 and 64-QAM RZ33 interferers having the crosstalk levels that leads to 1 dB OSNR degradation were obtained and are depicted in Figure 4.11. The dashed lines are the PDFs obtained analytically, considering a Gaussian distribution, with mean and variance of the received signal were estimated using the MC simulator. Figure 4.11 also indicates the ideal amplitudes of the QPSK modulation format by a black line and the mean of each PDF is highlighted with a black dashed line. As it can be observed, there is a normalized difference of approximately 0.25 between the ideal amplitudes and the mean of the PDFs, and so the symbols distribution is clearly misplaced in relation with the ideal locations of the decision variable of the QPSK modulation format. However, the simulated PDFs agree with the theoretical PDFs, revealing that, in presence of in-band crosstalk, the PDFs still follow a Gaussian distribution for 1 dB OSNR penalty.

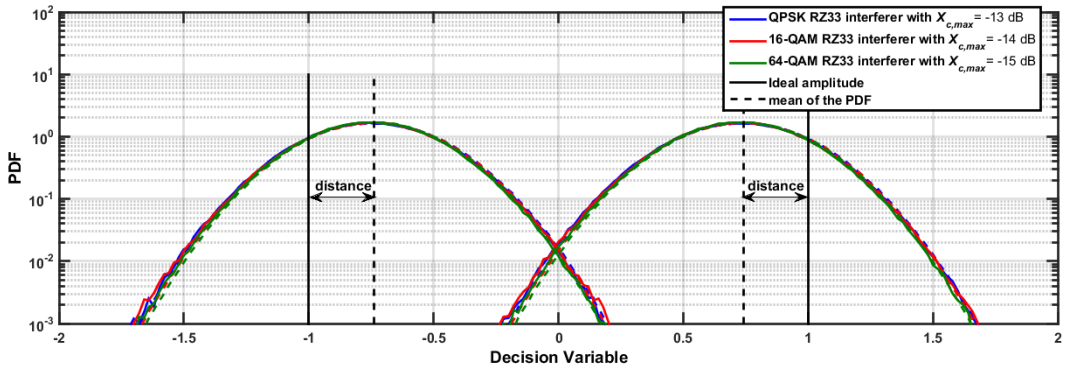

Figure 4.11: PDFs of the QPSK RZ33 selected signal having an OSNR of 11.2 dB, with QPSK RZ33, 16-QAM RZ33 and 64-QAM RZ33 interfering signals having a $X_{c,max}$ of -13 dB, -14 dB and -15 dB, respectively.

Table 4.2: Simulation parameters used for the study of the time misalignment influence in the OSNR degradation due to the crosstalk.

Parameter	value
Selected signal	QPSK
Assessment method	DEC
OSNR	see Table 4.1
Time mismatch variation	$[0,T_s]$
Phase noise ϕ_ε	0

4.4.1.1 Time Misalignment

In this subsection, the time misalignment influence on the OSNR degradation of the coherent receiver due to in-band crosstalk is studied. The parameters used in this simulation are indicated in Table 4.2. Figure 4.12 depicts the OSNR degradation as a function of the time misalignment between the interfering signal and the selected signal. From inspection of Figure 4.12, it can be noticed that a null or a T_s time misalignment leads to the highest OSNR degradation when the modulation format of the interferer is the QPSK. This situation leads to the alignment of the peak amplitude of the crosstalk signal with the sampling time instant of the selected signal. Hence, the QPSK receiver detects the selected signal with the interfering signal at its maximum amplitude. This conclusion is in agreement with the results found in [20]. Figure 4.12 shows also that, for the QPSK interferer, the time misalignment that leads to the smallest OSNR degradation is $T_s/2$, which corresponds to the required time mismatch for the symbol transition of the interfering signal to be aligned with the sampling time instant of the selected signal, and consequently, the interference caused by the crosstalk signal is practically null at the decision circuit input.

Figure 4.12 shows also that the time misalignment is less detrimental to the performance of the receiver when the interferers have 16-QAM and 64-QAM modulation formats and considering the NRZ pulse shape, as it can be noticed in Figure 4.12(a). This conclusion can be explained by the longer duration of the symbol period of the interfering signals in comparison with the original signal symbol duration. Only for smaller duty-cycles, 50% and 33%, the 16-QAM and 64-QAM interfering signals lead to a non-negligible variation of the OSNR penalty with the time misalignment, which for the 16-QAM RZ33 interfering signal reaches values comparable to the QPSK RZ33 crosstalk signal.

In addition, and in agreement with Figure 4.9, Figure 4.12 allows also to conclude that the reduction of the selected signal duty-cycle increases the crosstalk tolerance. By reducing the symbol period of the selected signal, in the presence of the time misalignment, the crosstalk influence on the sampling time instant of the selected signal becomes negligible, as shown schematically in Figure 4.13 for the 16-QAM RZ33 interfering

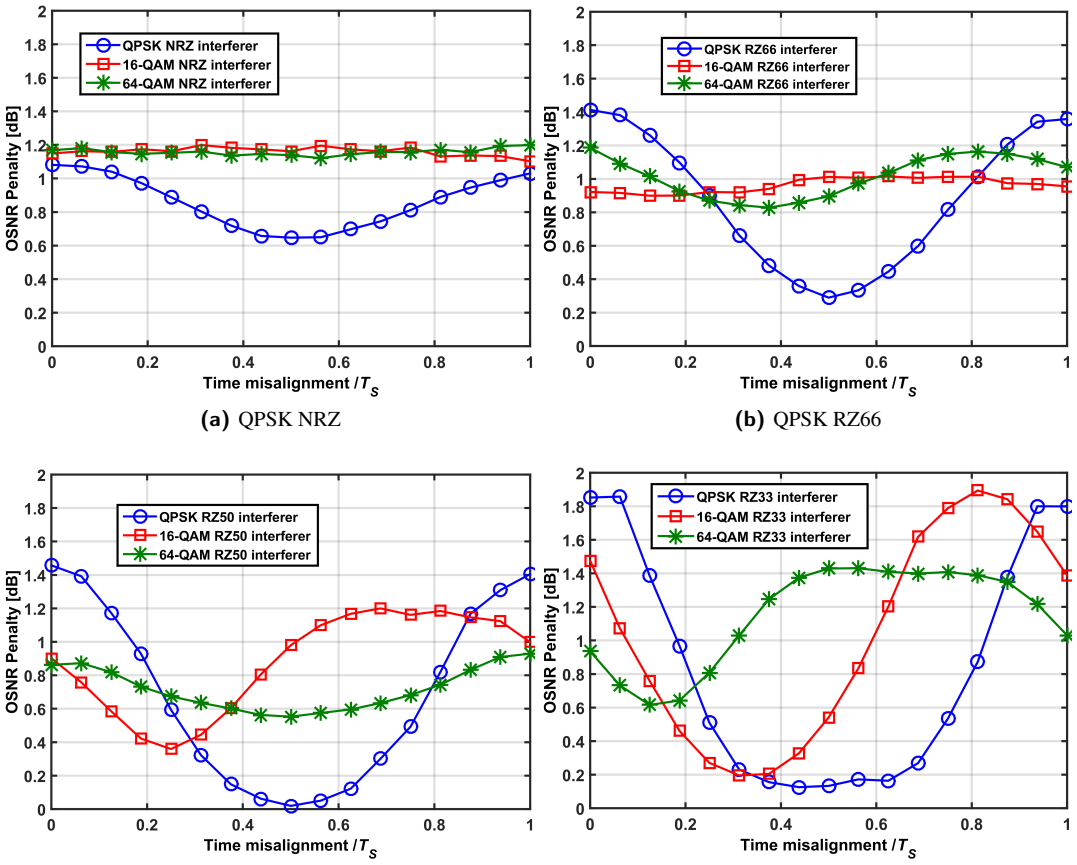

(a) QPSK NRZ **(b)** QPSK RZ66

(c) QPSK RZ50 **(d)** QPSK RZ33

Figure 4.12: Time misalignment influence due to a single interferer signal with different modulation formats and the same pulse shape as the (a) QPSK NRZ, (b) QPSK RZ66 (c) QPSK RZ50 and (d) QPSK RZ33 selected signal pulse shape.

signal. Figure 4.13 shows that the $T_s/3$ time mismatch aligns the interfering pulse with the return-to-zero period of the original signal, and therefore, the interference in this case is negligible.

As a final note, we have observed that the variation of the OSNR penalty with the time misalignment has a period of T_s, even for interfering signals with a symbol duration longer than the symbol period of the selected

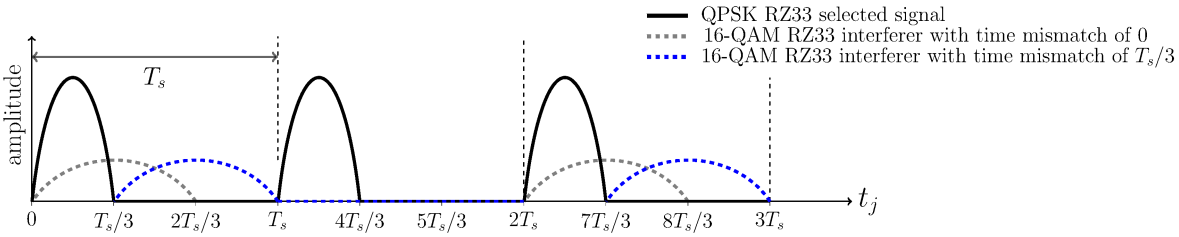

Figure 4.13: Schematics of the interference of 16-QAM RZ33 pulse shape on the QPSK RZ33 selected signal, for a time mismatch of 0 and $T_s/3$.

Table 4.3: Simulation parameters to study the phase noise influence in the OSNR degradation due to the crosstalk.

Parameter	value
Selected signal	QPSK
Assessment method	DEC
OSNR	see Table 4.1
Time misalignment	worst case of Figure 4.12
Phase noise variation ϕ_ε	$[0,\pi]$ rad

signal, such as the 64-QAM modulation format.

4.4.1.2 Phase Difference

The phase noise influence on the receiver performance degradation in the presence of in-band crosstalk is studied in this subsection, using the parameters presented in Table 4.3. The time misalignment is set, by using the results depicted in Figure 4.12, to the worst case time mismatch, accordingly to the selected and crosstalk signals

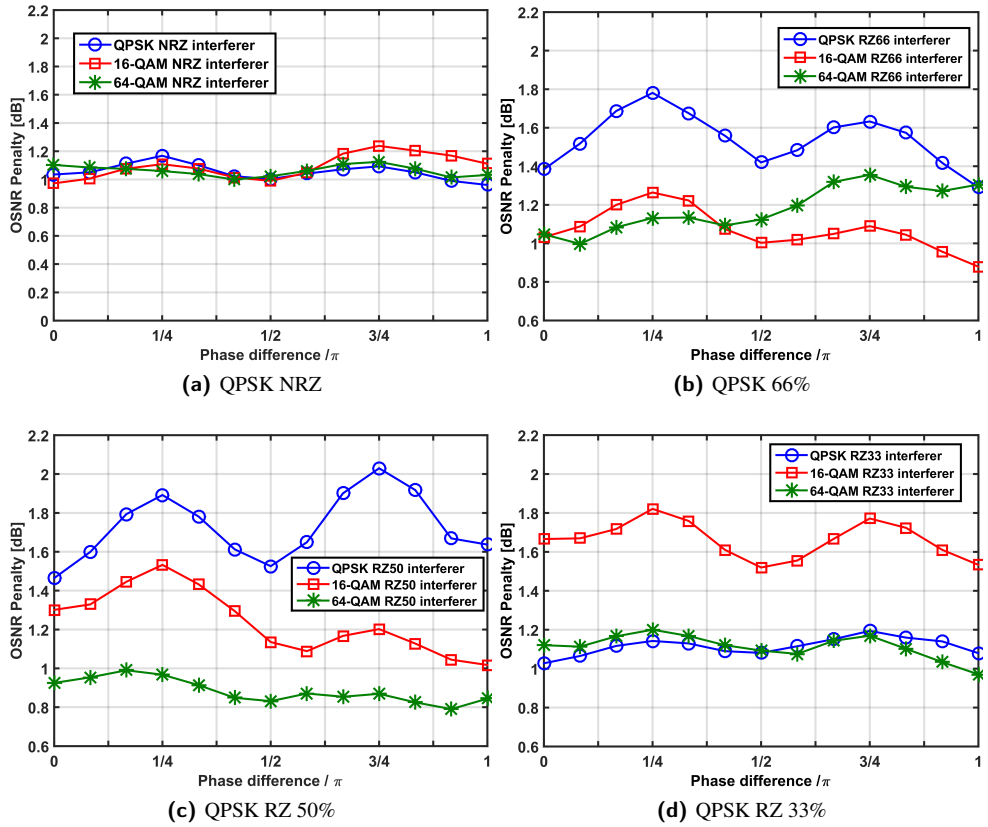

(a) QPSK NRZ **(b)** QPSK 66%

(c) QPSK RZ 50% **(d)** QPSK RZ 33%

Figure 4.14: OSNR penalty as a function of the normalized phase difference for a single interferer with the same or higher modulation format order than the (a) QPSK NRZ, (b) QPSK RZ66 (c) QPSK RZ50 and (d) QPSK RZ33 selected optical signals and having the same pulse shape as the original signal.

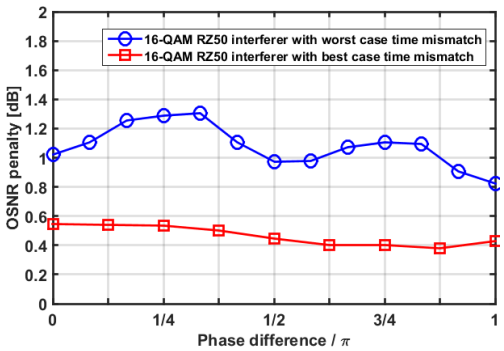

Figure 4.15: OSNR penalty as a function of the normalized phase difference between a 16-QAM RZ33 interfering signal and a QPSK RZ33 selected signal.

considered in each simulation.

Figure 4.14 depicts the OSNR penalty as a function of the phase difference for interfering signals with the same pulse shape as the original signal. Figure 4.14 shows that the phase noises of $\pi/4$ and $3\pi/4$ radians are the angles that lead to the higher OSNR degradation in all the pulse shapes studied and this is in agreement with the results found in [20] and [46]. However, the OSNR degradation due to the phase difference variation does not significantly contribute to the OSNR penalty variation. The major OSNR penalty enhancement is noticed in Figure 4.14(c), where the OSNR penalty variation with the phase difference reaches approximately 0.6 dB. Figure 4.15 shows the comparison between the OSNR penalty caused by a 16-QAM RZ50 interfering signal with its worst and with its best case time mismatch, i.e. the time mismatch that leads to the lowest OSNR degradation. Figure 4.15 shows that the influence of the phase noise on the OSNR penalty variation, although not much significant, is enhanced when the worst time misalignment case occurs. The same comparison and similar conclusions have been drawn for different selected and interfering signals.

We have observed that the influence of the phase noise on the interfering signal leads to a rotation of its constellation. Assuming a phase error of $\pi/4$ radians in a QPSK crosstalk signal, its constellation without

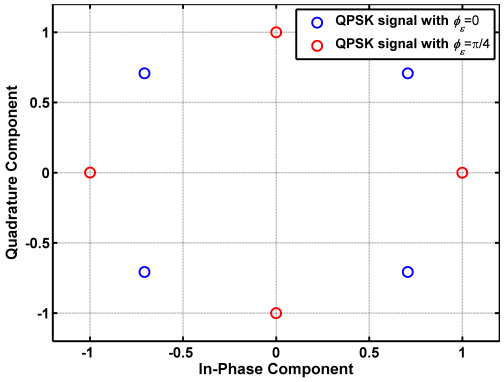

Figure 4.16: QPSK interfering signal constellation having a phase noise of 0 and $\pi/4$ radians.

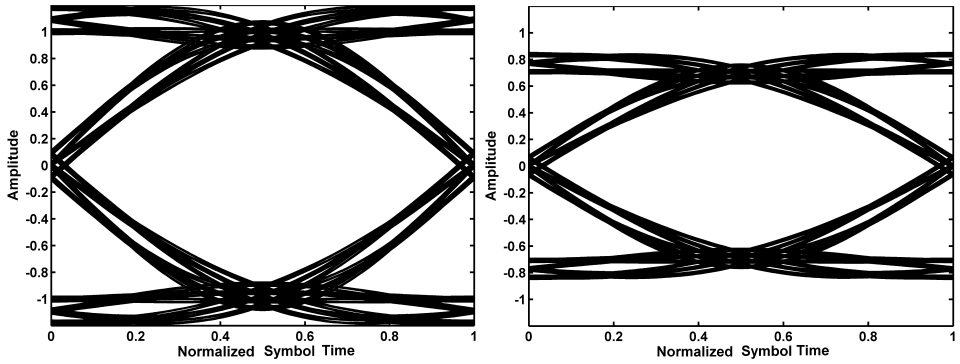

(a) $\phi_\varepsilon = \pi/4$ rad **(b)** $\phi_\varepsilon = 0$ rad

Figure 4.17: Eye diagrams of the QPSK interfering signal with a phase noise of (a) $\pi/4$ and (b) 0 radians.

ASE noise is depicted in Figure 4.16, where it is clear that a $\pi/4$ phase rotation increases the amplitude of the I and Q components of the interfering signal and, hence, leads to a maximum interference on the selected signal [46]. Figure 4.17(a) depicts the eye diagrams of the interfering signal with a phase noise of $\pi/4$ which has higher amplitude levels comparing with the eye diagram illustrated in Figure 4.17(b) obtained for a null phase difference.

4.4.2 Same Modulation Format and Different Duty-Cycles

In this section, the impact of the variation of the interfering signal duty-cycle on the receiver performance degradation due to in-band crosstalk is assessed. It is considered that the interfering signal has the same modulation format as the selected signal.

The DEC and EVM estimations, for the QPSK selected signal having a QPSK single interferer, as a function of the crosstalk level are shown, respectively, in the left-hand side and the right-hand side of Figure 4.18.

Starting with the inspection of the DEC estimates of the OSNR penalty, it can be concluded that the reduction of the crosstalk signal duty-cycle leads to a lower OSNR degradation. The most clear example is noticed in the left-hand side of Figure 4.18(a), which depicts the DEC estimation for the QPSK NRZ pulse shape. The predicted $X_{c,max}$ for the QPSK NRZ interfering signal is almost 5 dB less than the estimated $X_{c,max}$ for the QPSK RZ33 crosstalk signal. Considering the QPSK RZ33 selected signal, shown in the left-hand side of Figure 4.18(d), the DEC estimates that all interfering pulse shapes lead to practically the same OSNR degradation on the QPSK RZ33 receiver performance.

Comparing the EVM and DEC estimations for the maximum crosstalk level for a 1 dB OSNR degradation and considering the NRZ, RZ66 and RZ50 selected signals (Figure 4.18(a) to 4.18(c)), a good agreement is noticed, between both methods (below about 1 dB). In Figure 4.18(d), which depicts the OSNR penalty as a function of the crosstalk level for the QPSK RZ33 signal, the DEC $X_{c,max}$ prediction for the QPSK NRZ, RZ66

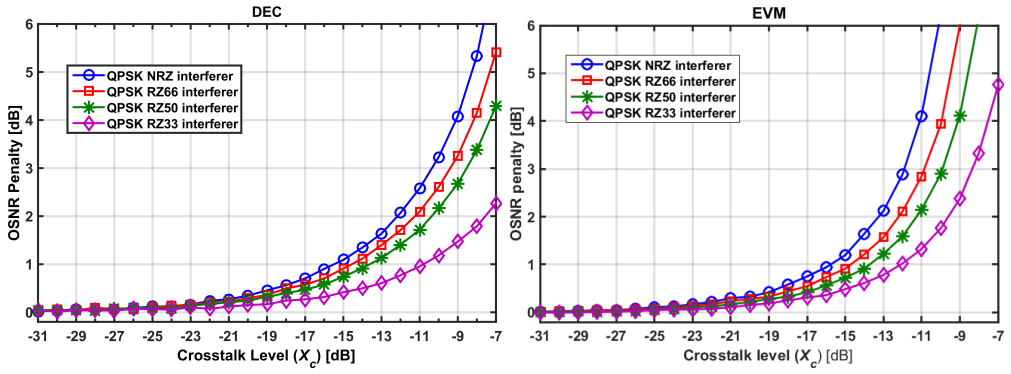

(a) QPSK NRZ

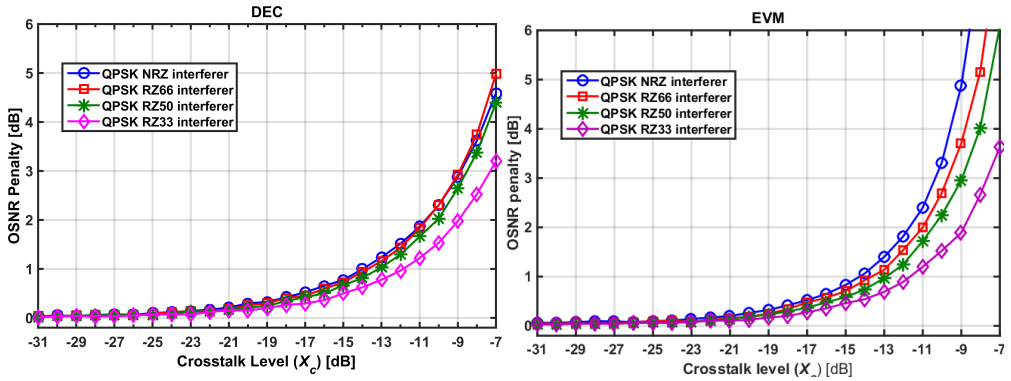

(b) QPSK RZ66

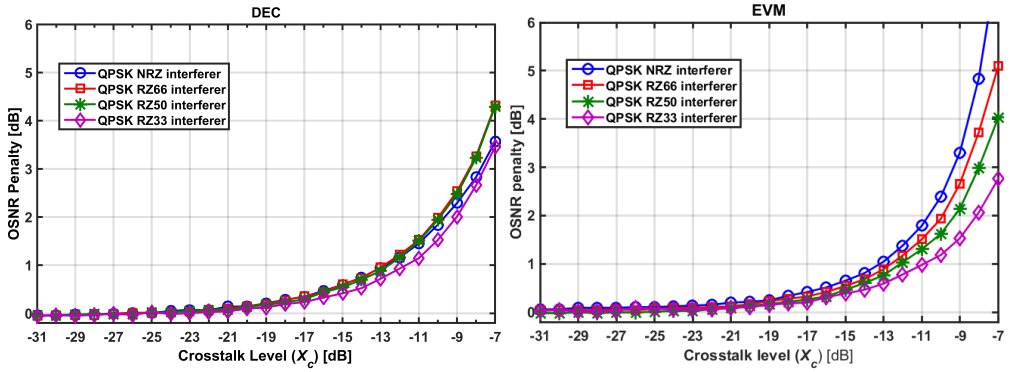

(c) QPSK RZ50

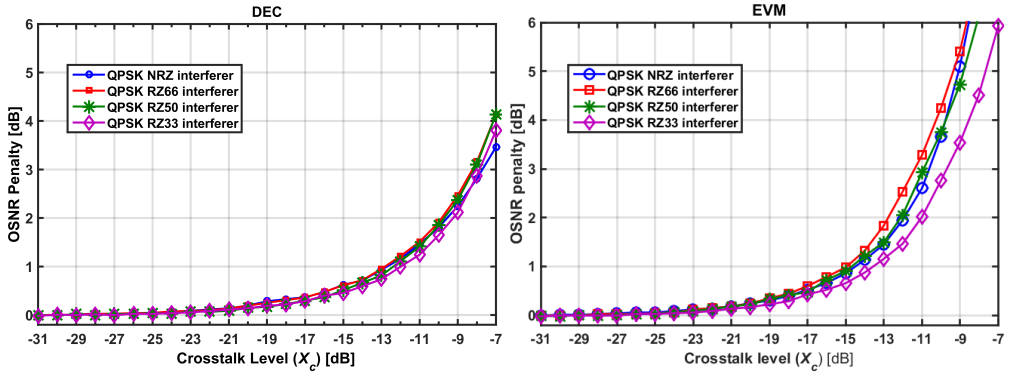

(d) QPSK RZ33

Figure 4.18: OSNR penalty due to interfering signals with different duty-cycles but having the same modulation format as the (a) QPSK NRZ, (b) QPSK RZ66 (c) QPSK RZ50 and (d) QPSK RZ33 selected optical signal.

and RZ50 interfering signals are −13 dB, while the EVM estimates a crosstalk level of −15 dB for the same interferers. In section 4.4.1, it was also observed a discrepancy between the OSNR penalty assessment obtained using both methods for the QPSK RZ33 selected signal, and in this case, it was attributed to the difference between the ideal and the received constellation symbols amplitudes. Regarding to the OSNR penalty due to higher crosstalk levels, the EVM estimates differ substantially from the DEC predictions, as observed also in Figure 4.9.

4.4.2.1 Time Misalignment

In this section, the study of the time misalignment of a single interferer, having the same modulation format and bit rate than the selected signal and with different duty-cycles is presented.

Figure 4.19 shows the OSNR penalty as a function of the normalized time misalignment, using the DEC method. Figure 4.19 shows that the time misalignment has a relevant influence on the OSNR degradation variation, particularly when the interfering pulse shape is not NRZ. The worst case time mismatch can lead to OSNR

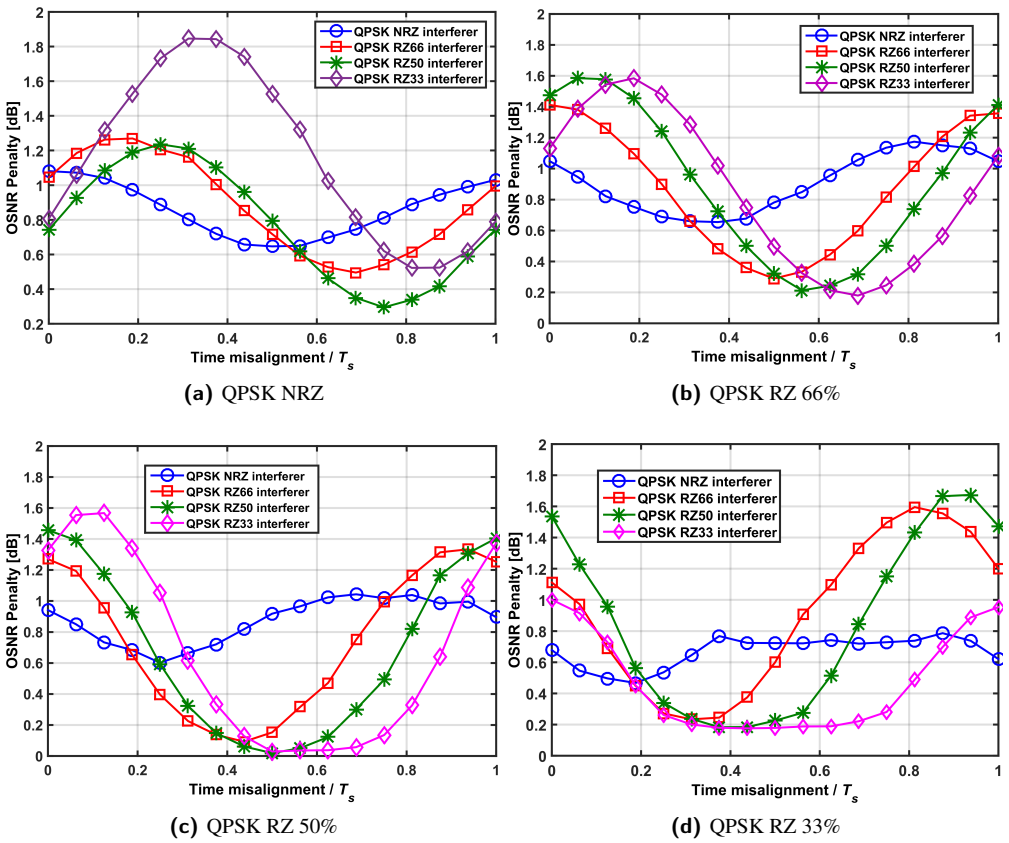

(a) QPSK NRZ **(b)** QPSK RZ 66%

(c) QPSK RZ 50% **(d)** QPSK RZ 33%

Figure 4.19: Time misalignment influence on the OSNR penalty due to a single interferer with different duty-cycles and having the same modulation format as the (a) QPSK NRZ, (b) QPSK RZ66 (c) QPSK RZ50 and (d) QPSK RZ33 selected optical signal.

penalty variations that reach almost 1.6 dB, as can be observed in Figure 4.19(b) to 4.19(d). In Figure 4.19, it can be seen also that negligible OSNR degradations are obtained for a longer duration (within T_s) of the time misalignment, when the interfering signal duty-cycle is reduced. An example is noticed in Figure 4.19(c), where the lowest OSNR degradation due to interfering signals with RZ66, RZ50 and RZ33 duty-cycles is below 0.1 dB.

Figure 4.20 depicts schematically the interference between a QPSK RZ50 selected signal and QPSK NRZ and QPSK RZ50 interfering signals for a $T_s/2$ time mismatch. The QPSK RZ50 interfering pulse is overlapped to the return-to-zero period of the selected signal and consequently, the OSNR degradation is minimized, as shown in Figure 4.19(c). In contrast, independently of the time misalignment variation, the QPSK NRZ interfering pulse always interferes with the sampling time instant of the original signal. This fact justifies the small variation on the OSNR degradation noticed in Figure 4.19, concerning the interference of signals with NRZ pulse shape.

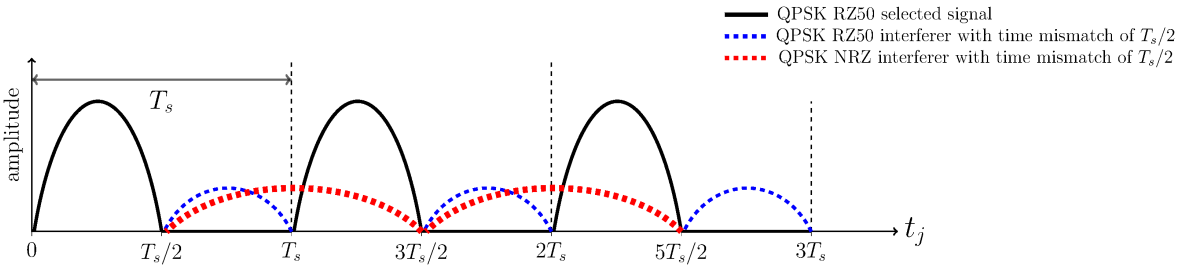

Figure 4.20: Schematics of the interference of QPSK NRZ and RZ50 pulse shapes on the QPSK RZ50 selected signal, for a time mismatch of $T_s/2$.

4.4.2.2 Phase Difference

The study of the phase noise impact on the receiver performance due to the duty-cycle variation of the interfering signal is also performed in this subsection, and its results are depicted in Figure 4.21. For each QPSK original signal, the time misalignment is parametrized using the worst time mismatch found in Figure 4.19.

From Figure 4.21, it is clear that the phase differences that lead to the highest OSNR penalty are $\pi/4$ and $3\pi/4$ radians. These results are expected since the duty-cycle variation does not change the symbols location on the interfering signal constellation. Therefore, the worst case phase noises are the sames as the ones found in section 4.4.1.2.

Once again, it can be also concluded that the phase noise impairment is not relevant to the OSNR degradation variation, since the maximum OSNR penalty variation found in Figure 4.21 is approximately only 0.5 dB in the several simulated scenarios. It was also observed that the influence of the phase noise on the OSNR penalty due to interfering signals having the time mismatch that leads to the smallest OSNR penalty does not lead to a significant OSNR degradation.

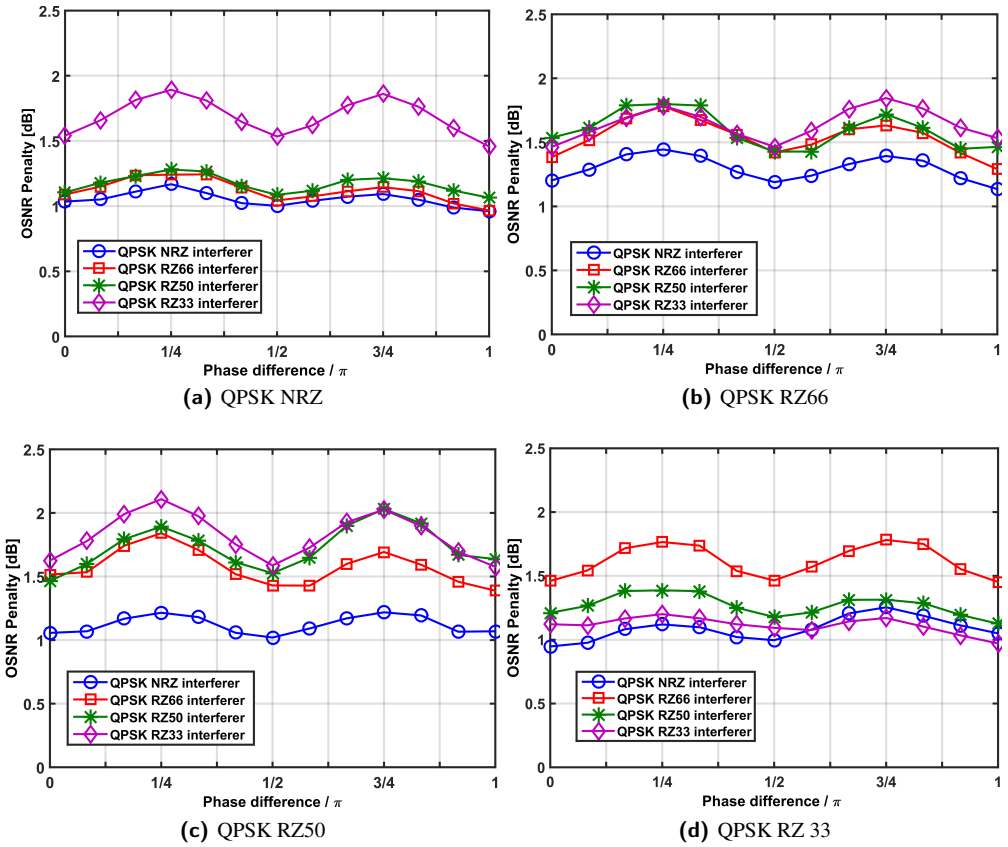

(a) QPSK NRZ **(b)** QPSK RZ66

(c) QPSK RZ50 **(d)** QPSK RZ 33

Figure 4.21: OSNR penalty as a function of the normalized phase difference for a single interferer with different duty-cycles and with the same modulation format order as the (a) QPSK NRZ, (b) QPSK RZ66 (c) QPSK RZ50 and (d) QPSK RZ33 selected optical signal.

4.4.3 Mixed Modulation Formats and Different Bit Rates

In this section, the crosstalk impact on the receiver performance is studied, considering the interference of optical signals with different bit rates than the QPSK NRZ 50 Gbps selected signal. Four modulation formats are chosen for the interfering signals: OOK modulation format with NRZ pulse shape at a bit rate of 10 Gbps and 40 Gbps, for being the most commonly used modulation formats in optical networks, QPSK NRZ and the 16-QAM NRZ interfering signals, both with a bit rate of 400 Gbps. The QPSK and the 16-QAM optical signals were chosen to analyze the crosstalk impact on the performance of a PDM-QPSK receiver in future optical networks scenarios, as the bit rate of 400 Gbps has been indicated as the capacity of the next generation optical networks [2]. The OOK modulation format signal with a bit rate of 10 Gbps or 40 Gbps is assumed to be transmitted in a single polarization and with an ideal extinction ratio. A QPSK or a 16-QAM signal with 400 Gbps can be multiplexed in polarization, so, in each polarization, an optical signal with 200 Gbps is considered.

The OSNR penalty as a function of the crosstalk level due to the presence of interfering signals with

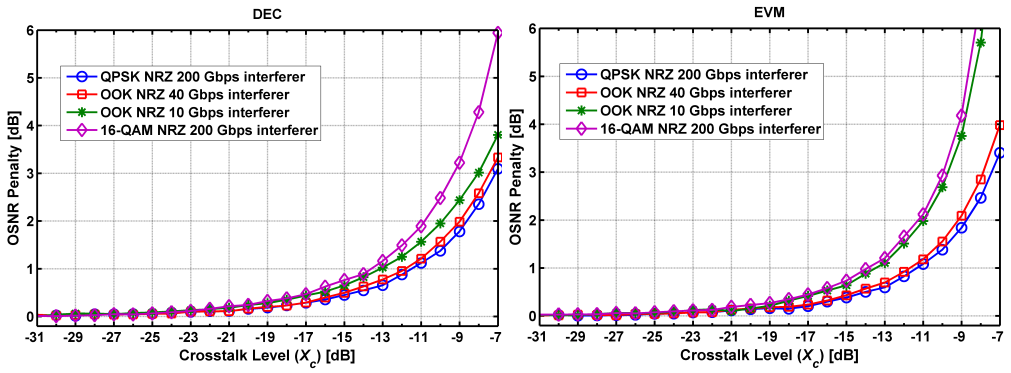

(a) DEC **(b)** EVM

Figure 4.22: OSNR penalty as a function of the crosstalk level due to interfering NRZ signals with different binary rates and modulation formats than the QPSK NRZ selected optical signal, estimated by the (a) DEC method and the (b) EVM method.

mixed modulation formats estimated using the DEC and EVM methods is shown in Figure 4.22. According to the DEC estimation of the $X_{c,max}$, depicted in Figure 4.22(a), the interfering signals that lead to the lowest OSNR degradation are the QPSK NRZ 200 Gbps and the OOK NRZ 40 Gbps, both with $X_{c,max} \approx -12$ dB. The most detrimental interfering signals to the coherent receiver performance, are the OOK NRZ 10 Gbps and the 16-QAM NRZ 200 Gbps, both with a crosstalk level of about -14 dB, for a 1 dB OSNR penalty. However, considering $X_c = -7$ dB, the 16-QAM NRZ interferer leads to a OSNR penalty 2 dB higher than the one obtained due to the interference of the OOK 10 Gbps crosstalk signal.

Figure 4.22(b) shows the EVM assessment of the OSNR penalty due to the crosstalk interference with different bit rates and modulation formats. Using the EVM method, the $X_{c,max}$ estimations are nearly the same as the ones found using the DEC method, confirming the good agreement between both methods also found in Figures 4.9(a) and 4.18(a). For higher crosstalk levels, we observed again, that the estimations of both methods disagree.

The impact of time misalignment and phase noise impairments on the receiver performance is also evaluated. The corresponding results are depicted in Figure 4.23. From Figure 4.23(a), it is noticed that the time misalignment has practically no influence on the OSNR degradation. The same conclusions were drawn from Figure 4.12(a), concerning the 16-QAM and 64-QAM NRZ interfering signals.

The phase noise study results are depicted in Figure 4.23(b), where $\pi/4$ and $3\pi/4$ are the phase differences that lead to the highest OSNR degradation due to the interference of the QPSK NRZ and 16-QAM NRZ with bit rate of 200 Gbps. The reasons are the same as the ones already described in section 4.4.2.2. By considering the OOK interfering signal, the angles that lead to the highest OSNR degradation are 0, $\pi/2$, and π radians. We observed once again, that the phase noise does not lead to a significant OSNR penalty variation, as the highest OSNR penalty is only 0.2 dB higher than the lowest OSNR degradation.

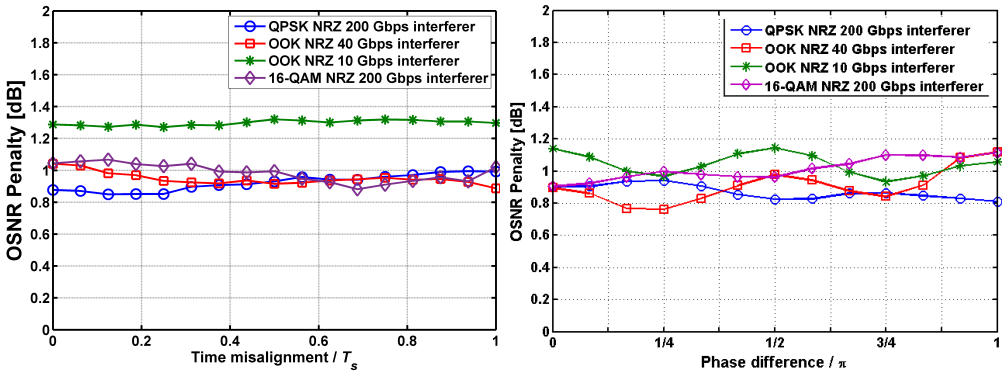

(a) Time misalignment **(b)** Phase noise

Figure 4.23: OSNR penalty due to interfering NRZ signals with different binary rates and modulation formats than the QPSK NRZ selected optical signal as a function of the (a) time misalignment and the (b) phase difference.

4.5 16-QAM Receiver Performance in Presence of In-band Crosstalk

Table 4.4: Required OSNR for the 16-QAM receiver for a BER of 10^{-3} per pulse shape and per estimation method, using the indicated -3 dB bandwidth of the EF and the OF.

Format modulation	Pulse shape	OSNR [dB]		EF[3] [$/R_s$]		OF[4] [$/R_s$]	
		DEC	EVM	DEC	EVM	DEC	EVM
16-QAM at 50 Gbps (per polarization)	NRZ	15	15.1	1.6		1.1	
	RZ66	14.2	14.3			2	
	RZ50	14.2	14.3			2.7	
	RZ33	14.4	14.1			4.7	

In this section, the impact of in-band crosstalk on the receiver performance is investigated for a 16-QAM selected signal with a bit rate of 50 Gbps per polarization. The goal is to estimate the crosstalk level that leads to a 1 dB OSNR penalty, considering M-QAM interfering signals with $M = 4$, 16, 64, and with the same bit rate as the selected signal. The accuracy of the EVM method is also assessed by comparison with the DEC method.

Table 4.4 presents the required OSNRs to get the BER of 10^{-3} for a 16-QAM coherent receiver without crosstalk, estimated using the DEC and EVM methods. The DEC OSNR estimates for the 16-QAM NRZ receiver is almost 1.7 dB higher than the OSNR obtained theoretically using Equation (2.39). The same difference between the DEC and the theoretical OSNR estimation for the 16-QAM NRZ coherent receiver is found in [20]. The OSNRs estimated in the absence of in-band crosstalk using the EVM method are practically the same as the ones obtained from the DEC method. Comparing with the estimated OSNRs without crosstalk, presented in Table 4.1, the DEC estimates are approximately 5 dB higher than the ones obtained for the QPSK coherent receiver. In Table 4.4, the EF and OF -3 dB bandwidths used in this study are also presented and its values are taken from the filters optimization performed in section 3.6.

[3] 5^{th}-order Bessel filter
[4] 4^{th}-order Super-Gaussian filter

Figure 4.24 depicts the DEC (left-hand side) and the EVM (right-hand side) estimations of the OSNR penalty as a function of the crosstalk level due to interfering signals with equal or different modulation format orders, but with the same duty-cycle as the 16-QAM selected signal.

The left-hand side of Figure 4.24 shows that, considering the DEC method, the QPSK interferer is significantly less detrimental than the 16-QAM or the 64-QAM interferer, since the crosstalk level for 1 dB OSNR degradation for a QPSK interfering signal is approximately 3 dB higher than the $X_{c,max}$ for a 16-QAM interferer. We observed again that, as the selected signal and the crosstalk signal duty-cycles are reduced, the influence of the in-band crosstalk on the coherent receiver performance degradation is diminished. In the left-hand side of Figure 4.24(d), it can be seen that, considering the 16-QAM RZ33 selected signal and accordingly to the DEC estimation, the crosstalk levels that lead to 1 dB OSNR penalty are above 4 dB in comparison with the ones estimated for the 16-QAM NRZ receiver, shown in Figure 4.24(a)).

Additionally, the OSNR degradation due to the interference of a 64-QAM crosstalk signal is not significantly higher than the one caused by the 16-QAM interferer. In the left-hand side of Figure 4.24, it can be observed that, the DEC estimations for the $X_{c,max}$ for the 16-QAM and for the 64-QAM interfering signals have a maximum difference of 1 dB between them.

Regarding the right-hand side of Figure 4.24, the EVM estimations of the crosstalk level that leads to a 1 dB OSNR degradation due to the 16-QAM and 64-QAM interfering signals are in agreement with the DEC estimations, except in the RZ33 pulse shape. Figure 4.24(d) shows that the $X_{c,max}$ predicted by the DEC method are more than 1 dB lower than the ones obtained from the EVM method for all the interfering signals. For instance, the DEC predicts a $X_{c,max}$ of -19 dB for the 16-QAM RZ33 interfering signal, while, for the same interferer, the EVM estimates a $X_{c,max}$ of -17 dB. Finally, the OSNR degradation due to interfering signals estimated by the EVM method becomes much different from the DEC estimations for higher crosstalk levels.

In order to explain the discrepancy between the EVM and the DEC estimations of the $X_{c,max}$ for the 16-QAM RZ33 receiver, observed in Figure 4.24(d), the received constellation of the 16-QAM RZ33 selected signal having a OSNR of 14.4 dB and a 16-QAM RZ33 interfering signal with a crosstalk level of -19 dB is depicted in Figure 4.25. Additionally, the ideal symbols amplitudes for the QPSK modulation format are represented with a red circle. The averages of the symbols amplitudes of the received signal are also marked with a orange square. Analyzing this figure, it can be observed that for the symbols that have the ideal amplitudes of ± 3 in the I and Q component, the averages of the received symbols amplitudes are mismatched with the ideal ones. Therefore, in this situation, as seen also for the 4-QAM, the EVM estimations become inaccurate. Additionally, the PDFs of the decision variable for the 16-QAM RZ33 selected signal were obtained for the OSNR of 14.4 dB and the crosstalk levels of -16 dB,-19 dB and -20 dB for the QPSK RZ33, 16-QAM RZ33 and 64-QAM RZ33 interferers, respectively, are depicted in Figure 4.26. The theoretical PDFs were also obtained and depicted with a dashed line in Figure 4.26, considering a Gaussian distribution, which mean and variance of the received

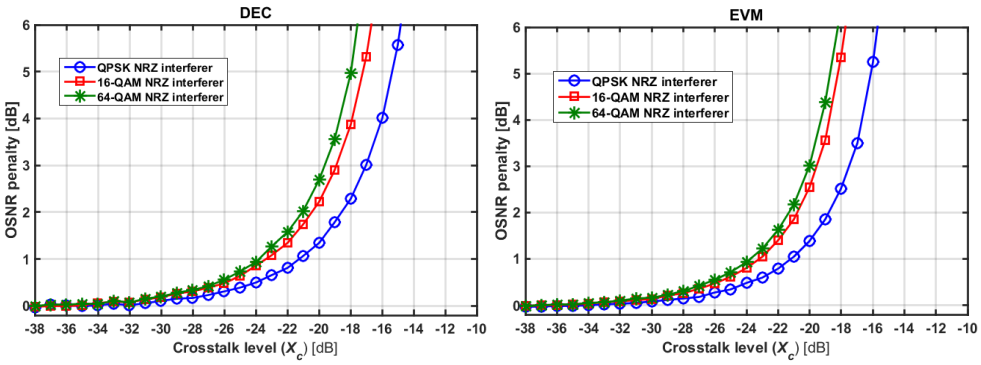

(a) 16-QAM NRZ

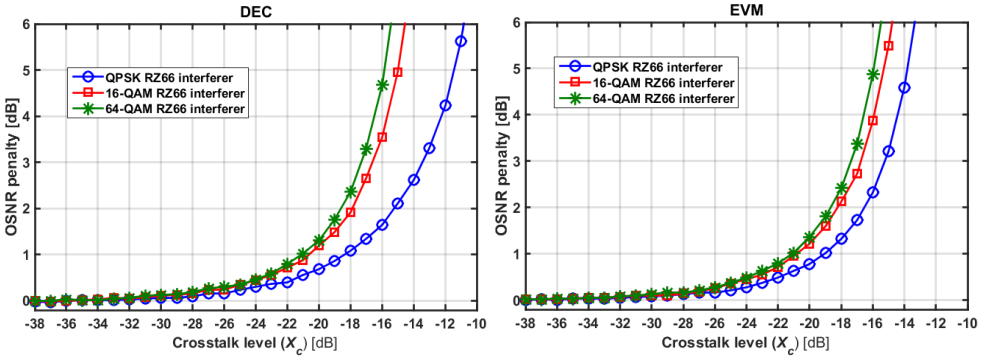

(b) 16-QAM RZ66

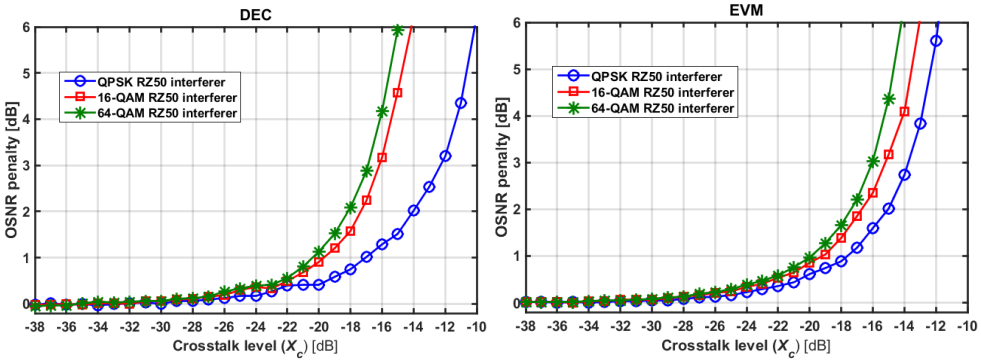

(c) 16-QAM RZ50

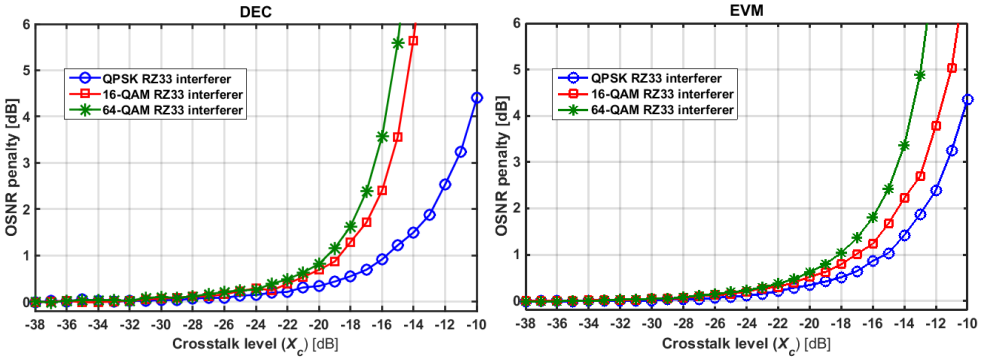

(d) 16-QAM RZ33

Figure 4.24: OSNR penalty as a function of the crosstalk level due to interfering signals with different modulation formats but having the same pulse shape as the (a) 16-QAM NRZ, (b) 16-QAM RZ66 (c) 16-QAM RZ50 and (d) 16-QAM RZ33 selected optical signal.

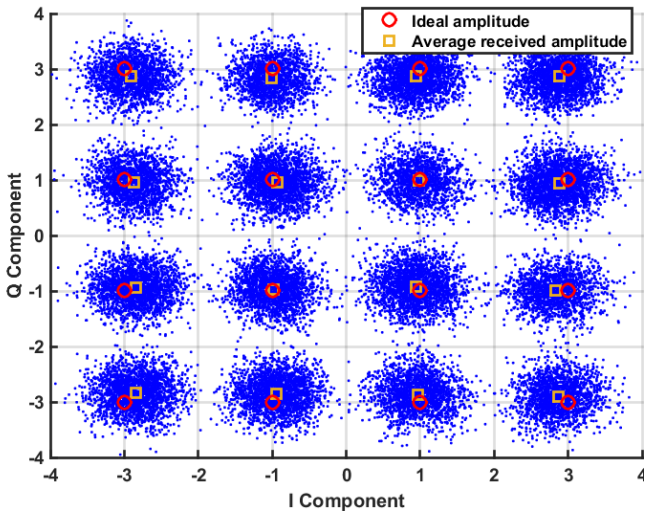

Figure 4.25: Received constellations of the 16-QAM RZ33 selected signal with a OSNR of 14.4 dB and a 16-QAM RZ33 interfering signal having the crosstalk level of -19 dB.

signal were estimated by the MC simulator. The mean of each PDF is drawn with a dashed black vertical line and the ideal amplitudes are highlighted with a black vertical line. The PDFs of the decision variable overlap the analytical PDFs, therefore still following a Gaussian distribution. However, as expected from the analysis of Figure 4.25, the mean of each PDF is mismatched from the ideal mean, especially for the amplitudes of -3 and 3. These misplacements are caused by the -3 dB bandwidth of the EF, which is too narrow for the 33% duty-cycle signal, leading to an amplitude signal reduction, therefore contributing to the reduction of the EVM accuracy.

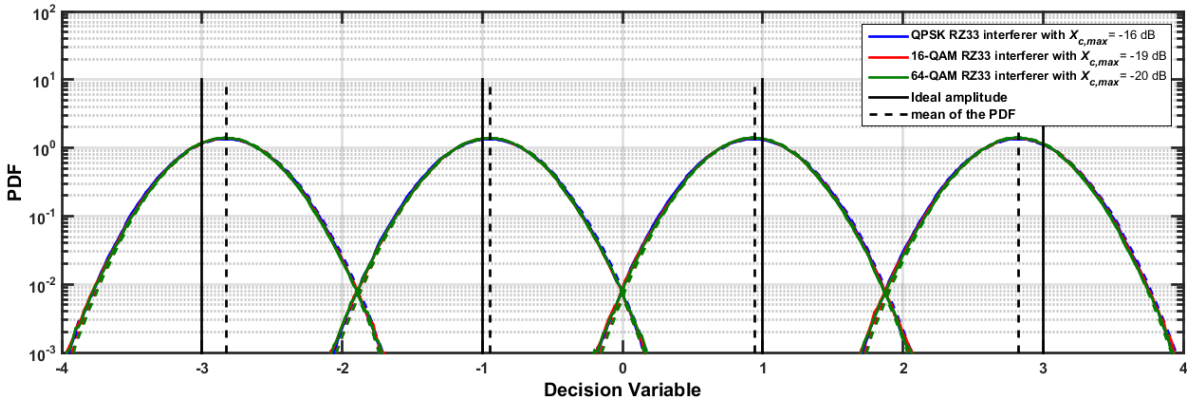

Figure 4.26: PDFs of the 16-QAM RZ33 selected signal with a OSNR of 14.4 dB and in the presence of a QPSK RZ33, 16-QAM RZ33 and 64-QAM RZ33 interfering signals having the corresponding $X_{c,max}$.

4.6 Conclusions

In this chapter, the crosstalk model used for the MC simulator was described in detail and its validation was performed by comparison with the results presented in [20], and an excellent agreement was noticed.

The OSNR degradation of a QPSK receiver due to the in-band crosstalk signals with different duty-cycles, modulation formats and bit rates, was assessed using the DEC and EVM methods. The comparison of the methods estimations was performed and analyzed. Considering a crosstalk level that leads to a 1 dB OSNR penalty (in relation to the absence of crosstalk), in QPSK and 16-QAM coherent receivers, both methods agreed in their estimations. A slight discrepancy was noticed when the selected signal duty-cycle was reduced. This discrepancy between both methods was attributed mainly to the deviation of the symbols locations on the receiver constellation in relation with the symbols locations on the transmitted constellation. However, our studies indicate that the EVM, although extremely inaccurate for higher crosstalk levels, is a satisfactory assessment tool to estimate the OSNR penalties due to in-band crosstalk around 1 dB.

The OSNR degradation assessment for QPSK and 16-QAM selected signals, using the DEC method led to the conclusion that the reduction of the duty-cycle of the selected signal increases the in-band crosstalk tolerance. Furthermore, the reduction of the duty-cycle of the interfering signal weakens its impact on the receiver performance. Our results show that the QPSK RZ33 selected signal was the most tolerant to in-band crosstalk and was also the less harmful interferer.

Additionally, and regarding QPSK coherent receivers, we have concluded that the OOK interfering signals lead to OSNR degradation due to in-band crosstalk smaller than QPSK. Regarding the M-QAM interferers at the bit rate of 200 Gbps per polarization, we observe again that increasing the modulation format order, enhances the influence of the in-band crosstalk in the OSNR degradation of the coherent receiver. Moreover, these interfering signals lead to the OSNR penalties similar to the ones obtained for the QPSK interfering signal at a bit rate of 50 Gbps per polarization. Therefore, the future deployment of the M-QAM modulation format (QPSK or 16-QAM) at a bit rate of 200 Gbps per polarization in future optical networks will not be significantly detrimental to the actual QPSK coherent receivers.

The influence of the time misalignment and the phase difference between interfering and selected signals was also analyzed. The time misalignment is less detrimental to the receiver performance when the crosstalk signal is a M-QAM signal with a higher order than the selected signal or an OOK signal. The study of the time misalignment impact on the receiver performance degradation due to the in-band crosstalk reinforced the advantages of the duty-cycle reduction.

The study of the phase noise influence on the coherent receiver performance led to the conclusion that this impairment does not contribute significantly to the OSNR degradation of the coherent receiver performance. However, we have concluded that the phase noise influence is related to the constellation rotation. Our results

have shown that the most detrimental phase errors, for the case of squared QAM constellations on the interfering signals, are the ones that shift the symbols locations to its maximum amplitudes values in the I component and Q components, i.e. $\pi/4$ and $3\pi/4$ radians.

Chapter 5

Conclusions and Future Work

In this chapter, the main conclusions of the work developed in this dissertation are presented, as well as suggestions for future work.

5.1 Final Conclusions

In this work, the performance of a M-QAM coherent receiver in presence of in-band crosstalk has been investigated.

Chapter 2 has described the coherent receiver detection technique and the mathematical analysis of the coherent detected signal in the presence of ASE noise. Additionally, the MC simulator developed to assess the performance of the coherent receiver was described. The evaluation methods used in this work to address the performance of the coherent receiver were also presented: the DEC and the EVM.

Chapter 3 was devoted to the coherent receiver performance validation in presence of ASE noise and the optical and electrical filters optimization using the DEC and EVM methods. The validation was performed by comparison of the BER estimated for the coherent receiver using the MC simulation with the theoretical BER obtained for QPSK, 16-QAM and 64-QAM modulation formats. We have seen that the BER estimations from the DEC and EVM overlapped the theoretical ones for larger filters bandwidths which do not introduce ISI on the received signal. However, with narrow OF -3 dB bandwidths ($B_o/R_s = 1$ or $B_o/R_s = 2$), discrepancies between the BERs were noticed due to the ISI introduced by the filters. It was also observed that as the modulation format order was increased, the OF bandwidth must be larger than for smaller orders to obtain DEC and EVM BER estimates in agreement with the theoretical curves.

Then, several non-ideal filters types and their respective bandwidths were optimized, using the DEC and

EVM methods, in order to obtain the best pair of optical and electrical filters that maximizes the performance of the coherent receiver in presence of ASE noise, for the QPSK and 16-QAM modulation formats with different pulse duty-cycles. The best filters combination, which minimizes the BER predicted by the DEC method, was the 5^{th}-order Bessel EF and the 4^{th}-order Super-Gaussian OF. For the QPSK coherent receiver, the EF -3 bandwidth is R_s, and the OF -3 dB bandwidth is $1.2R_s$, $2R_s$, $3R_s$ and $4R_s$ for the pulse duty-cycles of 100%, 66%, 50% and 33%, respectively. For the 16-QAM coherent receiver, the optimized EF -3 bandwidth is $1.6R_s$, and the OF -3 dB bandwidth is $1.2R_s$, $2.5R_s$, $3R_s$ and $4.7R_S$ for the pulse duty-cycles of 100%, 66%, 50% and 33%, respectively. These filters combination were achieved due to a compromise between ISI, with enhanced impact for narrow filters bandwidths, ASE noise, which filtered power was higher for larger filter bandwidths and signal pulse duty-cycles. It was also observed that the EVM is a good tool to estimate the optimum filters bandwidths for the coherent receiver, due to the agreement of its estimates with the DEC estimates. This behavior was observed for all filters combinations, signal duty-cycles and M-QAM modulation format orders. However, concerning the BER estimations the EVM accuracy was diminished, for narrow EF bandwidths, where ISI is more significant, and higher filter bandwidths, where ASE noise is dominant.

In chapter 4, the impact of in-band crosstalk on the QPSK and 16-QAM coherent receiver performance was studied. The MC simulation model was validated by comparison of its performance estimates with the results found in [20].

Then, the degradation of the coherent receiver performance due to in-band crosstalk was investigated. Our results have shown that the crosstalk impact is enhanced by increasing the interferer modulation format order. Additionally, the reduction of the selected signal duty-cycle enhances the crosstalk tolerance and, therefore, the QPSK RZ33 selected signal revealed to be the most resilient selected signal to in-band crosstalk. Furthermore, reducing the duty-cycle of the interfering signal leads to a smaller influence of crosstalk on the degradation of the coherent receiver performance. Hence, the QPSK RZ33 interferer was also the less detrimental interferer. The impact of in-band crosstalk on the 16-QAM coherent receiver performance in presence of a single interferer having different modulation format orders was also investigated and similar conclusions were drawn.

The analysis of the influence of the time misalignment and the phase error between the selected and crosstalk signals was investigated using the DEC method. It was concluded that the highest OSNR degradation occurs, for the most cases, when the temporal mismatch aligns the maximum amplitude of the crosstalk signal with the sampling time instant of the selected signal. Lastly, the phase noise influence on the crosstalk impact was also studied and led to the conclusion that it is related to the rotation of the constellation of the crosstalk signal. The most detrimental phase errors are the ones that shift the symbols locations to its maximum values in the I component or in the Q component. However, we have observed that this impairment has almost a negligible impact on the OSNR degradation of the coherent receiver.

Regarding the EVM assessments of the influence of in-band crosstalk on the performance degradation of

the QPSK coherent receiver, the crosstalk level that leads to a 1 dB OSNR degradation predicted by the EVM revealed to be in agreement with the DEC estimations, when considering higher duty-cycles (100% or 66%). For lower duty-cycles, discrepancies between both methods estimations were noticed. For instance, according to the DEC method, the crosstalk level for 1 dB OSNR degradation for the QPSK RZ33 interfering and selected signals is -12 dB, while, for the same OSNR degradation and interferer, the EVM estimates a crosstalk level of -14 dB. The estimations difference between the EVM and DEC methods was investigated by comparing the received constellations with the ideal ones, considering the duty-cycles of 50% and 33%. We have concluded that the EVM looses its accuracy when the amplitudes of the symbols in the received constellation do not reach the ideal symbols amplitudes in the transmitted constellation. For higher crosstalk levels, the EVM estimations deviate significantly from the DEC predictions. The same comparison between both methods estimations was performed for the 16-QAM coherent receiver and similar conclusions were drawn. As in the DEC method, the EVM identifies the QPSK RZ33 selected signal as the most tolerant to the in-band crosstalk and, considers the same signal as the less detrimental interferer to the performance of the M-QAM coherent receiver.

5.2 Future Work

From the conclusions drawn above, some work topics for future investigation are proposed:

- Analysis of the impact of multiple interfering terms on the performance of the M-QAM coherent receiver.
- Investigation of the in-band crosstalk impact on the performance of the coherent receiver with non-ideal PDM.
- Study of the impact of in-band crosstalk on the performance of optical ROADM-based networks.

Bibliography

[1] T. Xia and G. Wellbrock, "Commercial 100-Gbit/s coherent transmission systems", in *Optical Fiber Telecommunications*, 6th ed., Boston: Academic Press, 2013, ch. 2, pp. 45 – 82.

[2] P. Winzer, "Beyond 100G Ethernet", *IEEE Commun. Mag.*, vol. 48, no. 7, pp. 26–30, Jul. 2010.

[3] J. Pires, "Sistemas e redes de telecomunicações", Instituto Superior Técnico, 2006.

[4] X. Liu and M. Nazarathy, "Coherent, Self-Coherent, and Differential Detection Systems", in *Impact of Nonlinearities on Fiber Optic Communications*, New York, NY: Springer, 2011, vol. 7, ch. 1, pp. 1–42.

[5] P. Winzer, "High-spectral-efficiency optical modulation formats", *J. Lightw. Technol.*, vol. 30, no. 24, pp. 3824–3835, Dec. 15 2012.

[6] M. Seimetz, *High-Order Modulations for Optical Fiber Transmission*, Atlanta, GA: Springer, 2009.

[7] G. Agrawal, *Fiber-Optic Communication Systems*, 4th ed, John Wiley & Sons, 2010.

[8] A. Chen and E. Murphy, *Broadband Optical Modulators: Science, Technology, and Applications*. Taylor & Francis, 2011.

[9] J. Mori, C. Zhang, M. Usui, K. Igarashi, K. Katoh, and K. Kikuchi, "200-km transmission of 100-Gb/s 32-QAM dual-polarization signals using a digital coherent receiver", in *Proceedings of the European Conference on Optical Communications (ECOC)*, Sep. 2009, paper 8.4.6.

[10] J. Yu, X. Zhou, S. Gupta, Y.-K. Huang, and M.-F. Huang, "A novel scheme to generate 112.8-Gb/s PM-RZ-64QAM optical signal", *IEEE Photon. Technol. Lett.*, vol. 22, no. 2, pp. 115–117, Jan. 2010.

[11] E. Lach and W. Idler, "Modulation formats for 100G and beyond", *Optical Fiber Technology*, vol. 17, no. 5, pp. 377 – 386, Aug. 2011.

[12] I. Monroy and E. Tangdiongga, *Crosstalk in WDM Communication Networks*, Norwell, MA: Springer, 2002.

[13] P. Legg, M. Tur, and I. Andonovic, "Solution paths to limit interferometric noise induced performance degradation in ASK/direct detection lightwave networks", *J. Lightw. Technol.*, vol. 14, no. 9, pp. 1943–1954, Sep. 1996.

[14] J. C. Attard, J. E. Mitchell, and C. J. Rasmussen, "Performance analysis of interferometric noise due to unequally powered interferers in optical networks", *J. Lightw. Technol.*, vol. 23, no. 15, pp. 1692–1703, Apr. 2005.

[15] T. Chai, T. H. Cheng, Y. Ye, and Q. Liu, "In-band crosstalk analysis of optical cross-connect architectures", *J. Lightw. Technol.*, vol. 23, no. 2, pp. 688–701, Feb. 2005.

[16] J. Pires and L. Cancela, "Estimating the performance of direct-detection DPSK in optical networking environments using eigenfunction expansion techniques," *J. Lightw. Technol.*, vol. 28, no. 13, pp. 1994–2003, Jul. 1 2010.

[17] L. Cancela, J. Rebola, and J. Pires, "In-band crosstalk tolerance of direct detection DQPSK optical systems," in *IEEE Photonics Conference, paper ThS5*, San Francisco, 2012.

[18] M. Filer and S. Tibuleac, "Impact of ROADM in-band crosstalk on 40G DPSK signals", in *National Fiber Optic Engineers Conference (OFC/NFOEC)*, Mar. 2010, paper NthF5.

[19] L. Cancela, J. Rebola, and J. Pires, "Analytical assessment of the impact of OOK crosstalk signals on a DPSK direct detection system", in *Conf. on Telecommunications - ConfTele*, May 2013.

[20] P. Winzer, A. Gnauck, A. Konczykowska, F. Jorge, and J.-Y. Dupuy, "Penalties from in-band crosstalk for advanced optical modulation formats", in *37th European Conference and Exhibition on Optical Communication (ECOC)*, Sep. 2011, paper Tu.5.B.7.

[21] J. Oliveira, R. Silva, E. Silva, L. Carvalho, M. Silva, J. Neto, and A. Paradisi, "Crosstalk penalties analysis in mixed line transmission rates (10G-OOK/40G-DQPSK/112G-DP-QPSK/224G-DP-16-QAM) optical flexible grid networks", *Microw. Opt. Tech. Let.*, vol. 55, no. 1, pp. 119–122, Jan. 2013.

[22] E. Ip, A. Lau, D. Barros, and J. Kahn, "Coherent detection in optical fiber systems", *Opt. Express*, vol. 16, no. 2, pp. 753–791, Jan. 2008.

[23] L. Binh, *Digital Processing: Optical Transmission and Coherent Receiving Techniques*, CRC Press, 2014.

[24] M. Jeruchim, P. Balaban, and K. Shanmugan, *Simulation of communication systems: modeling, methodology and techniques*, 2nd ed., Norwell, MA: Kluwer Academic Publishers, 2000.

[25] R. Hui and M. O'Sullivan, *Fiber Optic Measurement Techniques*, Elsevier Academic Press, 2008.

[26] A. Carlson and P. Crilly, *Communication Systems*, 5th ed., McGraw-Hill Education, 2010.

[27] G. Agrawal, *Lightwave Technology: Telecommunication systems*, John Wiley & Sons, 2005.

[28] G. Agrawal, *Lightwave Technology: Components and Devices*, John Wiley & Sons, 2004.

[29] R. Ramaswami, K. Sivarajan, and G. Sasaki, *Optical Networks: A Practical Perspective, 3rd Edition*. San Francisco, CA: Morgan Kaufmann, 2009.

[30] R. Essiambre, G. Kramer, P. Winzer, G. Foschini, and B. Goebel, "Capacity limits of optical fiber networks", *J. Lightw. Technol.*, vol. 28, no. 4, pp. 662–701, Feb. 15 2010.

[31] M. Taylor, "Phase estimation methods for optical coherent detection using digital signal processing," *J. Lightw. Technol.*, vol. 27, no. 7, pp. 901–914, Apr. 1 2009.

[32] I. Ogama, T. Ohyama, H. Tanobe, R. Kasahara, S. Tsunashima, and H. Kawakami, "100-Gbit/s Optical Receiver Front-end Module Technology", *NTT Technical Review*, vol. 9, no. 3, Mar. 2011.

[33] J. Proakis and M. Salehi, *Digital Communications*, 5th ed., McGraw-Hill, 2008.

[34] A. Carena, V. Curri, P. Poggiolini, G. Bosco, and F. Forghieri, "Maximum reach versus transmission capacity for Terabit superchannels based on 27.75-GBaud PM-QPSK, PM-8QAM, or PM-16QAM", *IEEE Photon. Technol. Lett.*, vol. 22, no. 11, pp. 829–831, Jun. 2010.

[35] S. Yao, S. Fu, H. Wang, M. Tang, P. Shum, and D. Liu, "Performance Comparison for NRZ, RZ, and CSRZ Modulation Formats in RS-DBS Nyquist WDM Systems," *J. Opt. Commun. Netw.*, vol. 6, no. 4, pp. 355–361, Apr. 2014.

[36] T. Alves and A. Cartaxo, "Analysis of methods of performance evaluation of direct-detection OFDM communication systems", *Fiber and Integrated Optics*, vol. 29, no. 3, pp. 170–186, Mar. 2010.

[37] R. Shafik, S. Rahman, and R. Islam, "On the extended relationships among EVM, BER and SNR as performance metrics," in *International Conference on Electrical and Computer Engineering (ICECE)*, pp. 408–411, Dec. 2006.

[38] M. McKinley, K. Remley, M. Myslinski, J. Kenney, D. Schreurs, and B. Nauwelaers, "EVM calculation for broadband modulated signals", in *64th ARFTG Conf. Dig*, pp. 45–52, Dec. 2004.

[39] T. Alves and A. Cartaxo, "Performance evaluation methods of direct-detection OFDM systems", in *International Conf. on Transparent Networks (ICTON)*, Jun. 2009, paper Tu.C5.2.

[40] S. Bottacchi, *Noise and Signal Interference in Optical Fiber Transmission Systems: An Optimum Design Approach*, John Wiley & Sons, 2008.

[41] R. Sadr and W. J. Hurd, "Detection of signals by the digital integrate-and-dump filter with offset sampling", *Telecommunications and Data Acquisition Progress Report*, vol. 91, pp. 158–173, Sep. 1987.

[42] L. Paarmann, *Design and Analysis of Analog Filters: A Signal Processing Perspective*, Klumer Academic Publishers, 2003.

[43] G. Bosco, V. Curri, A. Carena, P. Poggiolini, and F. Forghieri, "On the performance of Nyquist-WDM terabit superchannels based on PM-BPSK, PM-QPSK, PM-8QAM or PM-16QAM subcarriers", *J. Lightw. Technol.*, vol. 29, no. 1, pp. 53–61, Jan. 1 2011.

[44] L. Cancela and J. Pires, "Quantifying the influence of crosstalk-crosstalk beat noise in optical DPSK systems", in *International Conference on Computer as a Tool (EUROCON)*, Apr. 2011.

[45] P. Winzer, M. Pfennigbauer, and R. Essiambre, "Coherent crosstalk in ultra-dense WDM systems", in *Proceedings of the 30th European Conference on Optical Communication (ECOC)*, Stockholm, Sweden, pp. 1734–1744, Sep. 2004.

[46] K.-P. Ho, "Effects of homodyne crosstalk on dual-polarization QPSK signals", *J. Lightw. Technol.*, vol. 29, no. 1, pp. 124–131, Jan. 1 2011.

[47] J. Rebola, L. Cancela, and J. Pires, "Impact of multi-rate and multi-format crosstalk signals on the performance of 40 Gbit/s DQPSK optical receivers", in *INSTICC International Conf. on Photonics, Optics and Laser Technology - PHOTOPTICS*, pp. 56–62, Jan. 2014.